Systematic Exploration of Cellular Lattice Structures for Aerospace Applications

A Major Qualifying Project Report

Submitted to the Faculty of the

WORCESTER POLYTECHNIC INSTITUTE

in Partial Fulfillment of the Requirements for the

Degree of Bachelor of Science

in Aerospace Engineering

by

____

Neal Keklik

____

Mike Lam

____

Cassandra Lira

____

Ivan Nikulin

____

Nicholas Pitti

____

Julia Rivelli

____

Matthew Withington

April 2, 2021

Approved by: ________________________

Professor Karanjgaokar

Abstract

The objective of this project is to explore the utility of a novel class of lattice-structure-based materials for effective cooling in a jet engine turbine blade, thus improving the overall efficiency of the aircraft. As opposed to existing technology based on metallic foam in such applications, optimized lattice structures enabled through recent advances in additive manufacturing can provide similar cooling performance with significant improvements in structural, acoustic, and thermal performance. This multidisciplinary exploration involved the design (SolidWorks and Netfabb) based on various performance requirements for the jet turbine blades and the subsequent realization of various lattice structures using additive manufacturing. Finite element method (FEM) based thermal and structural simulations were then performed on a few lattice structures selected through preliminary analytical predictions. The FEM results for simplified boundary conditions were then validated through a series of thermal, static loading, and vibrational experiments. Structural simulations for the lattice structures for both the loading conditions experienced in jet turbine blades as well as simplified static and low amplitude vibrational loading were conducted using ABAQUS and the results are validated using static experiments (Instron tensile tester). The corresponding thermal and flow simulations were performed in COMSOL and validated through custom-built experiments to measure thermal expansion, heat transfer, and flow velocity for low-speed, laminar flows at slightly elevated temperatures.

Acknowledgments

We would like to thank our project advisor, Professor Nikhil Karanjgaokar, for his guidance and support throughout the entirety of the project. We would also like to thank Doctor Adriana Hera and Professor Zhangxian Yuan for their help and support on finite element analysis. Additionally, we would also like to thank Ian Maskery for freely sharing his Functional Lattice Package (FLatt Pack) software.

Table of Authorship

Section:	**Author:**
Abstract	All
1.Introduction	Julia
1.1 Background and Lit Review	Julia, Neal
1.1.1 Design Section	Julia
1.1.2 Structure Section	Nicholas, Ivan
1.1.3 Thermal Section	Cassie, Mike
1.1.4 Force Analysis	Neal
1.2 Overall Project Goals	Neal
1.3 Project Design Requirements, Constraints and Other Consideration	All
1.4 Overall Project Management	Julia
1.5 Project Objective Methods and Standards	All
1.6 Project Tasks and Timetable	Neal
2. Design	Julia, Neal
2.1 Methodology	Julia
2.2 Software	Julia
2.2.1 Solidworks	Julia
2.2.2 FLatt pack	Julia
2.2.3 Netfabb	Neal
2.3 Design One	Julia
2.4 Design Two	Neal
2.5 Design Three	Neal

2.6 Discussion	Julia, Neal
3. Structural Analysis	Ivan, Matthew, Nicholas
3.1 Methodology	Nicholas
3.2 Instron Testing	Nicholas
3.3 Design One- Orthogrid and Honeycomb	Ivan
3.4 Design Two - Gyroid, Simplified Arch	Ivan
3.5 Design Three - Traditional Arch	Ivan
3.6 ABAQUS Simulations and Modeling	Matthew
3.7 Results	Ivan, Nicholas, Matthew
4. Thermal Analysis	Cassie, Mike
4.1 Property Selection	Cassie, Mike
4.2 Experiments	Cassie
4.3 COMSOL Simulation	Mike
4.4 Experimental Results	
4.4.1 Thermal Expansion Results	Cassie
4.4.2 Heat Transfer Results	Cassie
4.4.3 Velocity Change Results	Mike
4.5 Simulation Results	
4.5.1 Thermal Expansion Simulation Results	Mike
4.5.2 Flow Simulation Results	Mike
4.5.3 Heat Transfer Simulation Results	Mike
4.6 Discussion	Cassie, Mike
5. Summary, Conclusions, Recommendations, Broader Impacts	
5.1 Summary	Julia
5.2 Conclusions	All

5.3 Recommendations	All
5.4 Broader Impacts	Julia
7. References	All

Table of Contents

List of Figures

List of Tables

1. Introduction

This Major Qualifying Project (MQP) consisted of a 7-student group dedicated to the design and testing of different lattice structures. This project was the first of its kind to take place at WPI, and ultimately explored different types of lattice structures that would be the most effective in the cooling of a jet engine turbine blade. The team consisted of 3 sub-teams: design, structures, and thermal, all of which were led by an advisor, Professor Karanjgaokar. The Design team consists of two members, Neal Keklik and Julia Rivelli, the Structural Analysis team consisting of three members, Ivan Nikulin, Nick Pitti, and Matthew Withington, and the Thermal Analysis team consisting of two members, Mike Lam and Cassandra Lira.

The project centered on the research and design of a variety of lattice structures and their fabrication in software such as AutoCAD, Solidworks, FLatt pack, and Netfabb. Once testing amongst other sub-teams began their goal was to provide other teams with any CAD designs they needed based on their findings. The primary objective of the structures team is to 3D print structures made by the design team and perform a variety of tests for both loading conditions experienced in jet turbine blades. Additionally, conducting ABAQUS simulations for simplified and low amplitude vibrational loading on a variety of lattice structures. Results are validated using a variety of experiments and tools including an Instron stress tester.

The goal of the thermal team is to perform corresponding flow and turbulent simulations using COMSOL. A variety of custom-built experiments were created to measure thermal expansion, heat transfer, and flow velocity for low-speed, laminar flows at slightly elevated temperatures.

1.1 Background and Literature Review

A lattice structure is a space-filling unit cell that can be tessellated along any axis with no gaps between cells. These structures can be made up of patterns such as octagonal, honeycomb or even random patterns joined together by webs or trusses. More importantly, the patterns that the lattice structure takes on can lead to interesting properties such as negation poison ratios or natural dampening attributes. Therefore, it is vital to understand how different patterns can lead to specific characteristics when designing and integrating lattice structures into industrial products.

This literature will specifically go over how lattice structures are used in the aerospace industry and how they can be improved for a turbine blade. However, lattice structures and the designs that will be discussed in this paper do not necessarily have to be applied to only turbine blades. They can be altered and applied in other situations unique to the aerospace industry.

Traditionally, lattice structures have been used in rotors, rockets, propellers, satellite platforms, launcher payloads, and even antenna towers. Lattice structures are extremely useful in aerospace applications because they can absorb a large range of vibrational activity during a rocket's mission which could prove to be devastating to the structure of the rocket if they are not absorbed. In other industries, soft materials have been used to absorb vibrations in structures. According to Nicolette Emmino, author of New Lattice Structure Absorbs Dreadful Vibrations from Propellers, Rotors, and Rockets, soft materials do prove to be effective; they are limited in terms of range or bandwidth. Lattice structures on the other hand can provide damping abilities with greater bandwidth. This is an example that portrays the importance of lattice structure integration into the aerospace industry [39].

Currently, most basic level lattice structures can exist as an Isogrid or Orthogrid design. Isogrid lattice structures have an oscillating triangular pattern while Orthogrid lattice structures have rectangular patterns. Even a simple difference between a square and triangular pattern can have drastic effects on the characteristics of the lattice structure.

The pattern that comprises the lattice structure is not the only characteristic that can contribute to the properties of the structure. The materials that the lattice structure is made from can have a very drastic effect. In the case of this paper, auxetic and non-auxetic materials will be examined [38]. According to Prawoto [39], experimental and numerical reports for most auxetic materials indicate negative Poisson’s ratio values. In other words, the structure under tension or compression will expand or contract in the axis perpendicular to the outside force. Figure 1 below illustrates this well.

1.1.1 Design Section

When looking into lattice structure design, a valuable source of the material is that of auxetic materials. Auxetic cellular materials are modern materials that have some unique and superior mechanical properties. Their origin of investigation dates back to the 1980s. As previously stated these materials are also known to possess a negative Poisson's ratio, becoming wider when stretched and thinner when compressed.

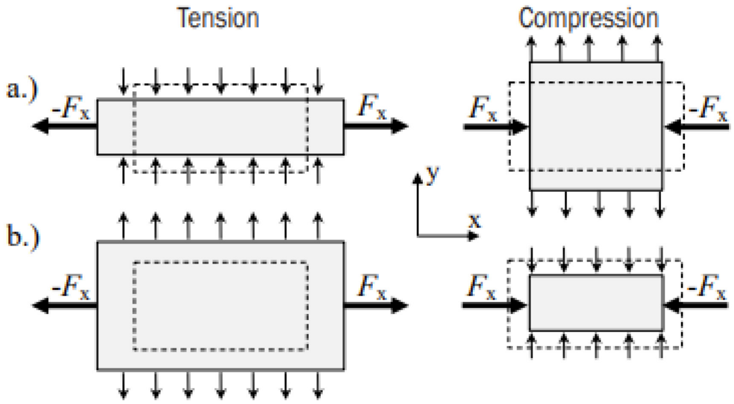

Figure 1: Comparison of Expected Deformation Under Uniaxial Tensile and Compressive Loading for a) Materials with Positive Poisson's Ratio, and b) Materials with Negative Poisson's Ratio [32]

There are three main groups of classification: Auxetic honeycombs, auxetic polymers, and auxetic composites. Honeycomb geometries can vary, some having missing ribs, Chiral vs. Anti-Chiral, etc. There also exists auxetic microporous and molecular polymers that possess auxetic properties. This occurs because their porous structures allow sufficient space for the nodules to spread apart. Research has observed auxetic behavior of some of the polymer structures is not dependent on the scale of the material convenient for the production of larger specimens and components. Auxetic composites are made of two or more components with different material properties. Materials have improved the shear performance (increased shear modulus), damping, sound (also with control of bands), and energy absorption of structural components. Because of such properties, auxetic materials are being increasingly used in body and vehicle armor applications. They are predominantly used in sandwich plates for ballistic protection in combination with other materials and fiber composites for greater pull-out resistance (applied tension pull-out force causes an increase of cross-section area) [32].

Amongst other materials, the team also explored Inconel and plastics. Modern aircraft and engines are seeing far more reliability now than predecessors did. Additive layer manufacturing is allowing for even greater leaps in the aerospace industry, both reducing cost and having incredible performance benefits. One of these materials being Inconel 718. The aerospace industry is increasingly relying on high-temperature alloys that can withstand severe mechanical stresses and strains in extremely hot environments while remaining stable, corrosion-resistant, and creep-resistant. Nickel-iron-based superalloys are best suited for these applications. Recently Inconel 718 is being used extensively, it accounts for about 50% of the weight of aircraft turbojet engines being the main component for discs, blades, and casing of the high-pressure section of the compressor and discs as well as some blades of the turbine section [20].

Once past material investigations the team began looking into geometries of lattice structures, specifically chirality. Chirality is among the most readily observed topological features in natural structures. The difference between Chiral and Anti-Chiral structures lies in their ability to be superimposed. Anti-Chiral structures are superimposable with their mirror image whereas Chiral structures are not. Bot structures have an abundance in nature and can be contrasted with man-made constructions, which often rely on multiple materials selection. There exists a class of metamaterials like periodic Chiral structures such as the ones shown in Figure 2.

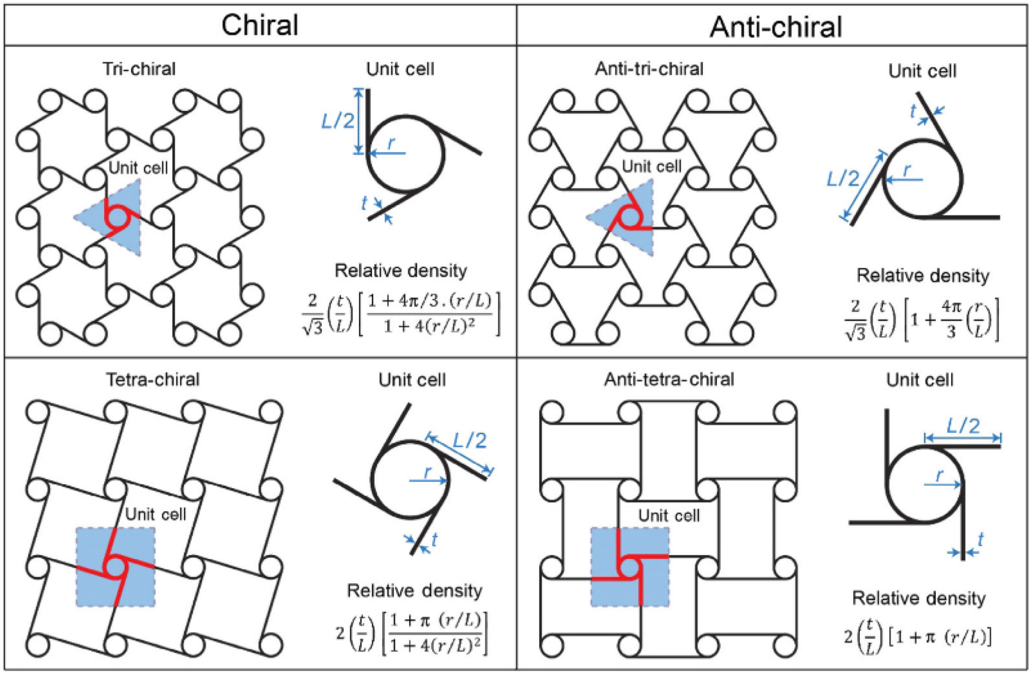

Figure 2: Schematic Representations of Examples for 2D Chiral and Anti-Chiral Lattice Structures [23]

These have been shown to possess relatively compliant behavior because of their bending-dominated response while exhibiting considerable multiaxial expansion/contraction under uniaxial loads due to the auxetic structure. Such features make them optimal for flexible design applications. Additionally, structures like Chiral Honeycombs have been experimentally and theoretically shown to possess Poisson's ratios in the range of $-1 < \nu < 0$ [23].

In addition to lattice structures being composed of different materials/properties, there are many different kinds of geometries. Grid composite structures are a promising solution to replacing some of the current aluminum and sandwich monolithic composite parts. The simplest being Orthogrid, Square Pattern, and Isogrids, Triangular Pattern shown below in Figure 3, and as previously discussed. These lattice structures are usually sandwiched between two flat composite panels, Orthogrid having stronger mechanical properties like more advantageous energy absorption and strength [7].

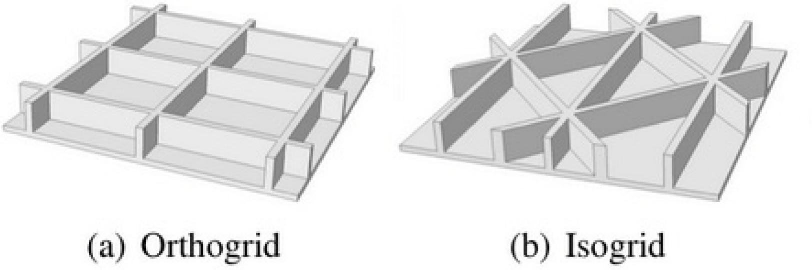
(a) Orthogrid (b) Isogrid

Figure 3: a) Orthogrid Structures Resemble a Grid Pattern while b) Isogrid Structures Resemble Triangular Patterns [2]

Another common geometry is a honeycomb. Honeycomb structures are a lattice composed of hollow, thin-walled cells with relatively high compression and shear properties out-of-plane while boasting a low density. The shape of these structures can vary but their cells are often characterized by a hexagonal and columnar shape. Honeycomb structures allow for the minimization of materials to save both weight and cost during design and manufacturing processes. In addition to this, they have high specific strengths, which makes them an advantageous option in the aerospace industry [6].

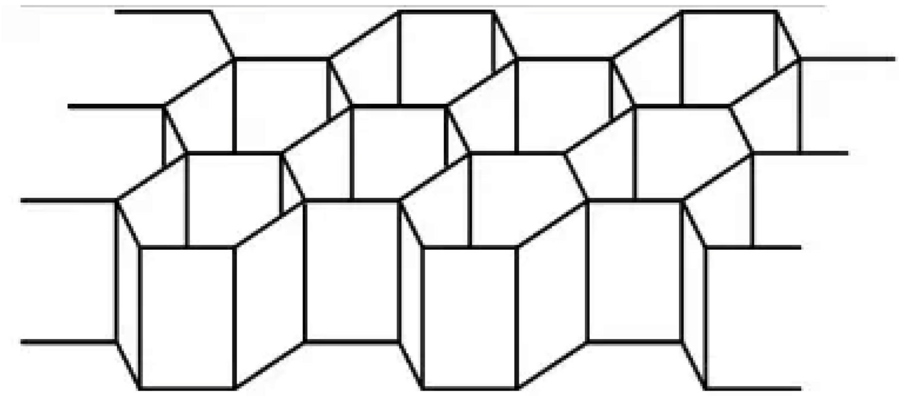

Figure 4: Honeycomb Structure Showing Two-Dimensional, Prismatic Nature [10]

Mechanical properties of different Honeycomb structures depend on their cell geometry, the properties of the material from which the Honeycomb is constructed, which can include things like Young's modulus, yield stress, and fracture stress of the material. The elastic moduli of low-density Honeycomb structures are independent of the axis. Other mechanical properties of Honeycomb structures will vary based on the direction in which load is applied. Therefore, the two planes of symmetry must be identified and distinguishable. They are also often used in mesh form for aerodynamics applications. A Honeycomb mesh can be used to reduce or create wind turbulence, but can also be used to obtain a standard profile in a wind tunnel, (temperature and flow speed) [42].

Another lattice geometry would be that of an Arch lattice. Like other lattice structures, these possess qualities like low density, high specific strength, high specific stiffness, good energy absorption ability, excellent thermal and acoustic insulation properties. In this work, the team specifically looked at two variations of Arch lattices, one with an arch curvature and one lacking such ("Simplified Arch") as seen in Figure 5, structures a-d representing that of an Arch structure and e-h representing the modified.

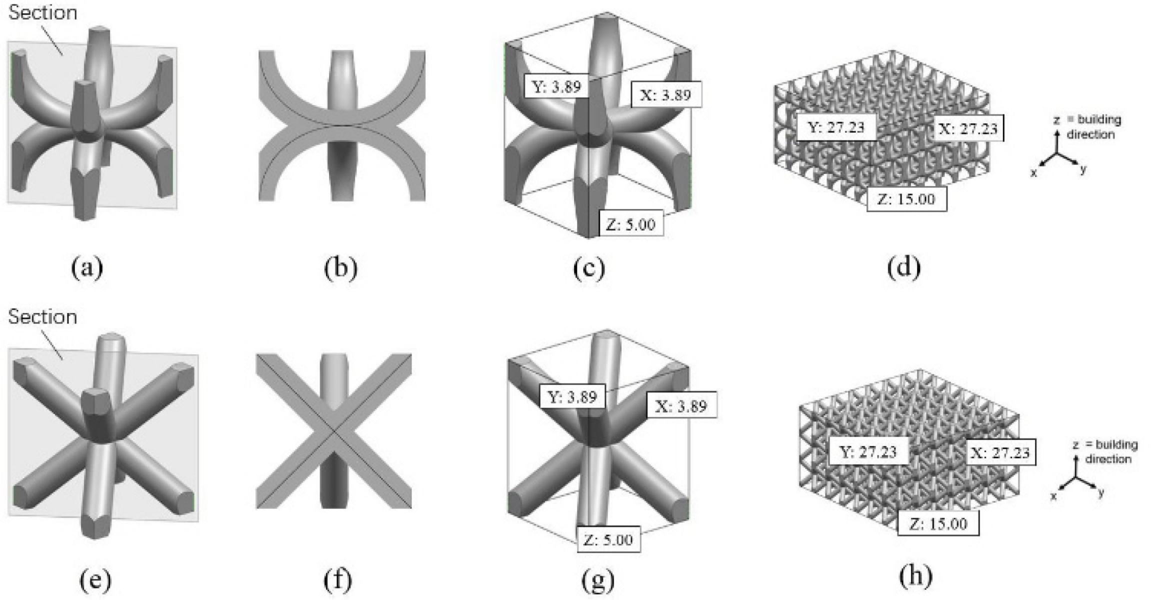

(a) (b) (c) (d)

(e) (f) (g) (h)

Figure 5: Traditional Arch Lattice Structure Design is Characterized by Curved Struts (a - d) While Straight Strut Lattice Design is Characterized by Straight Struts (e - h) [15]

Some research performed on these two variations to show the difference that comes with a straight strut vs. an arched. A series of testing was done that compared compression of structures and energy absorption. The conclusions drawn were that under the same relative density the compressive strength of the Arch lattice structure was over 100% higher than that of the Simplified Arch. The elastic modulus of the Traditional Arch structure was also much higher than that of the Simplified Arch, the Arch lattice structures possessing better overall mechanical properties. The Traditional Arch was also shown to possess better energy absorption properties than that of the Simplified Arch lattice [15].

The team also investigated some other lattice replacements such as foams and Gyroids. There are a variety of foam cells, polymeric, metallic, ceramic, and open or closed, all used for a variety of different things. Synthetic polymer foams are widely used in cushioning, packaging, and energy-absorption applications [12]. Metallic foams like cellular structures can be manufactured at relatively low costs which makes them an attractive class of engineering material. These foams are usually used in sandwich structures, compressed with walls, which allows them to be strong and stiff. Stiffness and strength are strongly influenced by cell wall bending for all loading conditions. Most closed-cell foams follow scaling laws similar to open-celled foams. They buckle or rupture at such low stresses the bending/buckling contribution to stiffness and strength values is minimal, leaving the cell edges to carry most of the load. Figure 6 shows the comparison of (a) closed-cell foams vs. (b) open-cell foams in a cubic form [21].

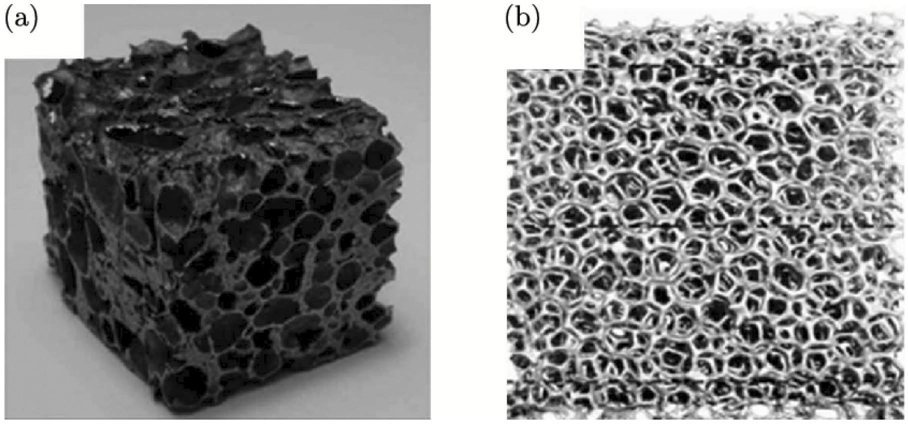

Figure 6: Foam Comparison: a) Closed Cell Foam vs. b) Open Cell Foam [31]

In addition to foams, the team explored the utility of Gyroid structures. Unlike typical foams, Gyroid is not necessarily a regular lattice structure cell and belongs to the triply periodic minimal surfaces family, which is a group of surfaces that possess crystallographic symmetries, as seen in Figure 7. The structure on the left showing three-dimensionally repeated unit cells, and that on the right showing a singular unit cell. Like other examples talked about above, their main source of further research and investigation lies in the pursuit of using lighter cost-effective materials.

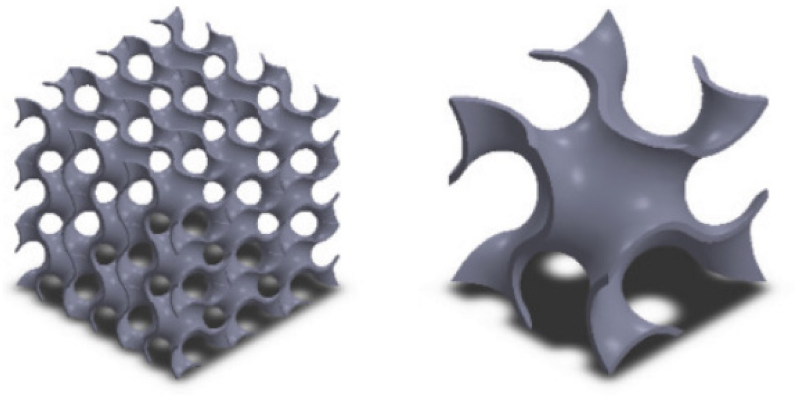

Figure 7: A Single Gyroid Unit Cell (right) and a Gyroid Structure Comprised of Multiple Gyroid Unit Cells (left) [1]

Similar research was done on the mechanical properties of Gyroid structures under compressive loading and energy absorption as discussed earlier. Furthermore, to perform finite element analysis the base material was tested under tensile and compressive loading conditions where strain rates were applied and then attained results. Results obtained from experimentation and computations were in very good agreement, showing that Gyroid structures possess comparable mechanical properties to other structures and are a strong potential candidate for various advanced technological applications [1].

1.1.2 Structure Section

Rigid body structural analysis is the simplest and most primitive mode of structural analysis of a solid object. To understand the more complex and advanced methods of analysis, the team explored the most basic and simple method first. The simple rigid body structural analysis method involves treating the body as a uniform or isotropic solid. The definitions of “uniform” and “isotropic” include constant key properties such as material density, chemical composition, thermal and structural properties throughout the solid. To maintain simplicity, common constraints and basic loads were explored. Basic formulas, values, and constants were used in traditional problems with beam bending, stretching, and coupling to demonstrate similar effects expected on parts designed by the project team.

To accurately simulate the behavior of the designed samples, research on conditions inside the turbine section of jet engines was done. Any turbine blade mainly experiences four types of loads and stresses: centrifugal or rotational body force, thermal stress, bending gas loads, and vibratory stress. The most dominant and influential load is the centrifugal body force load caused by and directly proportional to the rotation of the jet engine shaft. Circular motion on a constant and stationary axis produces a load distribution acting on every part of the body, in this case, the turbine disk and blades. Hence the “body” in the name of the load, as it acts through the entire body, with a force distribution such that matter at the axis of rotation experiences the largest load and matter at the tip of the turbine blades experiences the smallest load. The rotational body force load is greatest at the peak angular velocity of the engine shaft and turbine disk. The high angular velocity exerts a pulling load on the turbine blades due to centripetal acceleration. To calculate the load, basic values such as geometric parameters, modulus of elasticity, and Poisson's ratio were used. For the specific case of rotational body force loading, values for parameters such as density of the material and angular velocity are required. The resulting force can be used in a basic formula for stretching, involving the initial length and elasticity modulus.

The second load that turbine blades experience is the load that is due to the rotary acceleration of the turbine disk. Similarly, the second load calculation involves the use of unique values of material density and angular acceleration. The rotary acceleration load causes the turbine blades to bend in the plane of the turbine disk rotation. The third load considered in the analysis was the load caused by the airflow through the jet engine. Aerodynamic drag applies a load perpendicular to that of the plane of turbine disk rotation.

Although preliminary calculations of the loads and stresses experienced by a turbine blade are reliable and proven, numerical simulations provide tremendous insight into the deformation and stress fields developed in real turbine blades during the typical operating conditions. Therefore, the development of reliable finite element analysis (FEA) models for all the structures/tests was a critical task. This task involving numerical simulations was executed using the commercial finite element analysis software ABAQUS (version 2019).

The literature on how to develop these simulations was sparse, and hence the initial simulations presented in this work relied on a trial and error approach. None of the structures team members had used ABAQUS or any FEA software before, which compounded the difficulty of creating the geometries used in the simulations and the stresses/loads input on these geometries. Nevertheless, once the skills were acquired to be able to develop functioning models in ABAQUS, it expanded the ceiling for simulating more complex scenarios that would emulate the working conditions of a functioning turbine blade.

To validate the mathematical calculations and finite element analysis simulations the project team designed and conducted experiments in the laboratory. With the absence of actual superalloy materials to perform various tests with, the team decided to use polymer specimens. The project team expected that the tested polymer structures would exhibit a behavior similar to that of a superalloy structure. The results of such tests were expected to be proportional based on the basic material characteristics. Contingent on the ratios of elasticity moduli and Poisson's ratios of the polymer and super-alloy, adjustments to the resulting experimental values could be made. The validity of the assumptions stands if the forces involved in the experimental procedures are adjusted accordingly.

To create a complex lattice structure, the additive manufacturing method is typically used, as opposed to subtractive manufacturing. Additive manufacturing builds the part by adding the material to it, whereas subtractive manufacturing takes a material and cuts away portions to result in the desired part. When utilizing subtractive manufacturing to create a part, a lot of time and money go into machining the castings, as well as the long cooling period following its creation. Performing subtractive manufacturing typically yields approximately 10% of the original superalloy as a finished product [35]. When creating lattice structures, due to their complexity, additive manufacturing is the preferred method as it allows for design freedom.

The proposed method of turbine blade manufacturing utilizing selective laser melting (SLM), or electron beam melting (EBM) systems allows for the manufacturing of the complex internal lattice structures, otherwise not possible using the common molding or machining manufacturing methods. The additive turbine blade SLM manufacturing method was considered to be similar to the process used in the team laboratory for the production of experimental polymer samples. Regardless of what method is utilized in the field, the material requires heat treatment following its fabrication to optimize its strength properties.

The strength of the material lies within the formation of its microstructure during heat treatment. The microstructure with desirable properties is in essence obtained by disturbing the phase transformation, which is done by disturbing the heat treatment of the material following its casting. Microstructure control must be precise and accurate, as the gamma prime precipitates form during cooling.

Gamma prime is an intermetallic phase precipitate that is used to strengthen the nickel superalloy. They are part of a two-phase microstructure that forms as a result of the mixture of materials to create the superalloy [11]. The two phases are the gamma face-centered cubic matrix and the gamma prime precipitates that form within the matrix. The mismatch of the matrix/precipitate determines the shape of the gamma prime particles. These particles morph their shape to decrease their energy and approach a stable state, where the material is uniform and at its strongest. There are also elastic energies within the gamma prime precipitates, which are sometimes strong enough to control the shape as well (Minoru & Miki, 2004). Spheres are the preferred shape for the gamma prime precipitates, as there is less surface area on a sphere than a cube, thus resulting in less surface energy [11].

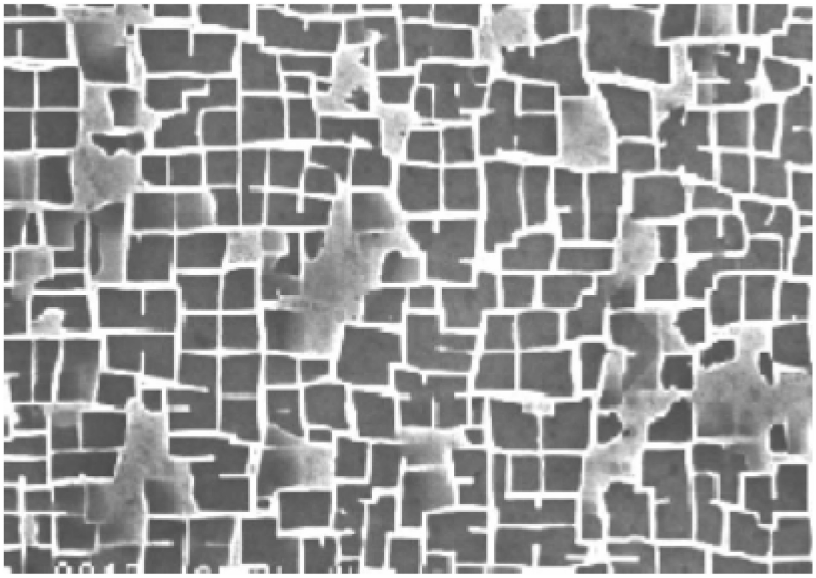

Figure 8: Gamma Matrix with Gamma Prime Precipitates [11]

As shown in Figure 8 above, the gamma prime precipitates have formed on this gamma matrix as cubes. This is not an exact science, and there is variation in the size and shape of the gamma prime precipitates. Unimodal distribution of fine particles throughout the matrix is preferred, although difficult and impractical to achieve in practice. Thus, multimodal distribution is typically adopted [24]. The multimodal distribution can range in size, with gamma prime particles being as small as 5nm up to 1µm. These sizes are determined from many factors such as material composition and heat treatment aging time. The material's strength is a direct correlation to the uniformity of the gamma and gamma prime matrix.

Comprehension of how the superalloy retains its strength under extremely high temperatures allows one to understand why these processes are important and gives insight as to how it could be done in a professional environment. Next, one can now look at the fabrication stage of the material through additive manufacturing. Two types of additive manufacturing 3D metal printing are the selective laser melting (SLM) method, and the electron beam melting (EBM) method. Both techniques are classified as powder bed fusion (PBM) processes. Powder bed fusion uses mechanisms to spread extremely thin layers of the powdered metal material over the work area, where a heat source is used to selectively melt sections based on the CAD file input. Another approach to consider when performing additive manufacturing is the direct metal deposition method, which deposits the material while it is melted using two nozzles concurrently. However, the PBM processes would have been used if the facilities were available and thus will be analyzed on how they execute their printing [13].

PBM methods come with some advantages that traditional casting approaches do not have, such as the rapid cooling rates. When the material is cured by the laser, there are cooling rates of up to 10^6 K/s, which results in improved mechanical behavior, grain refinement, and reduced chemical dendritic segregation [13]. PBM printers are also ideal for creating lattice structures, as it grants design flexibility, allowing for the construction of complex parts. However, it is important to keep in mind the drawbacks of PBM additive manufacturing and comprehend the deformities or defects the material could potentially have.

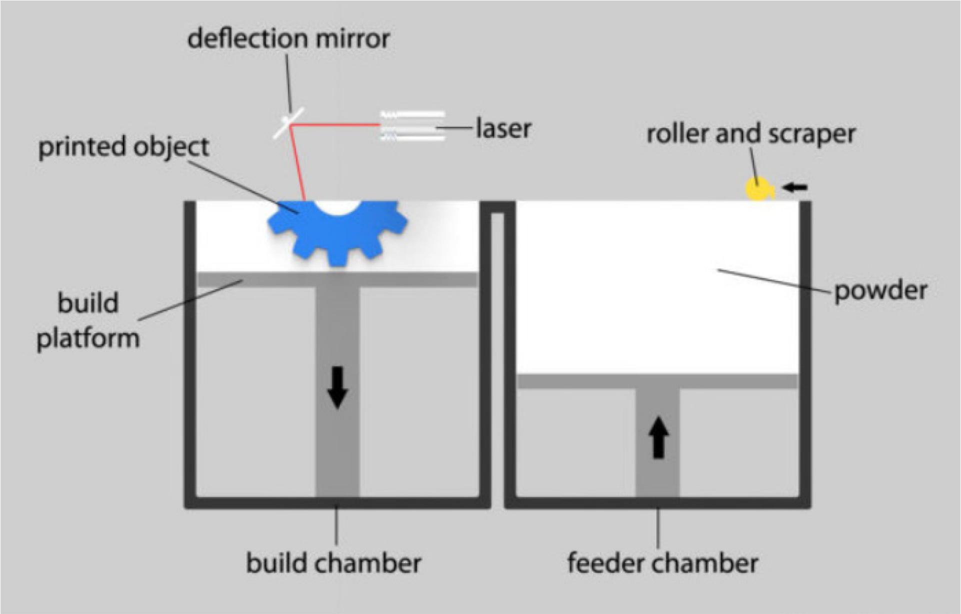

Figure 9: Powder Bed Fusion Additive Manufacturing Process [29]

With the benefits of rapid cooling also come consequences. Pores can form within the material, which are small empty spaces <100μm in diameter, resulting from gases in the melt pool being trapped during the rapid cooling. There are also natural errors, such as spatter and balling. Spatter occurs at high energy densities, where the force of the laser at the time of curing may cause molten material to be expelled out. The material then clumps with other material around it and causes inaccuracies in your structure. Balling occurs when the melt pool does not wet the layer beneath it, which would connect it to the structure [18]. Instead, the material "balls up" or forms into a sphere, not connecting itself with the rest of the structure. These consequences can result in irregularities within the lattice structure, and the problems can snowball into successive layer defects [18].

The advantages and disadvantages must be taken with each decision in the design process. The settings on the printer dictate how well the structure will print, thus it is important to find a balance between the settings. Researching PBM printers allowed the team to understand some of the nuances and finer details of 3D printing on a general level. The knowledge acquired researching additive manufacturing was applied to using and learning more about the 3D printer that would be used for the project.

Photopolymerization is a 3D printing process that is similar to PBM, where a laser selectively cures the material layer by layer. The difference between the two methods is the material used for photopolymerization is a liquid resin, that cures into plastic, as opposed to a metallic powder. Each layer is on average in the hundreds of microns of thickness for most vat polymerization printers, and for our specific printer, it is 200 microns [46]. This method of printing will also give similar design flexibility regarding complex structures to PBM printers, making it an ideal choice for printing lattice structures.

The resin resides inside a vat with a clear, acrylic bottom. The build plate lowers down into the vat, where the laser aiming upwards, selectively cures the resin based on the file provided. The part is printed upside down; the build plate raises as the part is cured from the bottom-up, which is shown in Figure 10.

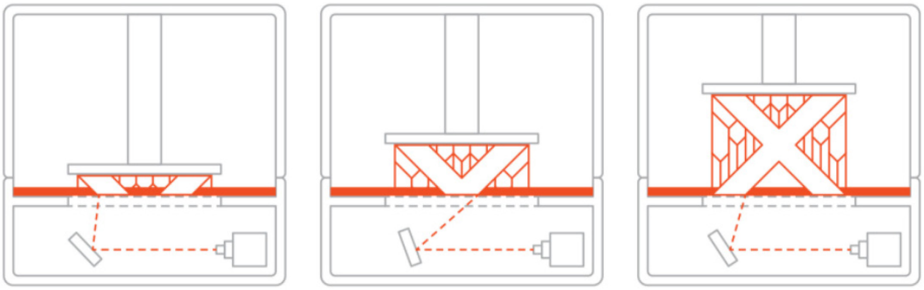

Figure 10: Photopolymerization SLA 3D Printing Process [46]

It is worth noting that vat polymerization printers are notoriously messy to work with. The resin is very sticky and is dangerous to touch before being cured. There are also many post-processing steps required before the part is ready for use. These were clear disadvantages of using a vat polymerization printer in practice, however, the advantages given by this method of 3D printing outweigh the disadvantages.

1.1.3 Thermal Section

A modern gas turbine engine has hot gas leaving the combustor and entering the turbine at temperatures ranging from 1750 to 2200 K. However, most alloys currently used in manufacturing the blades of jet turbines have a melting temperature of 1300-1500 K. The temperature at which the turbine blades can safely operate at (the blade service temperature) is 80% of the melting temperature, or approximately 1100-1200 K, as seen in Figure 11 [19]. Therefore, it is necessary to cool the first few stages of a turbine to prevent catastrophic failure during operation. Additionally, jet engine improvements in efficiency and power output are also limited by the turbine inlet temperature. A higher turbine inlet temperature is optimal because it improves both efficiency and power output [51] while simultaneously lowering emissions [8]. This means that reducing inlet temperatures is not an attractive solution.

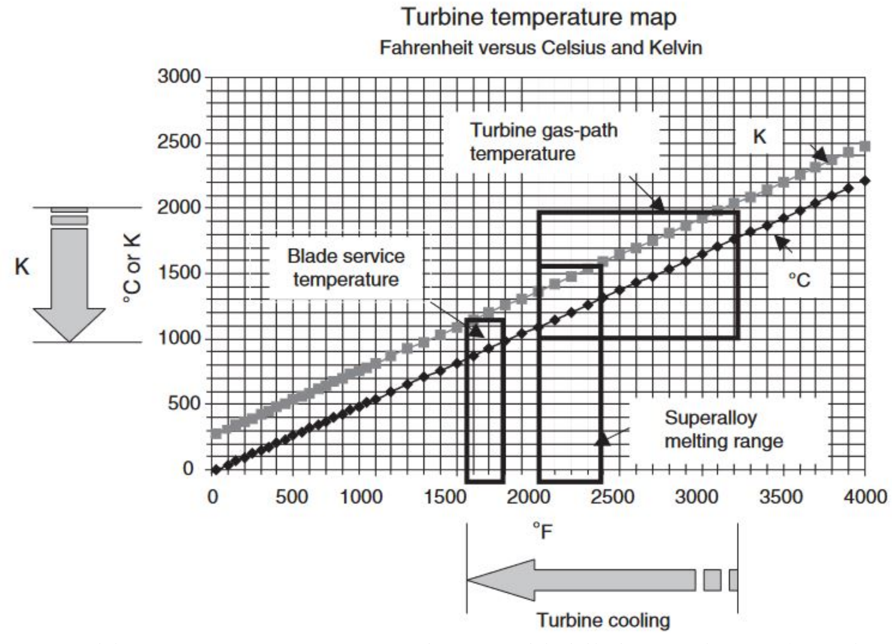

Figure 11: Turbine Temperature Map. The map highlights regions of an air temperature of serviceable blade temperature, gas temperature in the turbine, and the melting temperature of superalloys. [19]

Current turbine cooling methods that improve a turbine's ability to withstand extreme heat are either active or passive. Passive methods include coating the surface with a heat-resistant material or utilizing nickel-based superalloys [3]. Active methods, such as film cooling and convective cooling, utilize coolant systems. Convective cooling depends on two parameters: area and temperature difference. In a turbine blade that is convectively cooled, the internals of the turbine blade is split into smaller sections with channels containing coolant that draw heat away from the surface of the blade as seen in Figure 12 below.

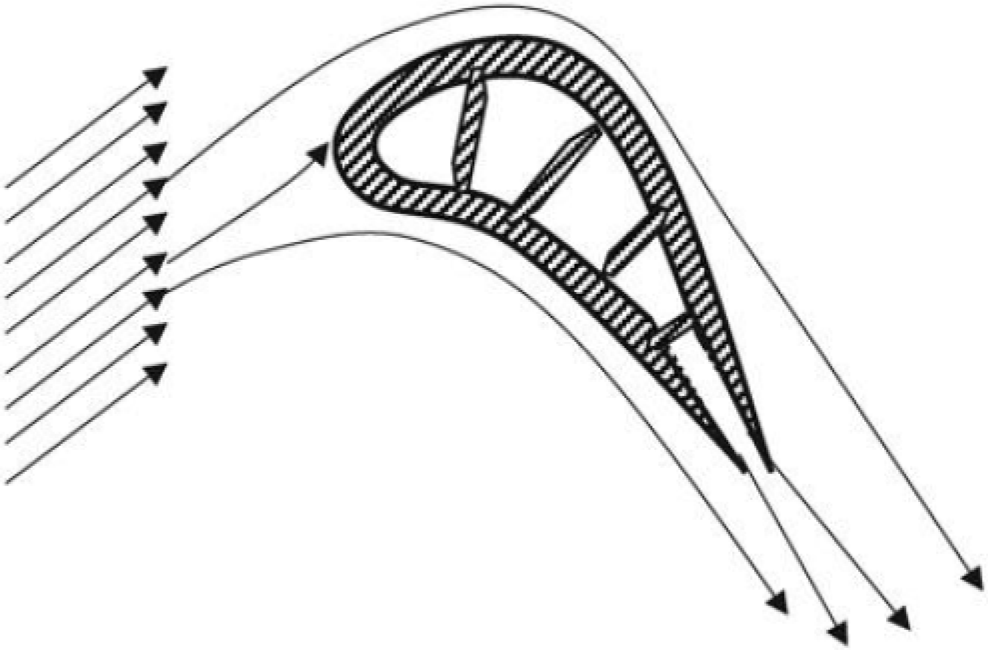

Figure 12: Schematic Representation of a Convectively Cooled Turbine Blade [19]

Film cooling is another method in which the surface of turbine blades is actively cooled using coolants. Unlike convective cooling, in film cooling, the coolant "shoots" out of small holes on the blade at an angle to the incoming flow, covering the surface of the blade with a film of coolant, as seen in Figure 13. However, there are a few disadvantages to using film cooling. Firstly, the interaction between the coolant and the hot gas flow as the coolant leaves the hole creates a local flow separation right after the hole, meaning the overall drag of the turbine blade is increased. Additionally, the coolant is only able to cover a small area after the hole effectively, meaning many holes are needed throughout the blade to effectively cool the entire surface of the blade, as seen in Figure 14.

Figure 13: Schematic Representation of a Film Cooled Turbine Blade [19]

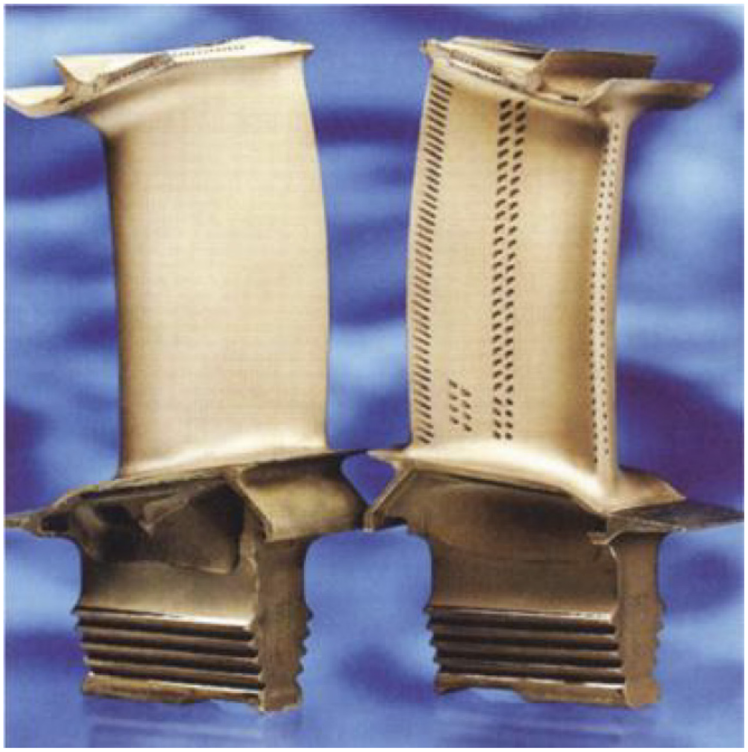

Figure 14: Film Cooled Turbine Blade [19]

The last active cooling method is transpiration cooling. Transpiration cooling works by having coolant interacting with the hot gases by emerging from a microporous foam, as seen in Figure 15 below.

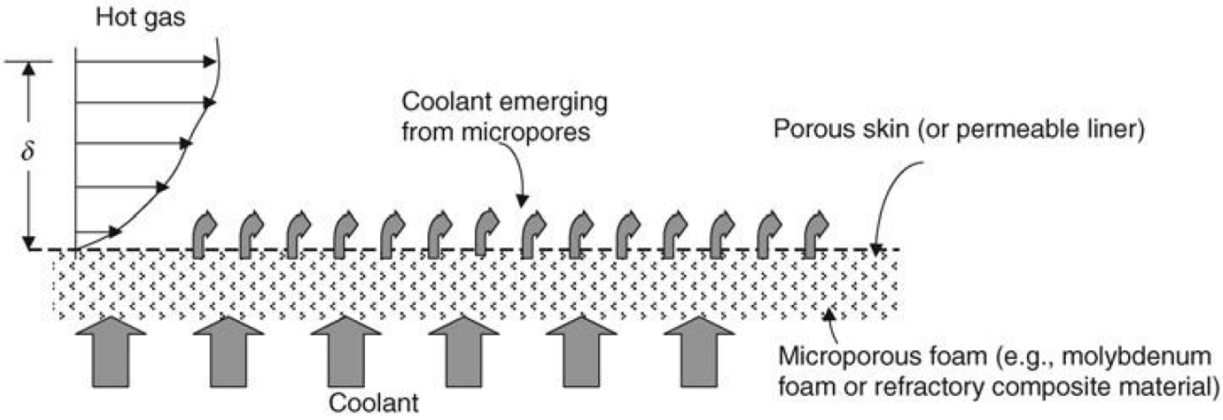

Figure 15: Visual Representation of Transpiration Cooling [19]

Unlike the other active cooling methods, transpiration cooling requires a much smaller mass flux of coolant. However, the micropores are on a scale of 10-100 micrometers, which makes them prone to getting clogged by emissions generated from combustion. Currently, there is no practical solution to unclogging them, which reduces the effectiveness of this cooling method. Furthermore, a microporous material is likely to have high manufacturing and repair costs, making transpiration an unattractive cooling method.

However, a potential new area for improvement in cooling technology is the use of lattice structures in turbine blades. As lattice structures are porous, they are expected to have significant heat transfer capabilities [43] while maintaining strength and being lightweight [17]. As such, our research focuses on the thermal properties of the lattice structures relating to turbine blade optimization, which could be beneficial to future developments of turbines. In this paper, three properties of heat and flow that affect jet engine performance will be investigated: thermal expansion, heat transfer, and velocity drop throughout the lattice structure. These thermal properties are discussed in further detail in section 4.1.

Lattice structures can be separated into several categories, such as lattice foams, Triply-Periodic Minimal Surface (TPMS) structures, and Chiral or Honeycomb structures. Each of these lattice categories has varying thermal or flow properties. TPMS structures are unique lattice structures created through additive manufacturing (AM), where each unit cell is a three-dimensional mathematically defined surface, as opposed to strut-based lattice structures (Ajit et al., 2018). TPMS structures are relatively new and complex structures, and consequently, there is little research done on their thermal properties, especially on specific properties such as the coefficient of thermal expansion. Most of the research is currently focused on using computational fluid dynamics (CFD) to analyze TPMS structures [5], with little research on physical experiments.

Given the lack of resources available to manufacture and accurately predict the coefficient of thermal expansion of a TPMS structure, it is likely for any analysis to be done mainly through simulation if a TPMS structure was to be chosen.

Unlike TPMS structures, Honeycomb structures have more thermal-related research and are simple to 3-D print for lab experiments. Honeycomb structures consist of a singular unit cell repeating itself to create a pattern. Honeycomb lattice structures can be varied by modifying the size and shape of the unit cell that makes up the honeycomb. These shapes can be regular hexagons, squares, or triangles but can be more complex by using chiral structures as a unit cell, creating a Chiral Honeycomb lattice structure.

As mentioned in the Design section, research has been done into designing lattice Honeycomb and Chiral structures with bi-material strips. These strips are made of two materials of differing thermal expansion coefficients and will flex in a certain direction under heating. The materials can be aligned so that their resulting expansions will counteract each other, resulting in little to no thermal expansion. This is demonstrated in Figure 16, where the yellow material has a low coefficient of thermal expansion, while the gray material has a higher one. Under heating, the grey material expands more than the yellow, causing the faces to bend. However, the bending also shortens the length of the faces. By modifying material specifications and dimensions, a custom thermal expansion coefficient can be achieved [26]. Figure 17 showcases a different approach in which two bi-metallic strips are joined to form one larger strip but the strips are flipped [25]. Under heating, the straight strips will start to bend around the circular joints, resulting in low thermal expansion as well.

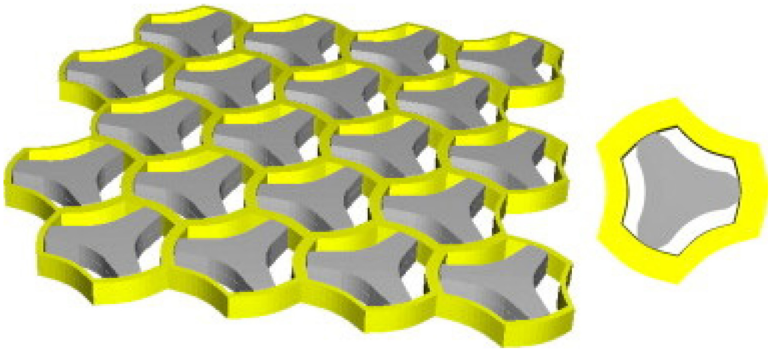

Figure 16: Sample Alignment of Two Materials for Zero Thermal Expansion. The two colors represent a material with different coefficients of thermal expansion. [25]

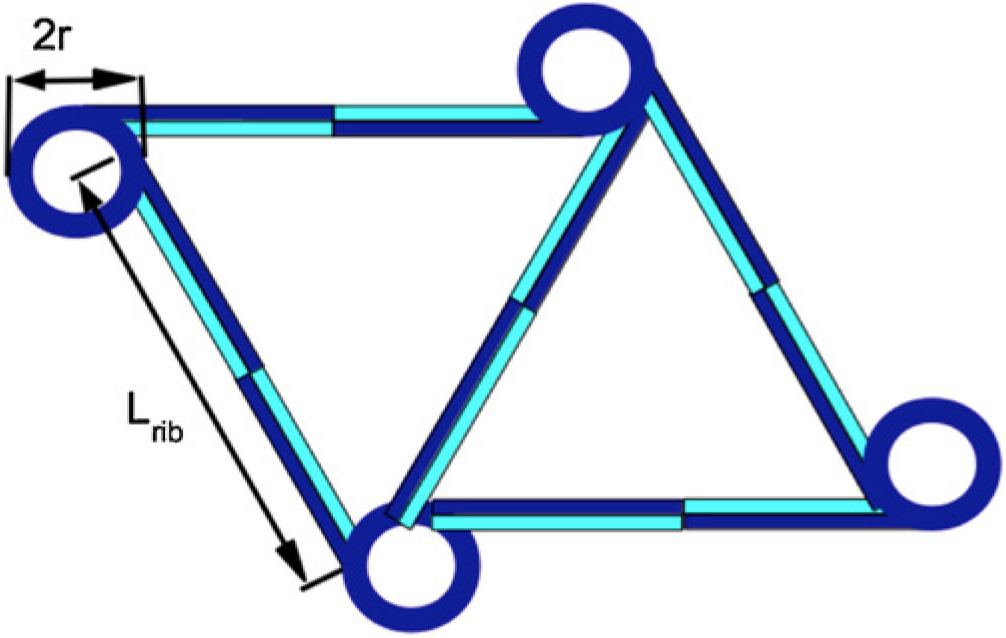

Figure 17: Different Alignment for Zero Thermal Expansion. The two colors represent a material with different coefficients of thermal expansion. [25]

For the structure in Figure 17, the coefficient of thermal expansion is calculated by $\alpha = \frac{r}{4\rho_s}\frac{1}{\sqrt{1+(\frac{2r}{L_{rib}})^2}}$, assuming thermal expansion occurs freely without constraint. Here, r is the outer radius of the node, L_{rib} is the length of each rib as seen in Figure 17 and $\rho_s = \frac{\rho^{-1}}{\delta T}$, which is known as the specific curvature. If the specific curvature parameter, k, of the material is known, then another equation, $\rho^{-1} = \frac{k}{h}$, can be used, where h is the thickness of the strips. If the specific curvature parameter of the material is unknown, then another equation, $\rho^{-1} = \frac{(\alpha_2 - \alpha_1)\delta T}{\frac{h}{2} + \left(\frac{2(E_1 I_1 + E_2 I_2)}{h}\right)\left[\frac{1}{E_1 \alpha_1} + \frac{1}{E_2 \alpha_2}\right]}$ can be used to determine ρ^{-1}. In this equation, E refers to the elastic modulus of the material, alpha refers to the coefficient of thermal expansion of the material, a is the thickness of each layer of the strip, δT is the change in temperature, $I = \frac{a^3}{12}$, which are the moments of inertia of each layer, and lastly, h is the thickness. The subscripts 1 and 2 refer to the separate materials used in the biomaterial strip [25].

Additionally, there have been significant reports focused on optimizing the Poisson's ratio of the structure at the same time as the thermal expansion coefficient. This can be achieved through certain star-shaped reentrant lattice structures made of two materials and modifying strut lengths and angles as seen below in Figure 18 [4].

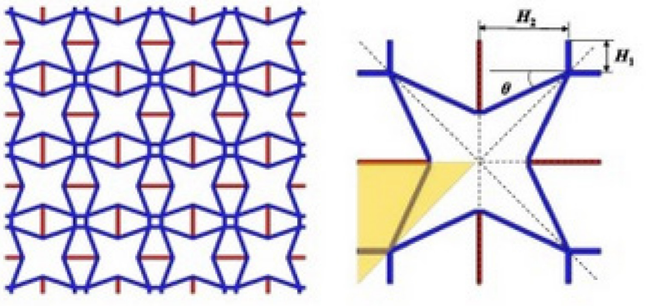

Figure 18: Example Design to Tune Coefficient of Thermal Expansion and Poisson's Ratio. The two colours represent a material with different coefficients of thermal expansion. [4]

These structures, just like ones in previous research, are also made of two different materials shown in blue and red. For this specific structure, Ai and Gao used ANSYS to model and simulate temperature changes and recorded changes in length between two nodes on different sides of the unit cell. Specifically, the equation $\alpha = \frac{\varepsilon_y^T}{\Delta T}$ was used, where α is the effective coefficient of thermal expansion, ΔT is the change in temperature and ε_y^T is the thermal strain in the y-direction and is calculated using $\varepsilon_y^T = \frac{(u_x^{A+})^T - (u_x^{A-})^T}{2(H_1+H_2)}$, where $(u_x^{A+})^T$ and $(u_x^{A-})^T$ are the nodal displacements at nodes A^+ and A^- due to the change in temperature [4].

From Ai and Gao's results, it can be concluded that for larger strut thickness, the coefficient of thermal expansion increases in a non-linear fashion as seen in Figure 19. Additionally, Figure 19 also shows that for increasing angle □, the coefficient of thermal expansion first decreases then stabilizes to a constant value as H2 increases. It is interesting to note that large changes in the coefficient of thermal expansion can be achieved by altering the angle and strut thickness.

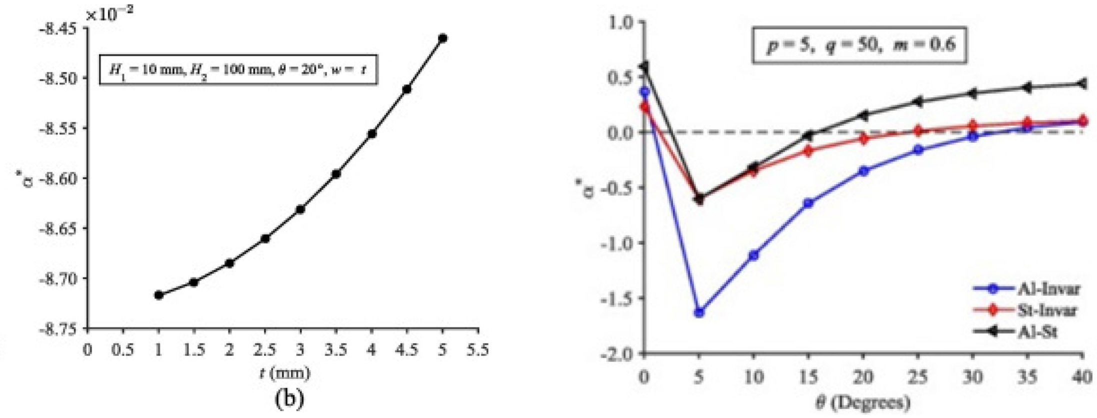

Figure 19: Results of Ai and Gao's Analysis on Thermal Expansion. Altering length, angle and material can result in a tailored coefficient of thermal expansion. [4]

In this study, the same analyses were completed for three other structures and it was concluded that by setting two to three length parameters, an angle parameter, and different material combinations, the coefficient of thermal expansion of a structure can be tailored specifically [4]. Similar research on this topic has shown that it is possible to design a structure with materials of positive coefficients of thermal expansion to have a significantly reduced coefficient of thermal expansion, but only in one axis [33] [45]. Given that Ai and Gao's analysis focused on thermal strains only in the y-direction, it is important to note that different axes may produce different changes to the coefficient of thermal expansion of the structure. Furthermore, the specific equations are only applicable to the same type of structure, meaning that a different unit cell design would result in their equations for a thermal expansion coefficient, which may be difficult depending on the complexity of the structure. Additionally, all of these tunable structures with zero or negative coefficients of thermal expansion consist of two materials with different coefficients of thermal expansion to allow for said tuning. While the biomaterial strips may be analyzed in a simulation, it is impractical to test them experimentally due to complexity and lack of resources.

Previous studies have shown that heat transfer through a Honeycomb structure is mainly due to heat conduction and partially due to thermal radiation, while heat transfer due to convection is generally negligible [9]. However, because airflow is considered for a jet turbine application, convection has a significant effect on heat transfer as well [52]. Therefore, our research will focus on heat transfer due to convection and conduction through the material.

1.1.4 Force Analysis

To understand how the designed lattice structures perform with applied loads, we must first know how forces propagate throughout the structures and how to calculate them. Figure 20 below is a Simplified Arch lattice structure. Although this is not one designed in this project, it is a rendering of the Simplified Arch structure and is similar enough to use for force analysis.

In the example below, a unilateral force is applied to the top of the lattice with the bottom of the structure being fixed in place. This simulation can be mimicked with a simple compression test in a laboratory setting [27]. However, it is useless to perform the test if overall and specific deformation is not calculated. Our experiments on the various structures would lose their validity without reliable quantitative measurements.

The force will distribute through the various struts of the lattice structure. It is critical to understand the deformation and stress fields in each strut.

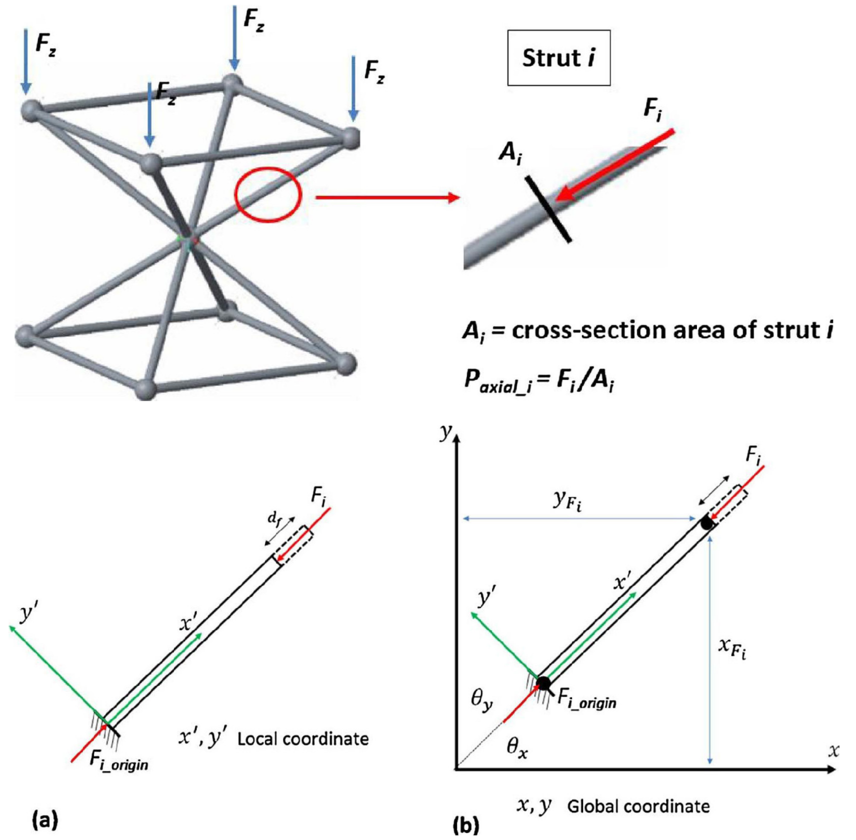

Figure 20: Simplified Arch Lattice Structure Forces [48]

According to the literature, "Design and analysis of strut-based lattice structures for vibration isolation" the force acting on a single strut can then be represented as the following:

$$F = \frac{A_s E}{l_s} df$$

Where A = area of the cross-section, E = young's modulus, l = length of the strut, and finally df= the deformation of the strut due to the force being applied.

$$A_s = \pi(\frac{d_s}{2})\text{^}2$$

The article, “Design and analysis of strut-based lattice structures for vibration isolation” notes that we can determine the axial force of each strut by finding the local stiffness matrix, K, and the local displacement matrix, D. In order to find the local stiffness matrix, K, we multiply F by a 2 x 2 matrix [48].

$$K = \frac{A_s E}{l_s}\begin{bmatrix} 1 & -1 \\ -1 & 1 \end{bmatrix}$$

Finally, the D matrix is…

$$D = \left[d_{fxy}\ d_{foxy}\ \right]$$

The force on each strut will now be equal to…

$$F = KD$$

Using the following equations, it is possible to determine the amount of deformation on each strut of the lattice structure. This model can also be applied to any strut-based lattice assuming that the struts are linear and not curved. A new model will have to be developed to determine the amount of deformation [48].

The process described above is very similar to how finite element analysis software works. Our team has utilized programs such as COMSOL and ABAQUS to understand how forces are transmitted throughout our lattice structures.

1.2 Overall Project Goals

The overall goal of this project is to determine the various structural and thermal effects of different lattice structures so that our team can determine the best design to implement in a turbine blade. Listed below are the team's main goals:

1. Familiarize ourselves and become proficient with appropriate CAD, FEA, and 3D printing software.
2. Create three design iterations of lattice structures that could be tested in the lab.
3. Print the lattice structures and perform structural and thermal tests on them.
4. Recommend a lattice structure that would best improve the structural and thermal integrity of a turbine compressor blade.
5. Learn the process of executing an experiment using laboratory equipment and using these results to validate simulated results.

1.3 Project Design Requirements, Constraints, and Other Considerations

The largest constraint on the project was the COVID-19 pandemic. Due to uncertain campus restrictions, a lot of planning was slowed, delayed, or not possible. Lab time was one of the main areas of the project affected. Lab space and time were uncertain for most of the project, which led tasks to continually be pushed back. Once lab time and space were available, the team accomplished as much as possible. Another constraint because of the pandemic, being limited in-person interaction amongst group members. Though group members met virtually accomplishing most tasks, smoother exchanges would have been possible with more interaction.

1.4 Project Management

As previously mentioned, the project consisted of three teams handling things related to design, structure, and thermal aspects. All students were advised under Professor Karanjgaokar and had different responsibilities split amongst each other. The entire team, sub-teams, and individuals communicated through text messaging and Zoom calls, until it was safe to meet in person. All work was shared in a google drive folder that all had access to. Documents that needed to be shared with Professor Karanjgaokar, were put into an OneDrive folder and sent to him.

The Design team consists of two members, Neal Keklik and Julia Rivelli.

Responsibilities:

- Researching lattice structures, how they can be modeled, and which software would be best to do it
- Fabricating lattice structures in Solidworks, FLatt pack, and NetFabb
- Taking feedback from other sub-teams and remodeling lattice structures / making new lattice structures that sub-teams recommend
- Communicating with all sub-teams to ensure all are on the same page and all teams have what they need to go further

The Structural Analysis team consists of Nicholas Pitti, Ivan Nikulin, and Matthew Withington.

Responsibilities:

- Researching lattice structures and how they can be structurally tested/which would be best for the given application
- Taking CAD lattice structures and running simulations with ABAQUS software

- Printing lattice structures in a 3D printer
- Running experiments on printed structures: three-point bending, tensile, and compression testing
- Comparing simulation results to experimental results

The Thermal Analysis team consists of Mike Lam and Cassandra Lira.

Responsibilities:

- Researching lattice structures, their thermal properties, and how they can be analyzed
- Taking CAD lattice structures and running various thermal and flow simulations with software such as ANSYS and COMSOL
- Running various experiments testing thermal expansion, heat transfer, and velocity change
- Comparing results from simulations to those found in experiments

In addition to the above responsibilities of all teams, the presentations occurred weekly to Professor Karanjgaokar. In the beginning weeks of the project, each sub-team would present a week, teams presenting every third week. Once the project advanced far enough all sub-teams presented weekly. Sub-teams met individually on a need-to-meet basis and one entire team meeting would take place at least once a week. The design team often acted as the team leads organizing meetings, slides, documents, and material order forms, in addition to leading most meetings, making for more organized project procedures.

1.5 Project Objectives Methods and Standards

Different objectives, methods, and standards were used by the different sub-teams. All were agreed upon as an entire team and were backed by research of Professor knowledge.

1.5.1 Design

The main objective of the Design team was to research, develop, and fabricate lattice structures that could then be passed to other sub-teams for further examination. This process led to the investigation into different software packages that would allow for lattice structures to be produced, which will be discussed in later chapters. Initial lattice structures were designed based on research and then tailored based on the feedback of the entire team. Tailored structures were also based on the capabilities of used software packages and time constraints discussed earlier.

1.5.2 Structure

The research was performed by the structures team to gain more knowledge on turbine blades and the typical loading conditions by these blades in a realistic scenario. The objective was to prove the validity of ABAQUS simulations by comparing them to experimental results. As a result, if the comparison yields similar data, the team can therefore use accurate results from Inconel 718 simulations to conclude the best-suited lattice structure for the turbine blade application. Throughout the process, the structures team also aimed to comply with as many standard test methods as possible, which was established by the World Trade Organization [40].

1.5.3 Thermal

The objective of the thermal team was to determine thermal flow properties that affect turbine blade performance and to test them accordingly on the lattice structure designs. Finite element analysis was conducted using COMSOL to simulate heat transfer, thermal expansion, and flow velocity through the lattice structures. The simulations in COMSOL were designed to depict real turbine blade conditions, including the temperature, material, and air flow velocity. Physical experiments using 3D-printed lattice structures were also created to verify the results. The physical experiments were replicated in COMSOL and used to determine the accuracy of the turbine blade simulations. The goal of the experiments and simulations was to find out which lattice structure, if any, could be most beneficial in terms of thermal properties for turbine blade applications. Standard SI units were used in all calculations. The physical experiments were controlled as much as possible and multiple trials were conducted for each.

1.6 Tasks and Timetable

To track progress our team designed a Gantt chart that included overall project deadlines as well as sub-team deadlines. This chart starts during the beginning of October 2020, when the heart of the project began, and extends through late March and the project's conclusion. The following chart displays a timeline that is as most accurate as it can be. Changes occurred often due to the COVID-19 Pandemic, as previously discussed. The dates on the right of the chart represent the start and end dates respectively.

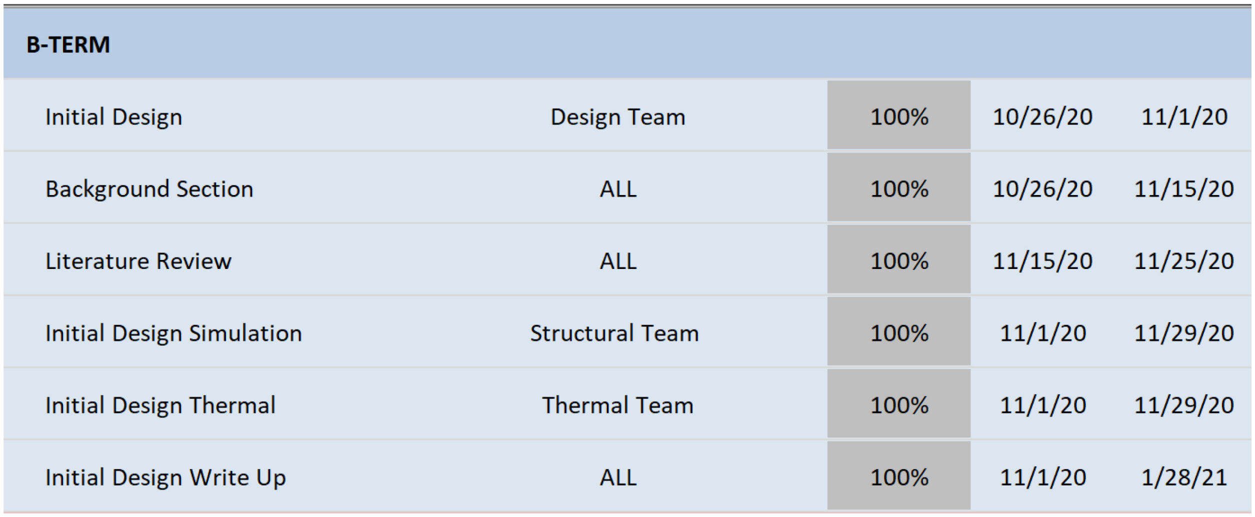

B-TERM				
Initial Design	Design Team	100%	10/26/20	11/1/20
Background Section	ALL	100%	10/26/20	11/15/20
Literature Review	ALL	100%	11/15/20	11/25/20
Initial Design Simulation	Structural Team	100%	11/1/20	11/29/20
Initial Design Thermal	Thermal Team	100%	11/1/20	11/29/20
Initial Design Write Up	ALL	100%	11/1/20	1/28/21

Figure 21: B-term Schedule

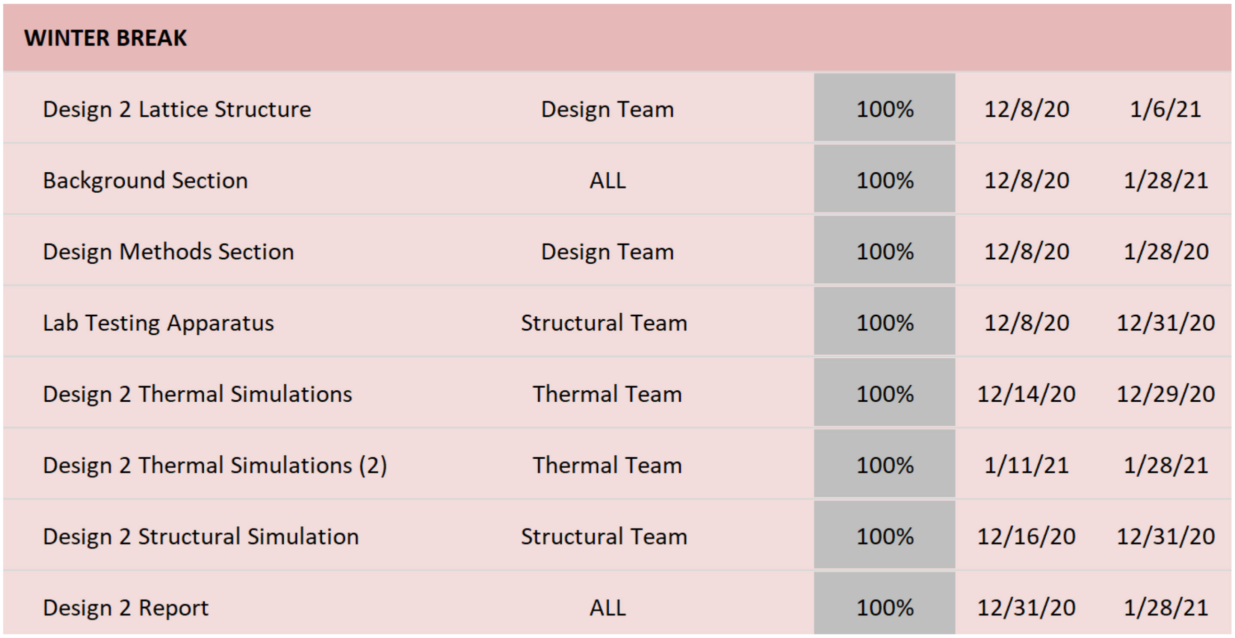

WINTER BREAK				
Design 2 Lattice Structure	Design Team	100%	12/8/20	1/6/21
Background Section	ALL	100%	12/8/20	1/28/21
Design Methods Section	Design Team	100%	12/8/20	1/28/20
Lab Testing Apparatus	Structural Team	100%	12/8/20	12/31/20
Design 2 Thermal Simulations	Thermal Team	100%	12/14/20	12/29/20
Design 2 Thermal Simulations (2)	Thermal Team	100%	1/11/21	1/28/21
Design 2 Structural Simulation	Structural Team	100%	12/16/20	12/31/20
Design 2 Report	ALL	100%	12/31/20	1/28/21

Figure 22: Winter Schedule

C-TERM				
Design 3 Lattice Structure	Design Team	100%	1/11/21	1/18/21
Methods Section of Paper	ALL	100%	12/31/20	1/28/21
Design 3 Simulations	Thermal, Strucutral Team	100%	1/18/21	2/10/21
Final Draft of Paper	ALL	100%	2/11/21	2/20/21
Thermal Experimental Setup	Thermal Team	100%	2/8/21	2/15/21
Thermal Lab Test	Thermal Team	100%	2/15/21	3/3/21
Lab Testing on Design 3	Design Team	100%	2/20/21	3/7/21
Final Paper	ALL	100%	3/7/21	3/17/21

Figure 23: C-term Schedule

2. Design

The design of lattice structures took place using three different types of softwares. Different techniques were used to fabricate six different lattice patterns and structures. Once made in software designs were sent to other sub-teams for use.

2.1 Methodology

Initially, when thinking about possible designs to explore, a couple of different available software packages and their capabilities were explored. Early designs were done in Solidworks because of teammates' familiarity with the software, which is how the first iteration of designs was fabricated. These designs were basic and simple enough to be a starting point for the project. The team's procedure then switched to more complex designs that would be more practical for the given application, a turbine blade. This switch came from more research and input from other teams. Once this process began, designs were tailored and created based on the needs of the entire team.

2.2 Software

Three different softwares were used when fabricating lattice structures to be printed. These softwares, their capabilities, and the extent of their use are described below.

2.2.1 Solidworks

The most familiar software to the team when beginning work was Solidworks, which is what was used for the first iteration of designs. Solidworks is a solid modeling computer-aided design (CAD) and computer-aided engineering (CAE) computer program published by Dassault Système. One of the major disadvantages of using Solidworks is that when designing lattice structures the team was essentially starting from scratch. In other words, there are no lattice functions that allow for fast fabrication. All designs made in Solidworks start with a singular two-dimensional single-cell lattice and can then be expanded using extrusions and the pattern function, which is a long tedious process. One of the main advantages of the Software was diversity in file type, when exporting the structures files could be parts, iges, autoCAD, etc. making its compatibility with other softwares used by other sub-teams easier.

However, another major disadvantage is the lack of processing power the team had access to. All team members worked remotely from laptops for the most part. Trying to develop increasingly more complicated designs such as those in design iterations 3 and 4, became not only more time-consuming but would result in crashes as well. Because of this, the team reached out to IT services at WPI to try and establish a server where work could be done. Though this helped, other less complicated, and less time-consuming softwares were sought and proven to be more advantageous.

2.2.2 FLatt Pack

The Functional Lattice Package (FLatt Pack) is a software developed at the University of Nottingham for the design of lattice structures for additive manufacturing research. The software is maintained by Ian Maskery, who the team reached out to in the early stages of the project. He provided the team with the software, which is capable of making a unit cell lattice structure in a few short steps, choosing geometry and dimensions. The software has 23 lattice cell types, including surface-based cells, strut-based cells and honeycombs, cell size and volume fraction control, including functional grading and user-defined volume fraction distributions (e.g. from topology optimization), and choice of standard lattice shapes or imports a geometry to be latticed.

Additionally, the software allows for designs to be exported as STL files for printing or Finite Element for analysis.

Ultimately the software seemed to be too new for use in this particular project. Though there were many default geometries, it was difficult to accurately import designs made in other softwares. FLatt pack also did not have as diverse of an export pool as other softwares. Therefore, the use of this software was eventually determined to be unuseful and other paths were explored.

2.2.3 Netfabb

Netfabb is a fabricating software that allows users to tessellate lattice structures within predetermined AutoCAD designs. One of the major benefits of this software is the lattice structure commander function. This tool allows the user to pick a lattice that has already been uploaded into the library of Netfabb and tesselate it within an AutoCAD file. The size, thickness, and density of the lattice can be changed to any desired value. Besides, the lattice can be meshed over with the function, "BREP to Mesh". This allows the user to convert an stl file into a parametric file which then can be used for finite element analysis software simulations. The file can also be prepared for 3d printing and a printer can be connected directly to the software.

The usefulness of Netfabb is dependent on two main factors, the complexity of the design and the power of the computing system. The design team used Netfabb to not only design and fabricate our lattice structure designs but also mesh the structures so that the other teams could then perform simulations. However, the more complex the design the less likely the mesh will complete. Therefore, ensuring the simplicity of the lattice structures was essential. One way to reduce the complexity of a design in Netfabb is to round off any sharp edges. The software can mesh rounded corners far better than sharp corners and will subsequently reduce the amount of time for the mesh to generate. Reducing the resolution of the mesh will also reduce the amount of time needed for the mesh to generate. Another factor that will determine the applicability of Netfabb is the operating system that the software is running on. A computer with only integrated graphics will be limited to the amount of designs that can be generated. On the contrary, a computer with a powerful dedicated graphics card can generate meshes for more complicated structures.

2.3 Design One - Orthogrid, Isogrid and Honeycomb

The first design completed was that of a square grid. This allowed the team to gain some familiarity with features in Solidworks such as the pattern functions, the sizing functions, and extrusion. The Orthogrid is shown in Figure 24. This also proved valuable for other sub-teams, as it could be used in some beginning flow simulations in softwares like ANSYS, ABAQUS, and COMSOL.

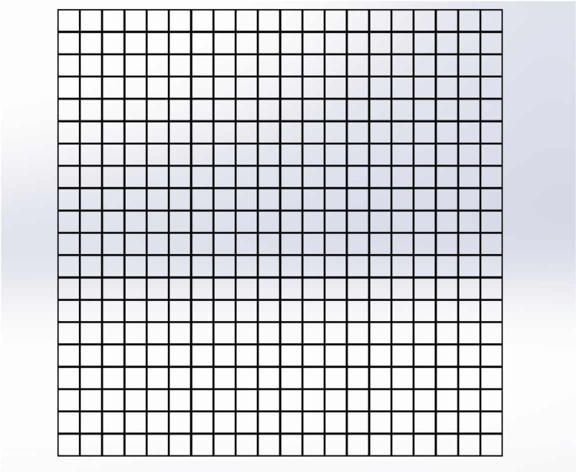

Figure 24: Orthogrid Designed in Solidworks

The next design was also created in Solidworks. The geometry is closer to that of an Isogrid and was not used in any simulation, but rather was another stepping stone for figuring out how to fabricate more complex structures. The lattice below in Figure 25 , shows some integration of Honeycomb features as well.

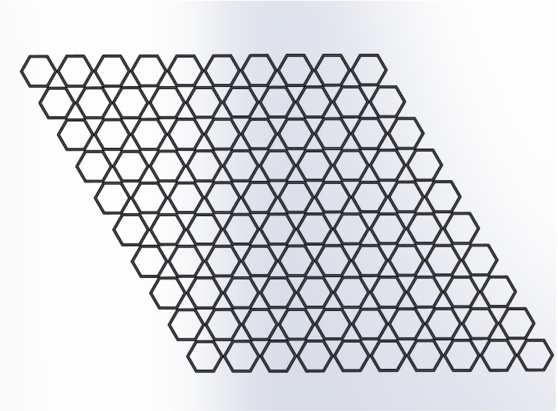

Figure 25: Isogrid Designed in Solidworks

Figure 25 led to the design of a typical Honeycomb structure, which was the next step in these preliminary designs. As described in the earlier sections, Honeycomb structures are strong candidates as they have many advantageous mechanical properties. Figure 26, was generated in Solidworks and will go on to be used in simulations both experimentally and theoretically by the Structures and Thermal sub-teams.

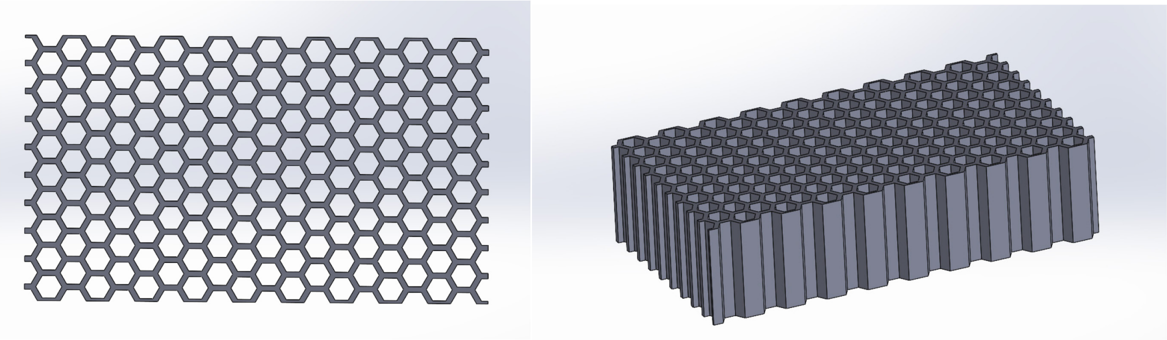

Figure 26 : Honeycomb designed in Solidworks

The structure on the left showing the front view of the 2D lattice and the right side showing the extruded view. The time taken to make the above three designs were great and tedious. The Design team began looking into some software alternatives, to make more structures faster. FLatt pack, a lattice structure generation software, was used to generate the following honeycomb-like structure, Figure 27.

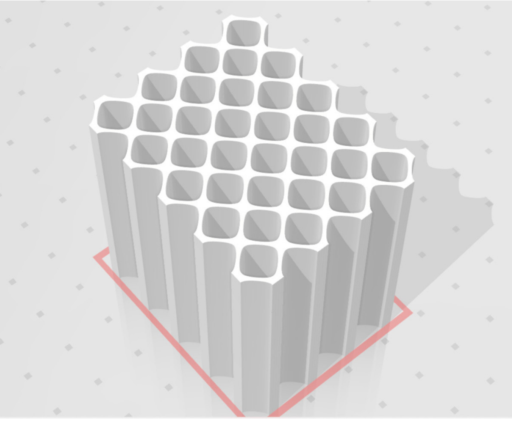

Figure 27 : Honeycomb design in FLatt pack

Using the FLatt pack, this structure was generated in a fraction of the time it would take to generate in Solidworks. However, as previously described, the software did not possess the same geometries of what was needed to continue, which is why the FLatt pack was eventually steered away from, as discussed earlier.

2.4 Design Two - Gyroid, Simplified Arch

The previous design iteration consisted of an Orthogonal lattice structure and an Anisogrid lattice structure. Our team decided to pursue these designs as first iterations because they were easy to understand and test. This was especially important because of the lack of familiarity that our team had with additive manufacturing software such as NetFabb and simulation software such as Ansys. Therefore, our first design enabled us to become more experienced with the software that we would need to use on my complex lattice structures.

For our second design iteration, we focused on a variation of the Arch lattice structure as well as the Gyroid lattice structure. A Traditional Arch design lattice structure can be found below in Figure 28. The Arch lattice structure that was used in design two featured straight struts rather than curved struts. This lattice structure is also known as an “X” structure due to the resemblance of the letter, x when viewed from the side. The unit cell of the Simplified Arch design can be found below.

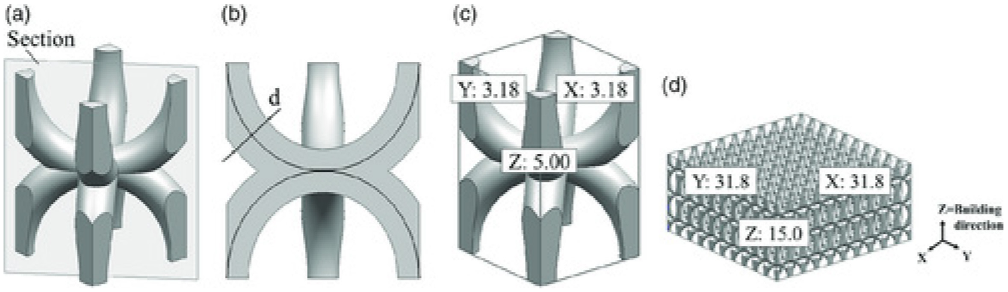

Figure 28. Traditional Arch Lattice

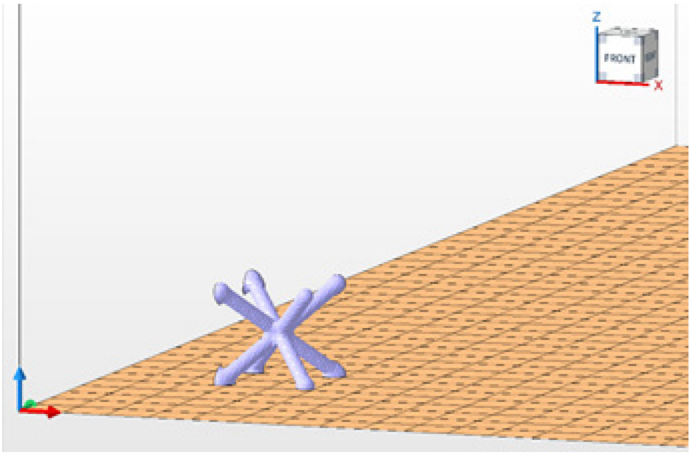

Figure 29. NetFabb Simplified Arch Lattice

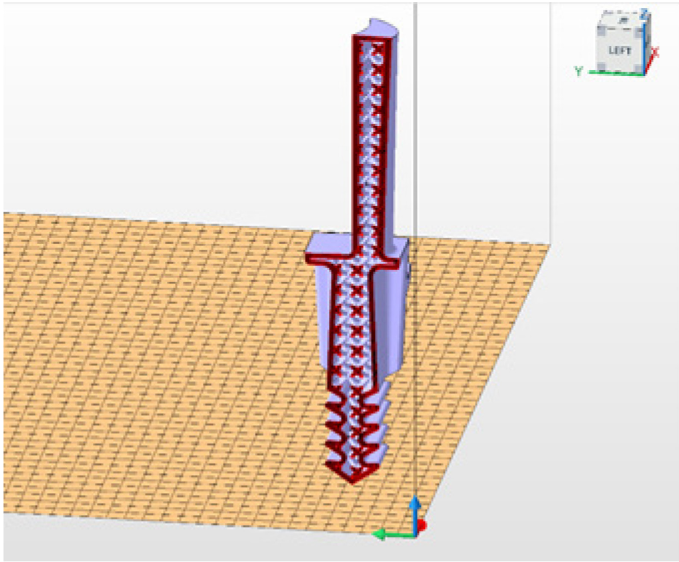

Figure 30: Simplified Arch Lattice Tessellated into a Turbine Compressor

In addition to the Simplified Arch lattice, a Gyroid design was also fabricated during the second iteration. The key difference with the Gyroid design as compared to the Simplified Arch design is the complexity of the lattice. The Gyroid unit cell has no sharp angles whatsoever in the lattice however, the Simplified Arch has multiple. The sharp angles create sheer points and when a load is applied to the lattice these sheer points are often the points of failure. The Gyroid does not have any of these sheer points and thus makes it optimal for our team’s application.

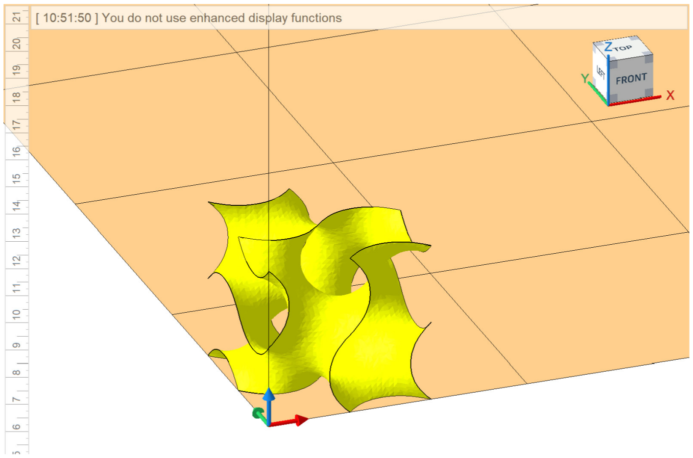
[10:51:50] You do not use enhanced display functions

Figure 31. Gyroid Unit Cell

2.5 Design Three - Traditional Arch

For the last and final design iteration, a Traditional Arch lattice structure was utilized. The main difference between the Traditional Arch and Simplified Arch design from the second design iteration is that the struts are curved rather than straight. Below is a unit cell of the Traditional Arch design.

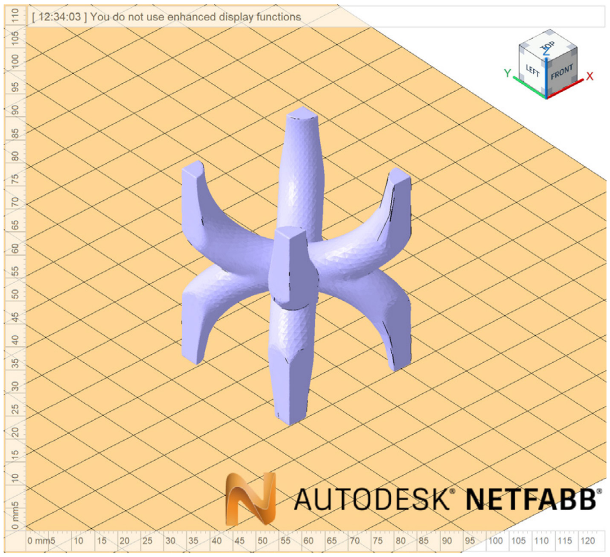

[12:34:03] You do not use enhanced display functions

Figure 32: Traditional Arch Unit Cell

Although the Traditional Arch unit cell has curved struts there are sharp edges present. Specifically, they lie at the junction of the bottom and top arch of the unit cell. Similar to the Traditional Arch, these sharp points allow for a load to concentrate subsequently turning into failure points if the load is great enough. The unit cell above was tessellated into the shape of a turbine compressor blade, a rectangular prism, and finally a cube for testing.

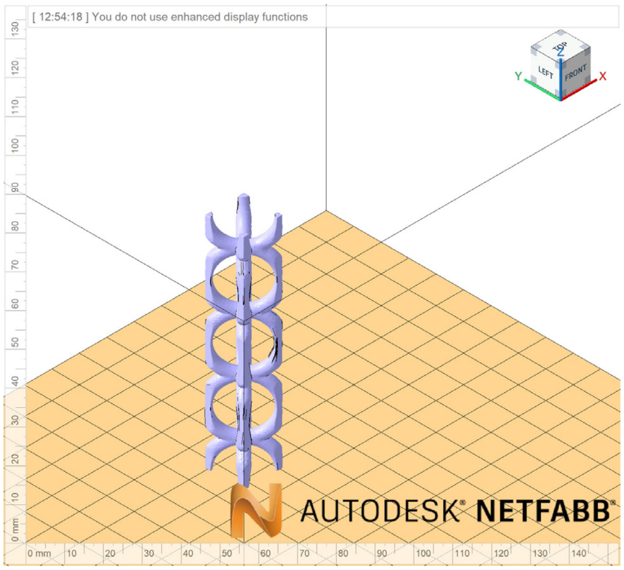

[12:54:18] You do not use enhanced display functions

Figure 33: Traditional Arch Rectangular Prism

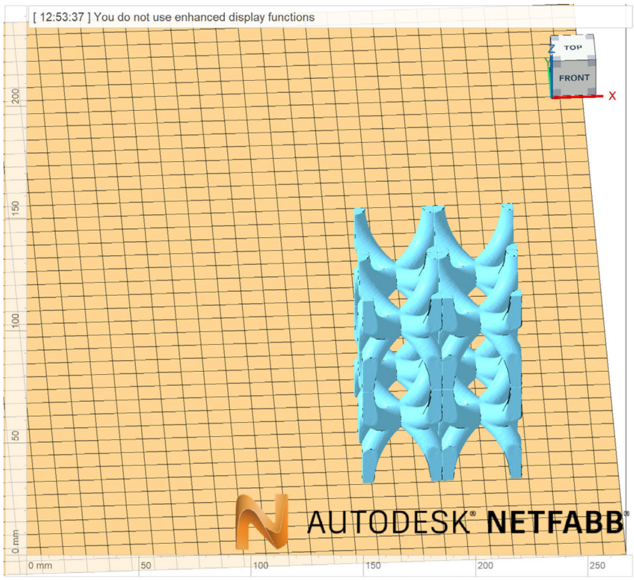

[12:53:37] You do not use enhanced display functions

Figure 34: Traditional Arch Cube

2.6 Discussion

As discussed in the individual sections above, there were many lattice structures researched and designed, using a variety of different softwares for fabrication. Honeycomb and Orthogrid structures proved to be the easiest to design and produce but not the most structurally beneficial, which will be described in later sections. The Simplified Arch is easy to manufacture, easy to model, has beneficial structural components and features, with lots of shear points. While the Traditional Arch is also easy to manufacture, has a lower shear point, but is much more complex to model. A Gyroid lattice is the most difficult to design, model, and print (printing being near impossible for the team). The structure requires a lot of computing power to use in any simulations and softwares, however demonstrates an advantageous balance between flow and strength. Furthermore, the Gyroid lattice proved to be extremely difficult to print. There was no way to test such lattice without the ability to effectively print it. Ultimately, the recommendation from the Design team would be to further investigate the Simplified Arch, with straight struts. The structure's simplicity in design and modeling makes it the quickest to manufacture. Additionally, the structures proved to be easily customizable in the changing of features such as length, width, overall dimensions, etc. while also having a good balance of flow and strength.

3. Structural Analysis

The investigation of the structural properties of the lattice structures included the analysis of three forces directly relating to the jet engine turbine blade application. Extensive knowledge is also helpful regarding the 3D printer to better understand the properties associated with the prints. The tests performed on the structures printed were conducted to validate the accuracy of the ABAQUS simulations.

3.1 Methodology

3.1.1 3D Printer

The Peopoly Moai 130 is a stereolithography (SLA) 3D printer, which is a type of photopolymerization printing, and was the printer used for the project. The part prints upside down, where the built plate lifts as the layers are selectively cured onto the part. At the beginning of the project, there was an initial choice between using a fused deposition modeling (FDM) printer or the SLA printer for the project. The chosen printer was the Peopoly Moai 130 SLA printer because this 3D printer would print our structures with better resolution and strength, despite the structure’s complexity. However, to get the results desired, one of the most important lessons that were learned is that “3D printing is more of an art than it is a science” (Professor Nikhil Karanjgaokar 2021). As a result, there were multiple failed prints at the beginning while the printer was fine-tuned and tested under different settings.

Table 1: Final Settings Used for the Peopoly Moai 130

X Size	900

Y Size	900
X Deviation	100
Y Deviation	100
Smooth	50
Z Motor Speed	8
PM Motor Speed	40
Laser Power	56
XY Speed Set	4
Z Reset Position	1877
PM Reset Position	40
Z Follows	40
Compensate X	100
Compensate Y	200
Z Initial Speed	2
PM Initial Speed	10

As mentioned in section 1.1.2, researching how additive manufacturing takes place in the field gave insight as to what to look for when learning about the Peopoly Moai 130. Print errors are a perpetual problem in any method of 3D printing, thus it was important to learn how these errors can occur and ways to mitigate them in practice. Forums and other public blogs were utilized heavily to read what problems real people are running into, and how they troubleshoot the issues. Many times, a dilemma that our team comes across has already been asked on the forum, with a response from other people troubleshooting the same problem, or the Peopoly company on methods to correct it. The largest obstacle in this respect was when the different printer settings were tested, more specifically finding the proper value for the laser power of the printer [30].

The ultraviolet (UV) light in the laser is what cures the resin. The energy density of the laser dictates how powerful the laser is, as well as how long the laser is exposed for, and how large the laser spot size is. For example, turning the energy density of the laser higher will provide quicker curing due to the laser power, with larger spot size, and a slightly longer exposure time [37]. The energy density is considered the “laser power” in Table 1 for the Peopoly Moai 130’s case. The default laser power set by the company is at a value of 58 [30].

Initially, the settings were on the default values given by the company, yet on the first print, the acrylic tray and silicone layer had partially melted. After researching, along with further trial and error, the team acquired new information about the nuances of vat polymerization. The laser power was too high, and only after multiple failed prints and a melted silicone later was it realized and corrected. Checking where possible error takes place in between prints is critical, as many times print errors can be prevented with the proper measures. Over time with more prints came experience mitigating these issues before they arise, and learning new problems that may need troubleshooting. Small factors as little as the color of the resin being used can require nuanced settings of the printer to receive an accurate final product.

The liquid thermoset resin used was ordered from the Peopoly Moai 130 printer website. It is called the Peopoly Hi-Temp Nex Resin, with the “natural” color (a light peach color). The material is a thermoset polymer, which is different from a thermoplastic, as the curing process from liquid thermoset resin to solidified plastic is irreversible. Thermoplastics become soft and pliable under high temperature and can repeat the process of melting, reshaping, and solidifying many times [41]. The cured thermoset plastic will not melt again when exposed to high temperatures, making it an ideal material for thermal testing.

As mentioned before, many early attempts resulted in failed prints. Improvements were made to the processes to achieve desired results, and tricks learned from the internet were used to aid the procedure. An example of an improvement we made to our prints was adding a small heater inside the print area, as the resin becomes more fluid and thus prevents warping [37]. Warping occurs when the material inside the part cools at an uneven rate compared to the plastic on the edge of the part. The result of warping is the curling up of corners, deforming the part. At times, the beginning layers of the print did not stick to the build plate, which results in nothing being printed. To resolve this issue, the build plate was wiped dry first, then coarse sandpaper was applied to the surface of the plate. After cleaning the excess residue with ethanol and drying it with the compressed air, the build plate will have a better-suited surface to allow the resin to stick when struck by the laser. A nuance of the printer that was learned the hard way was its tendency to partially melt/deform the beginning 1 or 2 cm of the part. To adjust for this complication, every part printed had about 2 cm of a solid base, to allow room for error.

3.1.2 Post Processing

When the part is properly printed and pending the result comes out accurate, the post-processing phase of the part begins. The build plate is first removed from the printer and the part is taken off. Failure to remove the build plate before the removal of the part can result in the printed part/printer to break, and/or a mess. At times, depending on the geometry of the part, it can be difficult to remove from the build plate. The solution found was to use a razor blade around the edges and corners, being patient. Eventually, after enough of the side and corners have been lifted, the part will come off of the build plate in one piece. Following its removal from the build plate, the excess resin must get cleaned off.

Ethanol will clean the part better than soap and water. Due to the complex geometry of the lattice structure printed, inside of the part there remained excess resin that could not be cleaned. Instead, following the part's fabrication, it was placed into a container where it was submerged in ethanol overnight. When the part was retrieved the following day, a sticky residue remained on the outside of the part. To remove it, the specimen is scrubbed with ethanol and a toothbrush. This process is repeated using soap, water, and a toothbrush again, and the result is a clean finish on the part with no leftover residue. Finally, the part is blown with air from an air compressor until dry, and placed into the team's homemade UV oven.

Figures 35 (left) & 36 (right): Homemade Ultraviolet Oven Created By Team

As shown in Figures 35 and 36, the team took a cardboard box and lined the inside with sheets of aluminum foil. A hole was cut out of the side so the UV light snugly fit inside of it. The desired outcome is that all sides are cured evenly throughout, which is why aluminum foil was taped on the inside. However, the time any part spent in the UV oven depended on its geometry and size. An example can be a rectangular part, where a few sides will be directly exposed to the UV light, yet the backside is receiving indirect UV light from the aluminum reflection. The solution was the part would cure for multiple days, and a member of the team would go into the laboratory and manually reorient the piece. The final step before the part is ready for experimentation is one final wash with soap and water, to remove any remaining stickiness from the part.

Once every other week, the team removed the build plate to do a full cleaning on it, and reapply the sandpaper. The resin is wiped with dry paper towels first, and the remainder is cleaned with ethanol. The vat that held the resin has also been cleaned a total of two times, once due to the melted acrylic as mentioned before, which needed to be replaced. First, the team emptied the resin into another container for future use. Dry paper towels are used to get the bulk of the resin up, then ethanol is used to wipe the vat clean. Once the station is cleaned and prepped for future use, the next step in the experimentation process is testing recently printed parts with the Instron stress tester.

3.2 Instron Testing

Instron is one of the leading companies in the industry that creates machines designed for the mechanical testing of materials. The Instron 5944, as shown in Figure 37, was the mechanical testing machine used to experiment with the structures printed. With an upper limit of 2 kN (450 lbf), this machine was ideal for experimentation on plastic structures.

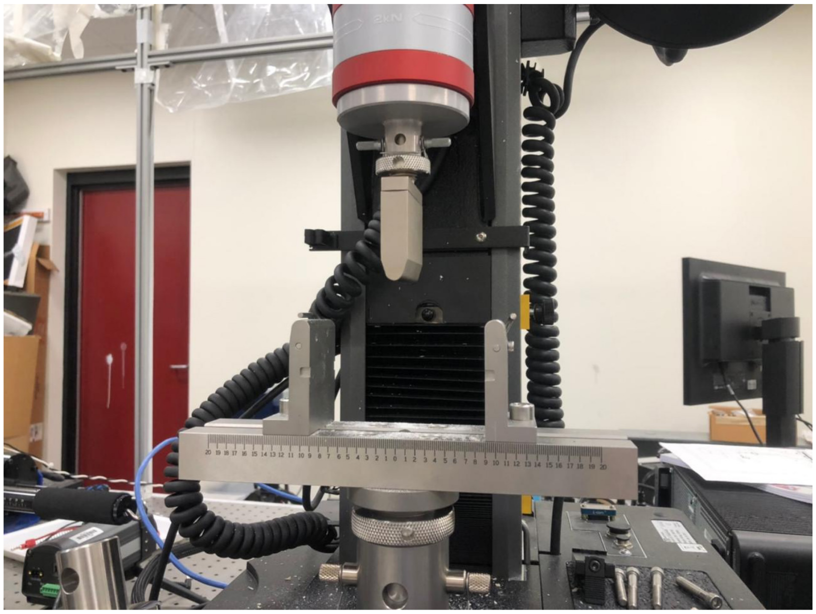

Figure 37: The Instron 5944 Equipped with Three-Point Bending Fixtures

Three types of tests were conducted on the lattice structures: A three-point bending test, a compression test, and a tensile test. Tests were used to see how the structures would fare under the conditions of each test, the load is evenly distributed to ensure the validity of the experiment. As a result, lattice structures both with and without a skin were printed; the tensile and compression tests were conducted using no skin, with an evenly distributed load throughout the surface. However, the three-point bend test would not distribute the load evenly across the surface without having a skin. Thus, the structures with skin were used for the three-point bend test.

Although the three-point bend test had no pre-processing requirements for the material, the compression and tensile tests required extensive preparation before the test. Only the Arch lattice structure and its perpendicular variation structure were tested under compression and tensile stress. This is because the honeycomb structure is considered a 2D lattice structure. The method for conducting the compression and tensile tests was to use Gorilla Epoxy adhesive and attach both sides of the structure to machined aluminum fixtures.

3.2.1 Pre Processing for Compression and Tensile Tests

The first step of the process was machining the aluminum into the shape desired, which was a square with a rectangular prism sticking out in the middle, to allow the Instron machine to clamp the system without damaging the part. The aluminum fixtures were manufactured in Washburn Laboratories on campus by a colleague of one of the team members. Two of them were created, with the geometry and dimensions displayed in Figure 38.

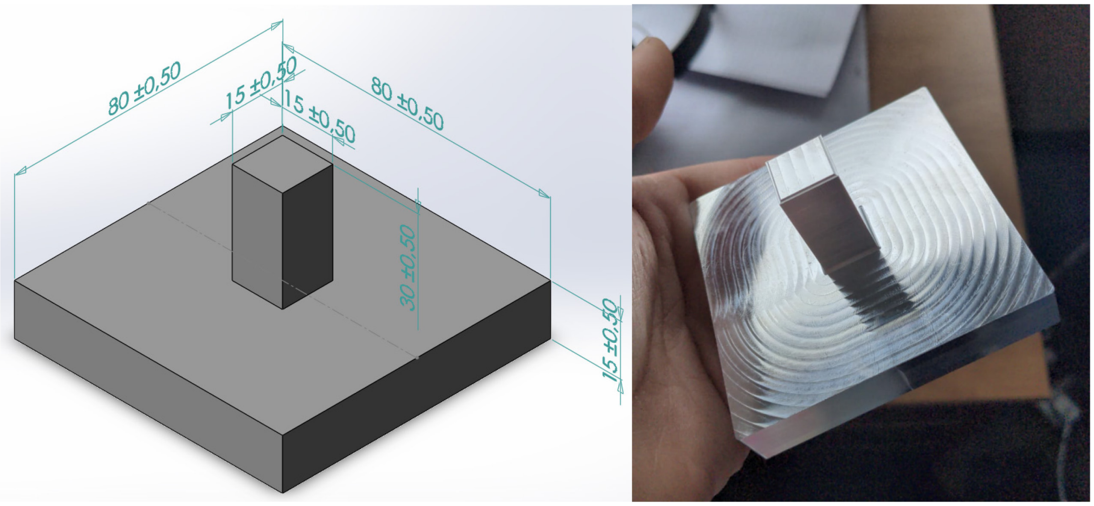

Figure 38 (left) & Figure 39 (right): Machined Aluminum Fixtures, with Dimensions in Millimeters in Figure 38

As mentioned in section 3.2, Gorilla Epoxy was used to attach the structure to the machined parts. This process was extensive and time-consuming, as there were many steps and factors to consider. The initial step taken was administering the adhesive to the middle of the fixture, and placing the side of the structure with the solid bottom onto the glue. Additional epoxy was provided, assuring that the weak point of the structure would not be the glue. A factor to keep in mind during this step was to align the bottom of the structure with the fixture, such that there is no tilt or bias in any given direction. This is a key step; if the structure is tilted even slightly anyway, the test could yield poor results.

The following step is just as important as the first. Assuming the structure is properly aligned with the fixture, this step focuses on aligning the fixtures across three axes. After letting the adhesive set long enough to hold the structure in place and not drip, the fixture-structure system was placed on its side, against the table. Two metal plates were placed on both sides, thus aligning the fixture on 3 axes. A clamp was then used to hold the fixture between the two plates. The second fixture was then aligned with the structure, as well as the three axes, and clamped into place using a second clamp.

Figure 40: Clamped Glued Fixture

The fixture-structure system was then stood up as shown in Figure 40, and more Gorilla Epoxy was then placed inside the struts of the Arch lattice. A pipette was used to ensure that there was a healthy layer of epoxy in between and around the struts of the bottom of the structure-fixture connection. The glue must be made and pipetted into the desired area within approximately 3-5 minutes, as the epoxy will become too hard at that point to move fluently. It is wise to keep caution as well, assuring that when someone is handling this process, they are using a laboratory coat and vinyl gloves. Another safety factor to keep in mind is the reaction temperature of the Gorilla

Epoxy, which comes in a dual syringe container, with 50/50 epoxy and hardener. When squeezed out in equal increments and mixed, this is what creates the final adhesive. During the mixing and hardening process, the adhesive becomes very warm, and can potentially burn if one is not careful.

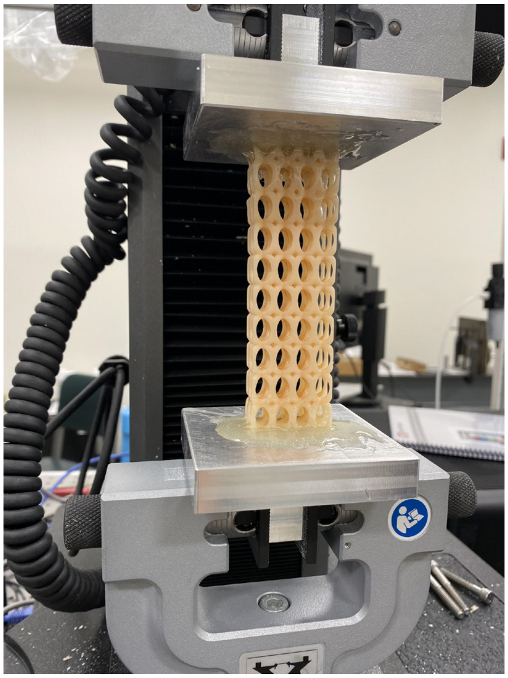

Figure 41: Final Setup of the Compression and Tensile Tests

The final step after administering the adhesive is to wait until the glue is set enough, such that the structure does not move. The team established a corner where the fixture-structure system could harden and set longer in the lab. The clamps remained until the following day when the team came ready to remove the clamps from the system and perform the test.

3.2.3 Post Processing for Compression and Tensile Tests

Following the compression and tensile testing procedures, the issue arises where the glue and structure must be removed from the fixture. After some trial and error, the team optimized post-processing to be efficient, and quick. The structure was first sawed on both sides, as close to the glue as possible. The Gorilla Epoxy is almost impossible to remove without the employment of a solvent. Acetone would be used to let the fixture soak and dissolve some glue, allowing for easier removal. The processes involving acetone were performed under the fume hood, as acetone can be dangerous to inhale. The two fixtures were placed into the two acetone-filled containers, glue-side down.

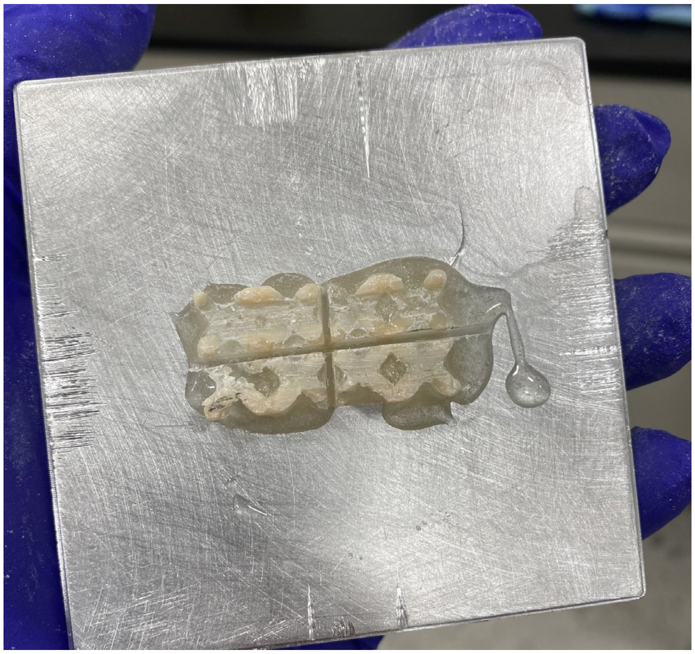

Figure 42: Cross-Section that was Sawed into the Structure

However, the dilemma that arose was that it was taking too long, as the glue was thick and the acetone only dissolved the outer layers. The solution found was to saw a cross-section, shown in Figure 42, into the structure and glue using a hand saw. Doing so allowed for a more inner surface area of the glue to be exposed to the acetone, raising the speed of dissolving. After the sawed structure system is placed into the vat of acetone, they were left to sit for approximately 15 minutes. After sitting in the acetone the fixtures were removed, and thin razor blades were used to scrape the glue. Fortunately, the glue comes up still attached to itself, which makes it easier to remove, as a technique was to scrape up a piece large enough to hold between your fingers then pull it up.

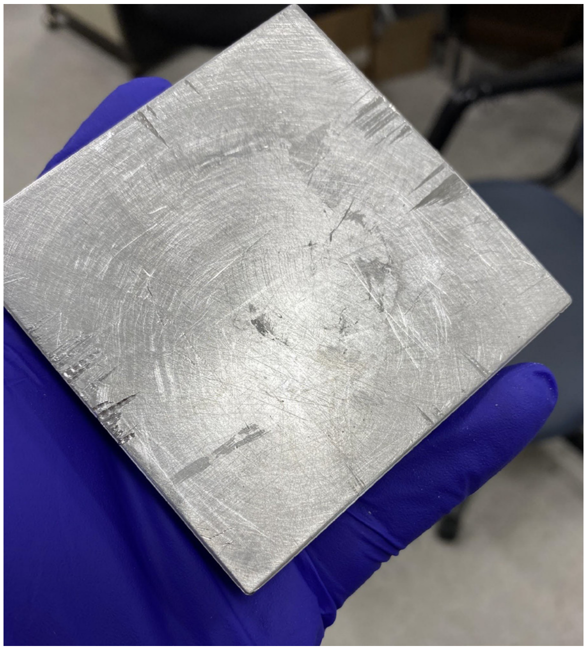

Figure 43: Fixture Surface Following Glue Removal

Another technique used was with a larger metal scraper, where it was placed inside the cross-section lines, then leverage was used to pry the glue/structure off. Many times, this technique yielded large quantities being broken off, making it the most effective method of removing the glue. Shown in Figure 43, is the fixture surface following the glue removal.

3.3 Design One - Orthogrid and Honeycomb

Orthogrid and Honeycomb lattice structure variants were provided in the first iteration of the design by the team responsible for lattice structure design. During the initial background research and literature review that was conducted by the team responsible for structures, the possibilities of applications of the first two structures were assessed. The Orthogrid lattice was found to be most common and most effectively used as merely a structural reinforcement. The Orthogrid structure was found to be used on larger scale objects, such as various wall supports, ship hull and body reinforcements, objects of a larger scale than turbine blades. It was established to serve a purpose different from that which was intended by the Structures team. Due to the differing primary application and purpose of the structure, the structural analysis team terminated the consideration of the Orthogrid lattice on the stage of background research and literature review and did not proceed with the structural analysis of the version lattice design. The Honeycomb lattice structure was also found to be unfit for the desired application in turbine blades, due to the results of initial research and project problem and goal establishment. The Honeycomb structure was found to be a version of a two-dimensional lattice structure, and due to that not suitable for the desired application. The two-dimensionality of the design was expressed in the drastic differences in isotropy of structural-mechanical properties. The Honeycomb lattice structure was also found to strictly limit the direction of airflow, and could not be placed inside a turbine blade for cooling due to the inherent design of the unit cells, which were merely hollow hexagonal prisms with set wall length and wall thickness, but a varying prism height. Unlike the Orthogrid Lattice, the Honeycomb lattice was still tested by the Structures team. The main purpose for testing and analysis of the Honeycomb lattice structure was to take advantage of the design's simple structure with a two-dimensional base to validate the Finite Element Analysis through laboratory testing. The Honeycomb lattice samples were tested with the Instron three-point bending fixture to obtain data for validation. That particular lattice structure was expected to fracture under the applied load, but proved to deform only elasticity, absorbing all of the applied force without fracturing and returning to the initial state at the end of the experimental loading process. In short, the Structure team established that the lattice designs of the first iteration of the design process: the Orthogrid and Honeycomb lattices are not a viable option to be integrated into turbine blades.

3.4 Design Two - Gyroid, Simplified Arch

The Design team presented the Structures team with lattice designs of the second iteration of the design process: the Gyroid and Simplified Arch lattices. Improved for structural-mechanical isotropy and enhanced airflow, the provided lattice designs were analyzed by the Structures team for their potential use for the project's goal. The Gyroid structure was considered to be a good match for the application, except for the production, and manufacturing aspect. The Structures team based this judgment on the background research and literature review steps of the initial analysis, which showed the significant challenges in CAD model production, 3D printing, and testing of the structure. Due to the inherent complexity of the model, it would not be possible to be manufactured using the available lab methods of SLA 3D printing, or the theoretical proposed EBM and SLM additive manufacturing methods. The consideration of the Gyroid lattice structure for the project's goal was terminated due to its lack of practicality. The second lattice structure design of the second design process iteration that was presented to the Structural team was the Simplified Arch lattice design. The unit cell of that design consisted of three perpendicularly oriented struts, which were analyzed by the Structures team utilizing basic concepts and fundamentals of structural analysis. The Simplified Arch lattice design was found to have a large weak spot in the point of interaction of all the struts, which would concentrate all of the stress on the center of each unit cell and the point of stress concentration would be the ultimate failure point of the lattice structure. Two individual unit cells were 3D-printed by the Structures team, mainly to test the printing device and software, but also to investigate. The Structures team determined that we would not continue the analysis with any of the lattice structures of the second iteration of the design process conducted by the Design team.

3.5 Design Three - Traditional Arch

The third and final iteration of the lattice structure design process produced the Traditional Arch lattice with arched struts instead of straight ones. The third design was found to potentially have good airflow, be easily manufacturable, and have no obvious weak spots. The unit cells are composed of curved struts, allowing for a better distribution of the load on the structure. It was thoroughly analyzed by the Structures team and chosen to be used in the experimental part of the project conducted in the laboratory. Multiple samples of the Traditional Arch lattice were 3D-printed in two different orientations. For three-point bending tests the Structures team decided to produce two types of samples consisting of rectangular prisms with a skin of set thickness of similar dimensions of that of turbine blades, filled in with the Traditional Arch lattice at two orientations perpendicular to each other for each type. To accurately validate the results from the FEM analysis, the team produced samples to be used for tension and compression testing, consisting purely of the Traditional Arch lattices arranged into the same shape as the rectangular prism from the previous instance. As expected, the Traditional Arch lattice structures did not perform as well in the three-point bending tests in comparison to the Honeycomb lattice structure due to its three-dimensional design. All of the Arch lattice samples tested with the three-point bending method fractured and were torn apart with only two large pieces able to be identified. The data collected from the bending tests of the two orientations of the Traditional Arch lattice structure was reviewed and decided on by the Structures team as sufficient for the FEM validation.

3.6 ABAQUS (Version 2019) Simulations and Modelling

3.6.1 Three-Point Bending Test Simulation Geometries: Instron 5944 Fixture and Honeycomb Rectangular Prism

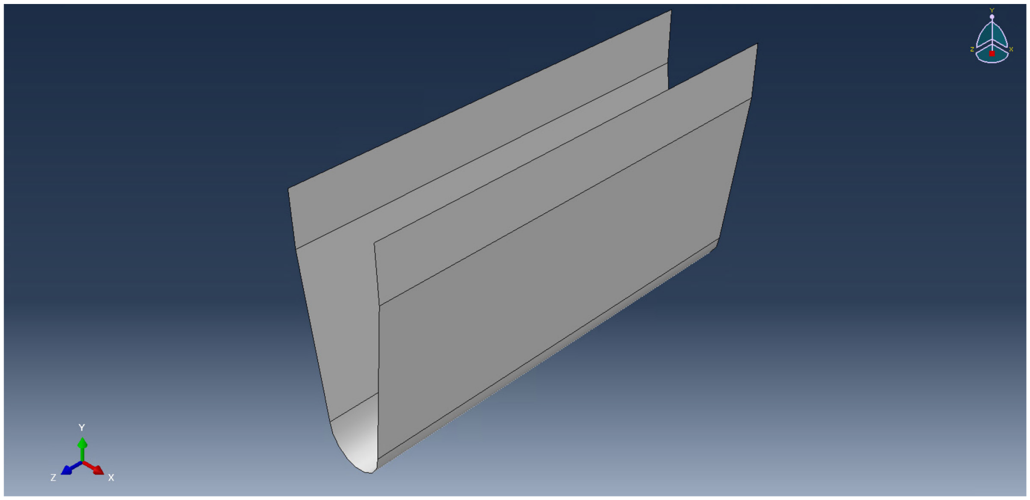

Figure 44: ABAQUS Model of the Instron 5944's Primary Bending Fixture

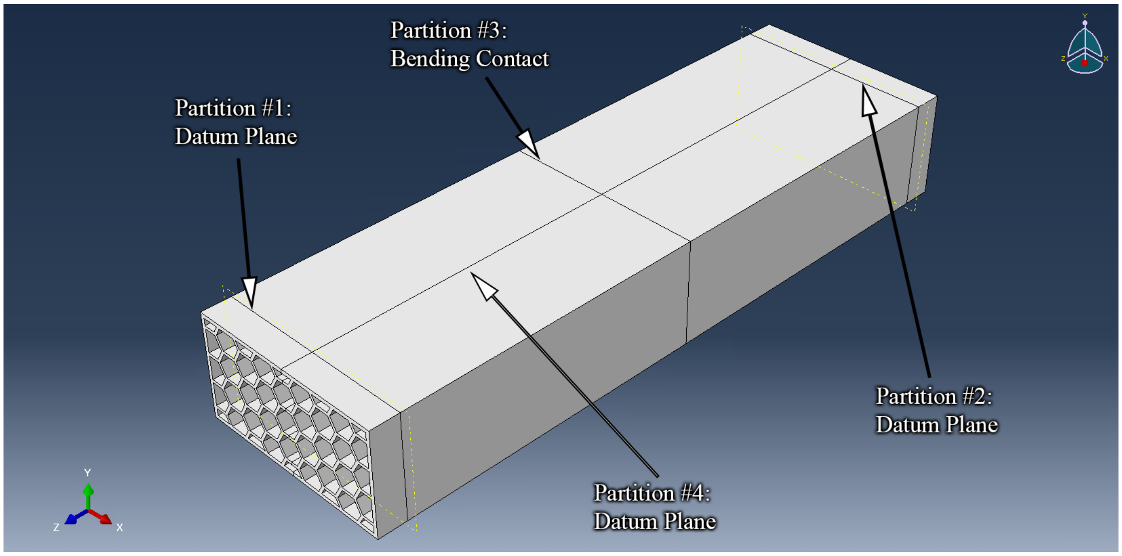

Figure 45: ABAQUS Model of Honeycomb Rectangular Prism

To replicate the testing conditions of the three-point bending test, conducted on the Instron 5944, a custom fixture geometry to match the Instron's three-point bending fixtures was developed within ABAQUS. In Figure 44, the fixture is seen in the XYZ coordinate system view.

Then, the Honeycomb Rectangular Prism geometry was imported into ABAQUS. Since this geometry has well-defined angles, it was simple to import into ABAQUS as an 'iges' file from its 'stl' form in AutoCAD.

In Figure 45, the Honeycomb Rectangular prism can be observed. Four partitions were made in the geometry. These acted as datum planes where boundary conditions were applied to ensure the simulation would perform like a proper three-point bending test.

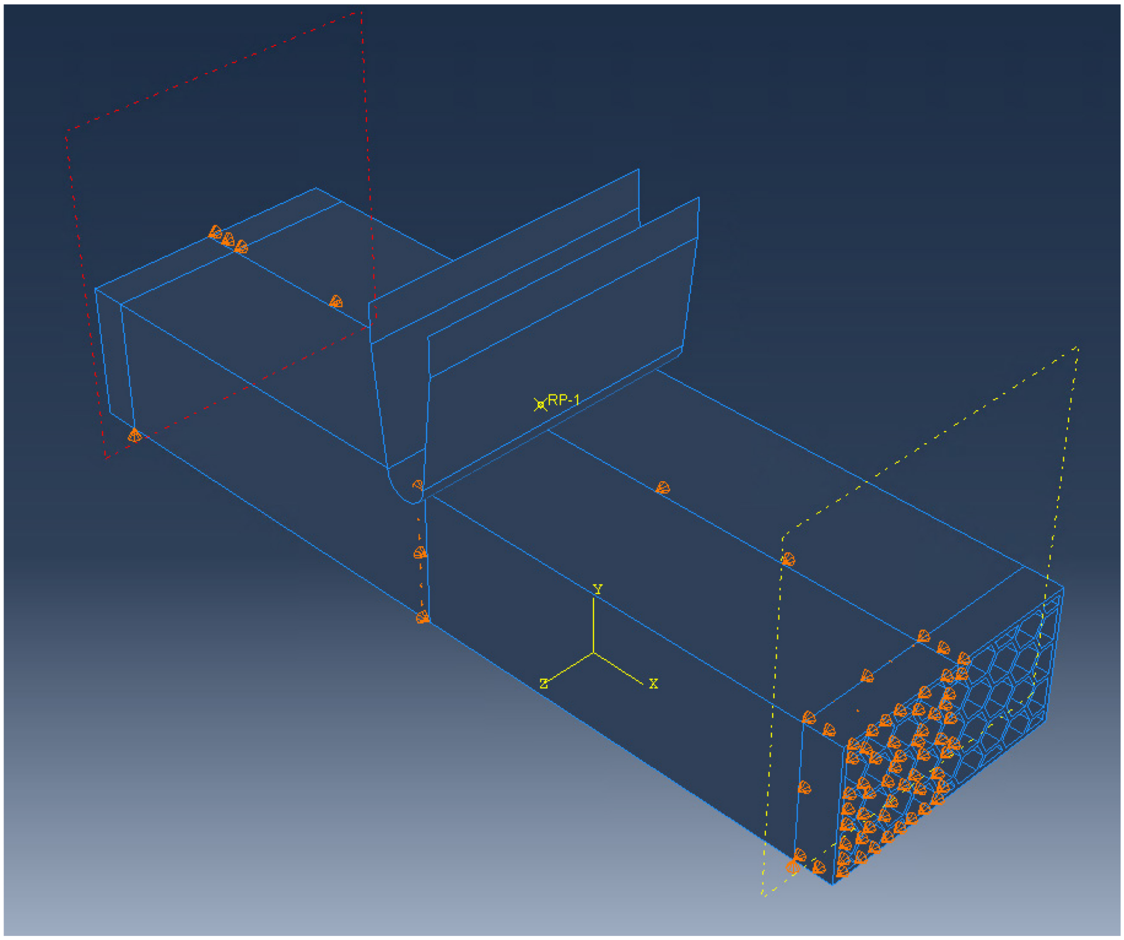

Figure 46: Boundary Conditions of Honeycomb Rectangular Prism

Specifically, the Honeycomb geometry was pinned at datum planes #1 and #2. Therefore, when the primary bending fixture contacted the geometry, these two datum planes would enable the prism to rotate at those points, while the midpoint of the geometry translated down in the -Y direction.

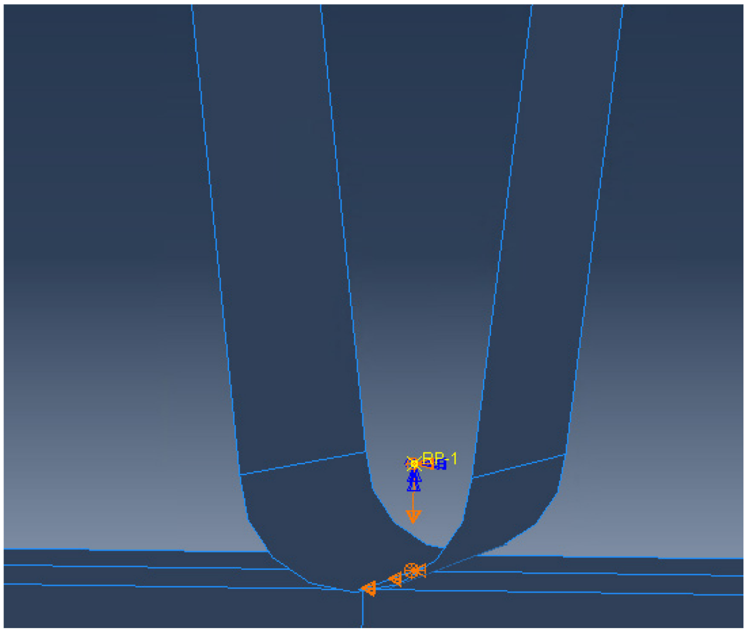

Figure 47: Loading Conditions for Three-Point Bending of Honeycomb Rectangular Prism

To apply a load to the Honeycomb geometry, the primary bending fixture was given a reference point at the midpoint of its bottom radius, as seen in Figure 47. The load was applied in the -Y direction.

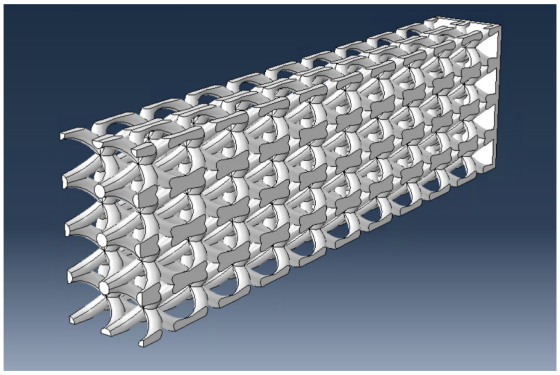

Figure 48: ABAQUS Model of No-Wall Arch Rectangular Prism

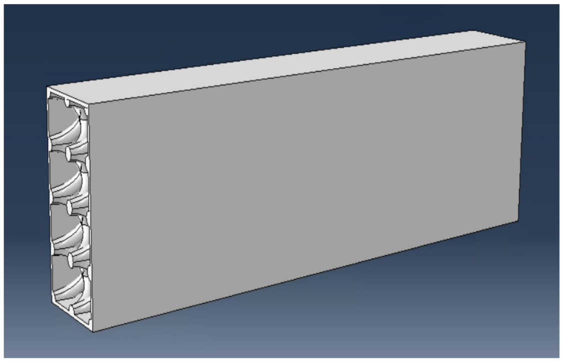

Figure 49: ABAQUS Model of Walled Arch Rectangular Prism

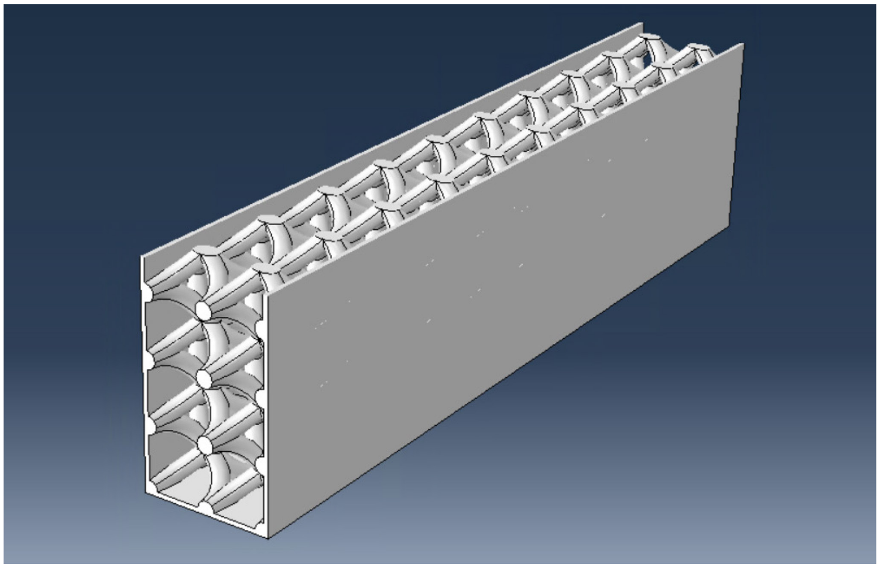

Figure 50: ABAQUS Model of Arch Rectangular Prism with Three Walls

As the bending simulations progressed, different geometries were experimented with to further understand ABAQUS and the limitations of what geometries could be imported into the program. Figures 48-50 are examples of three Arch-based prisms that ABAQUS could not import properly. The reason why these geometries failed was hypothesized to be the complex intersections of Arch unit cells in contact with each other. Nevertheless, a workaround was found for these geometry intricacies.

3.6.2 Tensile and Compression Simulation: Traditional No-Wall Arch

A breakthrough was made while experimenting with different imported Arch geometries in ABAQUS. Initially, the Structures Team attempted to use the Arch geometry in Figure 48 for the tensile and compression simulations. Yet, ABAQUS would always import this geometry with discontinuities. Figures 51 and 52 demonstrate these discontinuities.

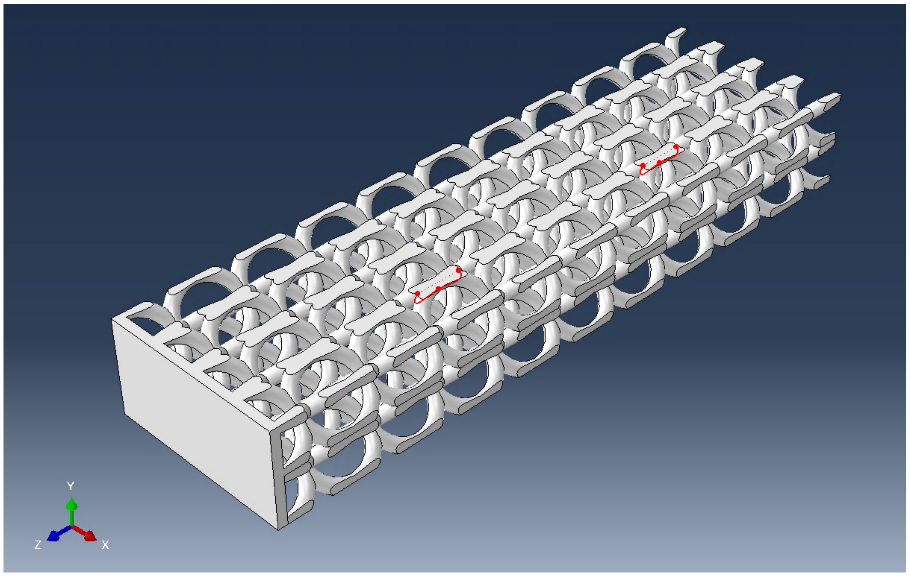

Figure 51: Inadequate Geometry Imported for Tensile and Compressive Simulations

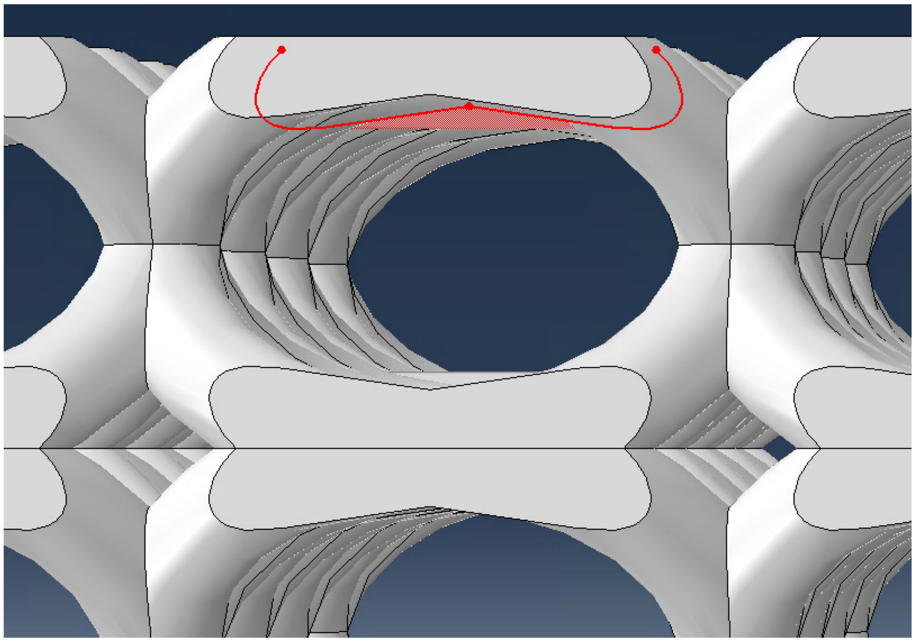

Figure 52: Improper Face Generation in Original Geometry for Tensile and Compression Simulations

The reason that these improper face geometries were generated is unknown but there are various geometry repair tools in ABAQUS that can repair these errors. Specifically, the "repair face" tool in the geometry edit menus was sufficient for resolving these improper geometries. The Structures Team then transitioned to developing the load qualities and boundary conditions used in the tensile and compression simulations.

Nevertheless, once the simulation was prepared to mesh the assembly and run the tensile simulation, more errors were encountered. Although the inadequate geometry has been fixed, ABAQUS was unable to mesh the final assembly. There were thousands of elements in the final mesh, and the Structures team was presented with two alternatives: either the mesh would have to be manually repaired using ABAQUS' geometry repair tools, or the initial geometry being used for the simulations would have to be redesigned. The latter option was chosen, and the Structures Team had to explore alternative methods for creating the same geometry featured in Figure 51.

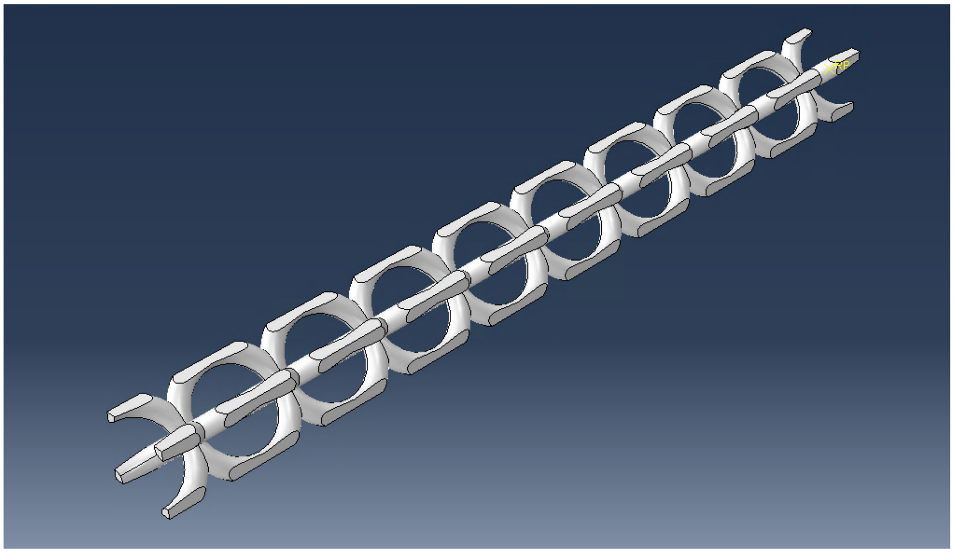

Figure 53:Column of Nine Arch Lattice Unit Cells

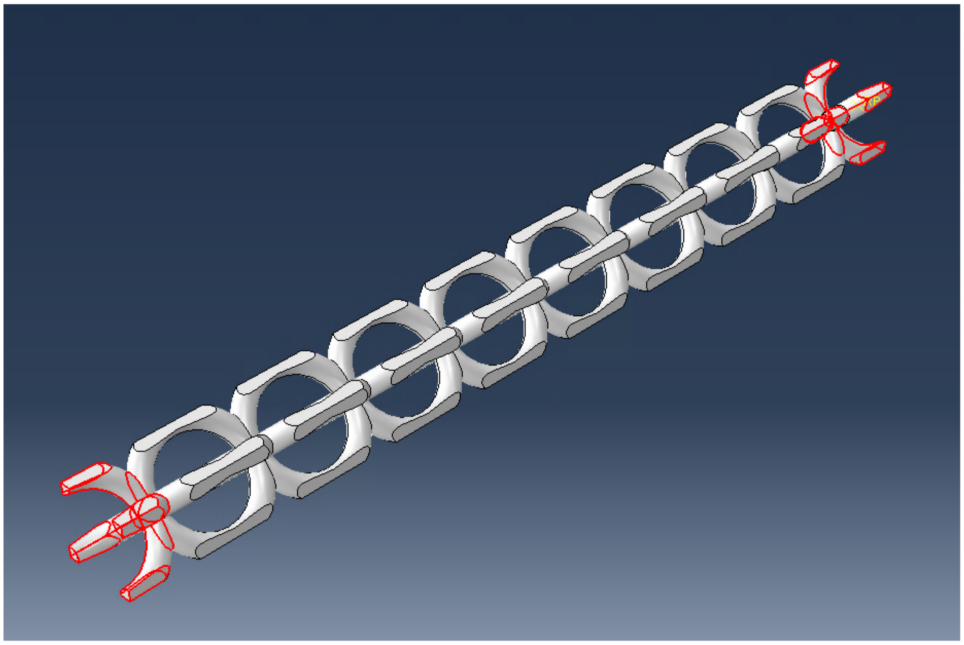

Figure 54: Partitioned Arch Column Geometry

To execute this design process, the Structures Team had to recognize which characteristics of the initial geometry, in Figure 51, resulted in ABAQUS' meshing process to error consistently.

Importing a single Traditional Arch unit cell into ABAQUS provided important insight on how ABAQUS interpreted all other Arch geometries. For instance, in Figure 51, this geometry had both rows and columns of Traditional Arch unit cells, which ABAQUS then had to interpret as one part. Beyond the interpretation that ABAQUS had on this geometry, the Structures Team knew that it was the same Traditional Arch unit cell repeated and combined into a prism, yet ABAQUS could not know this.

Figures 53 and 54 demonstrate the geometry that resolved these meshing complications. Instead of importing the final arch prism geometry into ABAQUS, a column of Traditional Arch unit cells was imported instead. The advantages of this model were that ABAQUS could interpret the geometry as a stack of Traditional Arch unit cells.

Furthermore, in regards to the geometries featured in Figures 53 and 54, ABAQUS did not have to interpret the rows of Arch unit cells. The intersection of Traditional Arch unit cells, when combined in a row orientation, resulted in discontinuities while being imported into ABAQUS.

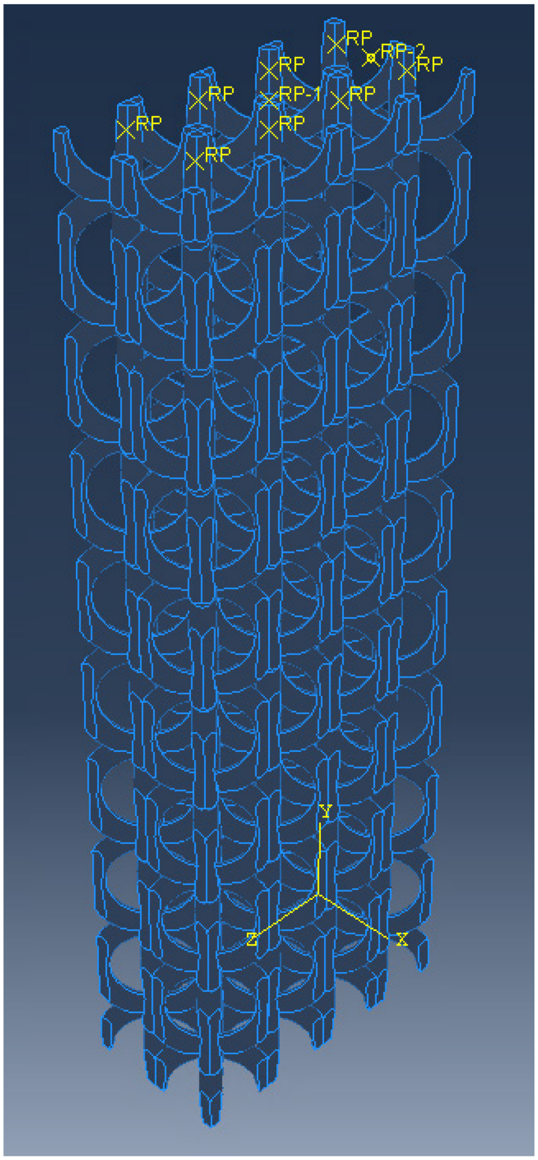

Figure 55: Assembly of Arch Unit Cells for Tensile and Compression Simulations

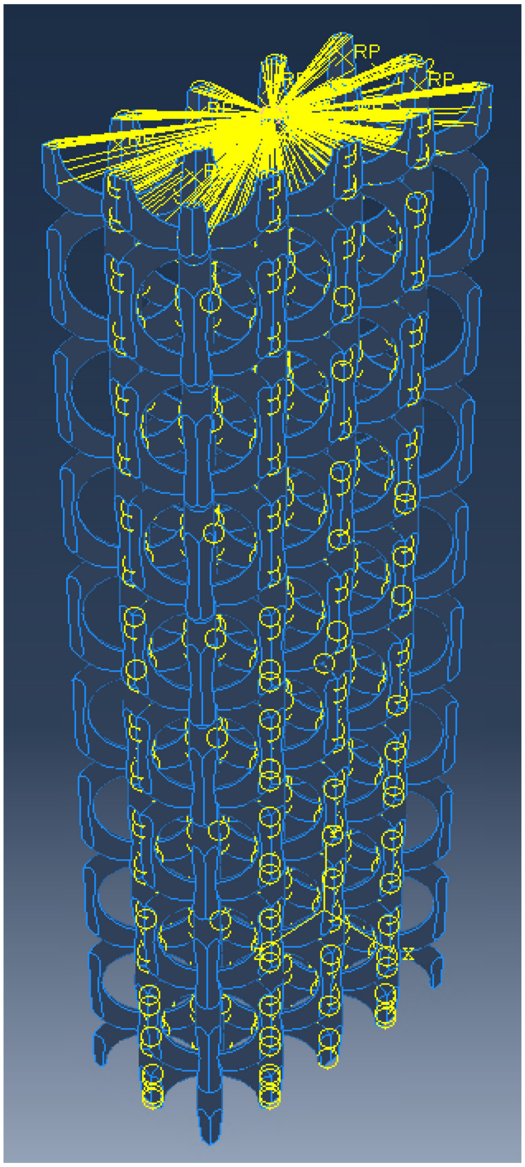

Figure 56: Coupling and Tie Interactions

By importing the Arch column geometry in its standalone form, the Structures team was then able to assemble eight columns into the Arch rectangular prism in Figure 55. The Arch rectangular prism geometry was now stable and sufficient for ABAQUS to interpret for tensile and compression simulations.

To prepare the Arch prism for tensile and compression simulations, the surface-to-surface interaction between columns had to be defined, as well as the coupling properties required for the tensile/compressive forces to be applied evenly throughout the Arch prism geometry.

The coupling interaction between all the Arch columns allowed for the tensile and compressive loads to be applied evenly throughout the Arch prism geometry and can be seen in Figure 56, denoted by the yellow lines at the top of the Arch prism geometry.

Tie interactions were defined for all surface-to-surface interactions between the eight columns of the Arch prism, as seen in figures 56, 57, and 58, and were denoted in ABAQUS by the yellow, red and purple circles. These tie interactions defined that there would be no relative movement between column surfaces, effectively fusing the columns in the simulation.

The purple and red circles featured in Figure 58 denote the master-follower relationship that ABAQUS requires for tie interactions. These relationships were arbitrary and as long as one column surface was the master and the corresponding surface was the follower, the tie interaction would behave correctly.

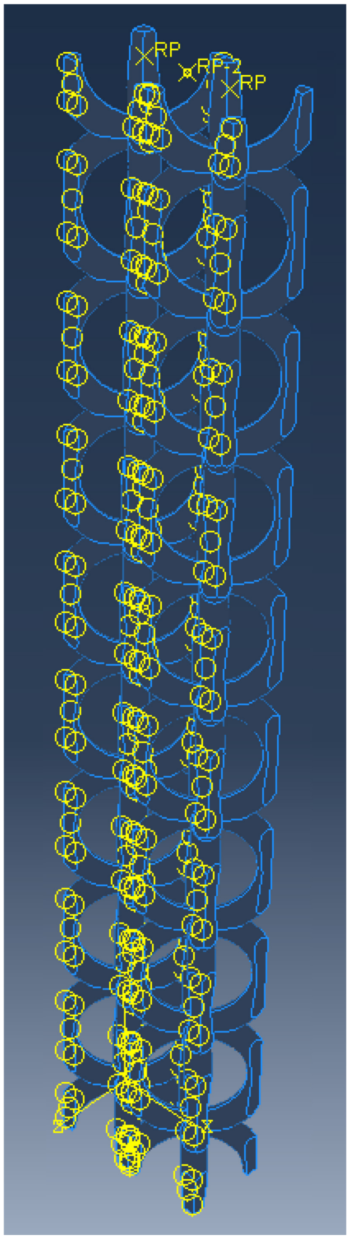

Figure 57: Tie Interactions for Surface-to-Surface Contact in between Column Sets

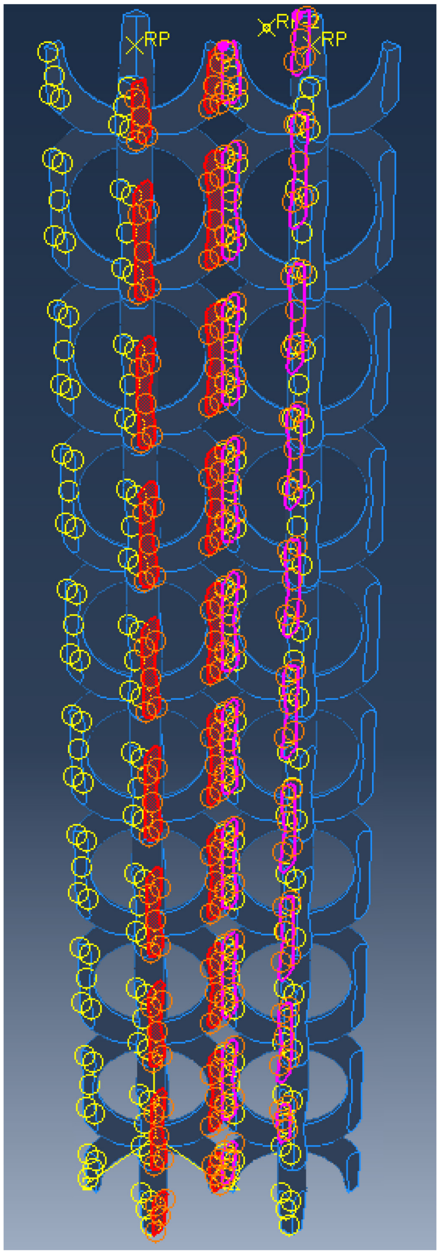

Figure 58: Master-Follower Tie Interactions in between Individual Columns

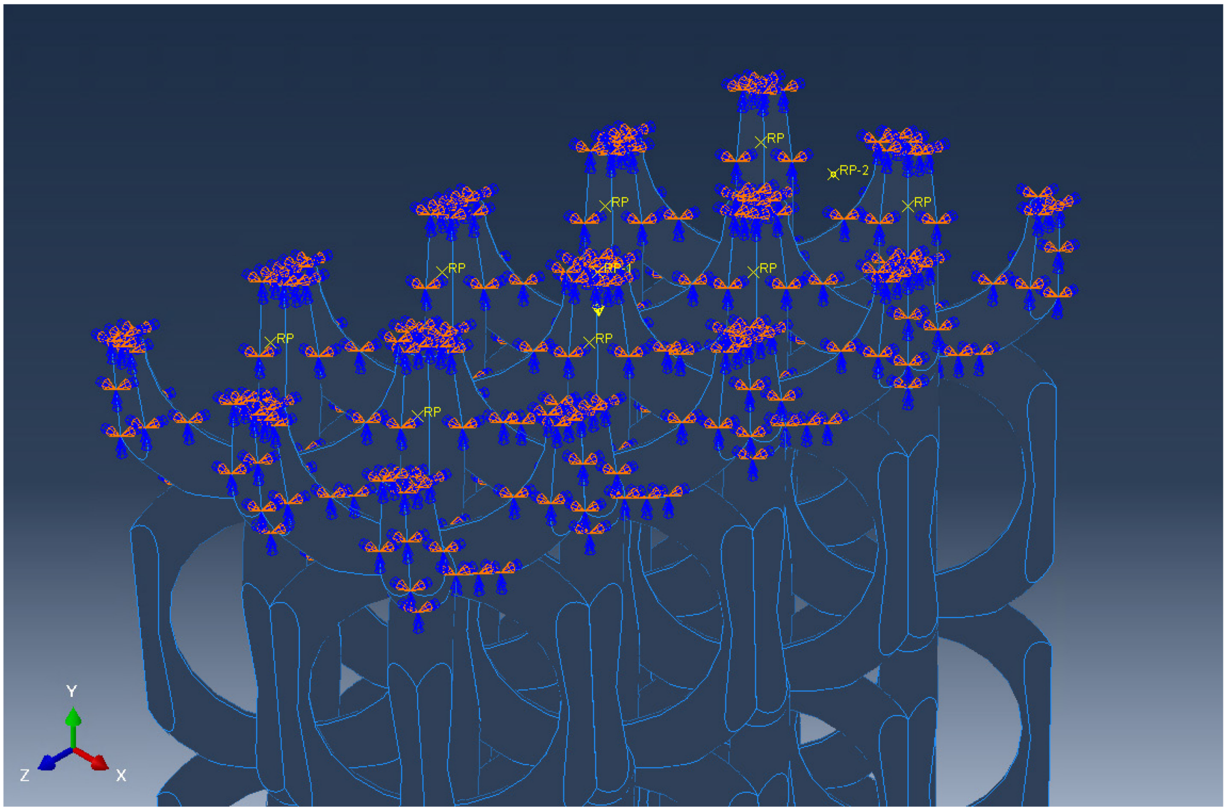

Figure 59: The Displacement Boundary Condition Applied for Tensile and Compressive Simulations

ABAQUS' boundary conditions and load properties were the final requirements to run the compression and tensile simulations. To replicate the tensile and compression testing conducted in the lab, the top of the Arch prism was allowed to translate only in the Y-direction. In Figure 59, this displacement boundary condition is denoted by the blue and orange arrows, and the coordinate system is featured in the lower-left section of this figure.

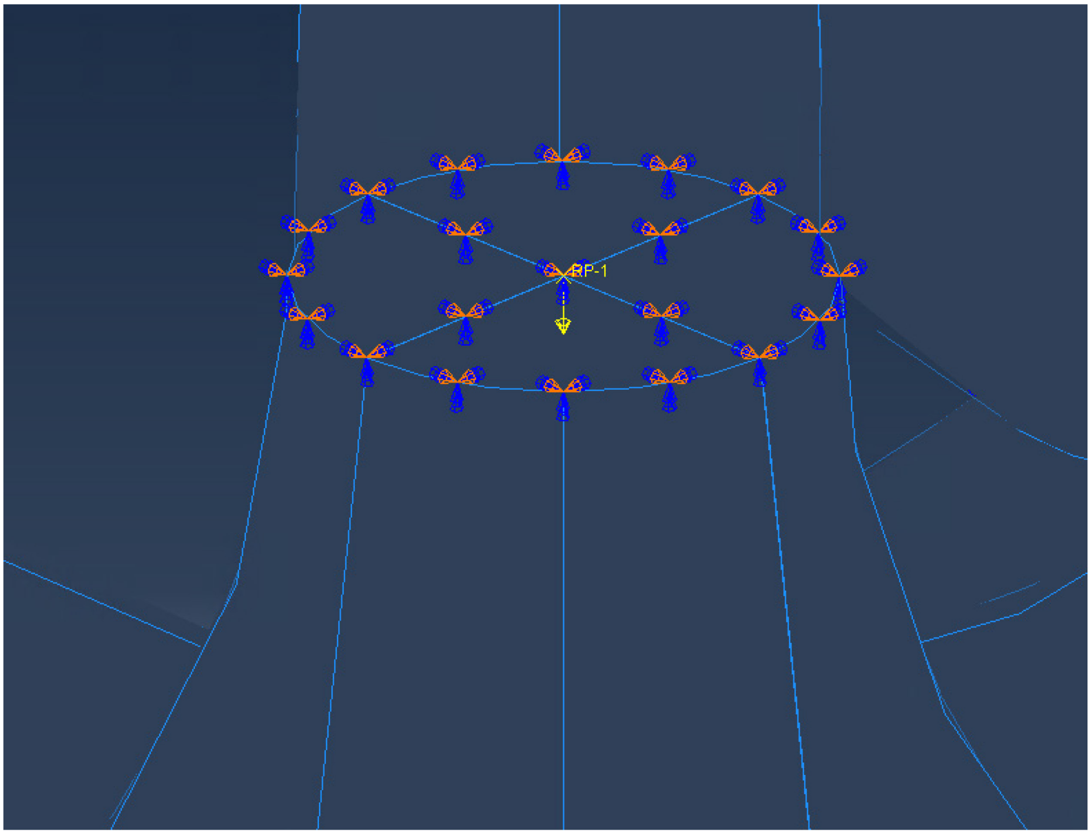

Figure 60: Compressive Load Vector

Furthermore, the yellow load vectors featured in Figures 60 and 61 depict the tensile and compressive loads required to simulate the testing conditions applied in the lab. Both the tensile and compressive loads had a magnitude of 1.6 kN and were applied in a ramp function just as the loads were applied in lab testing.

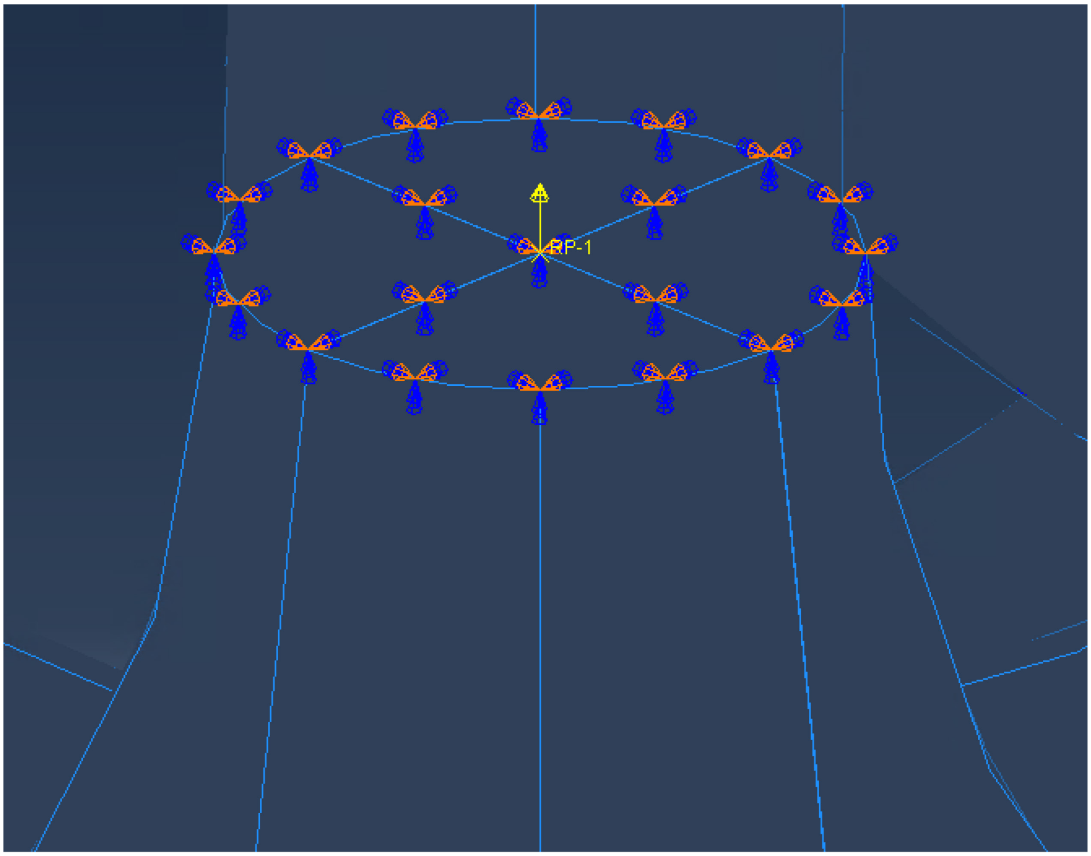

Figure 61: Tensile Load Vector

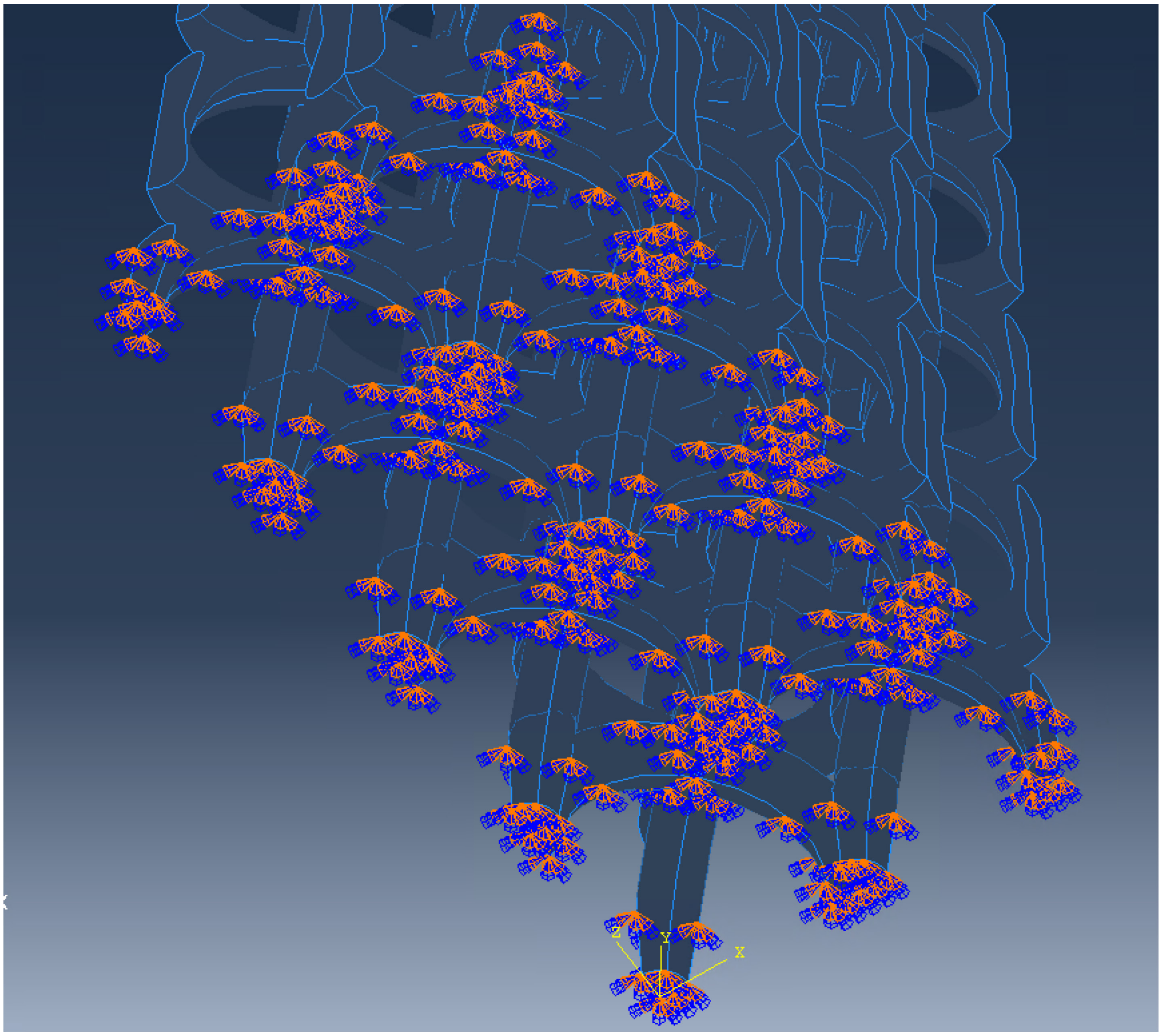

Figure 62: The Encastre Boundary Condition Applied for Tensile and Compression Simulations

ABAQUS' encastre boundary condition was applied to the base of the Arch prism model, depicted in Figure 62 by the blue and orange arrows. The encastre condition fixed the base of the structure at its initial position in the X, Y, and Z axes throughout the test. Encastre boundary conditions also restrict the rotation of the structure at the position in which it is applied.

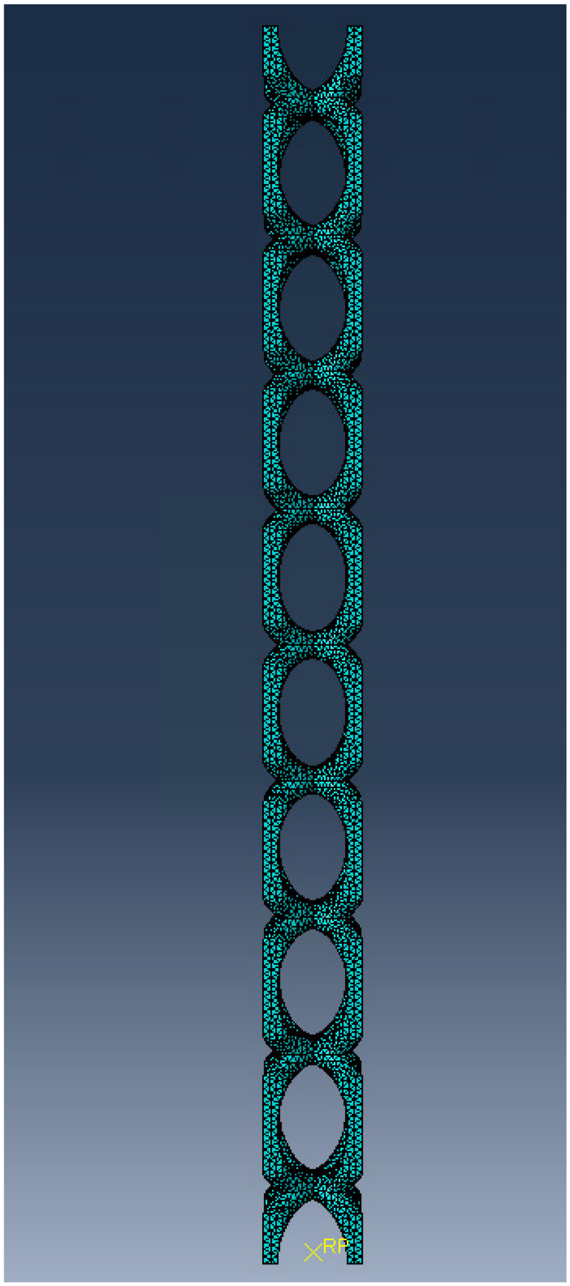

Figure 63: Individual Arch Column Mesh Using Tet Elements

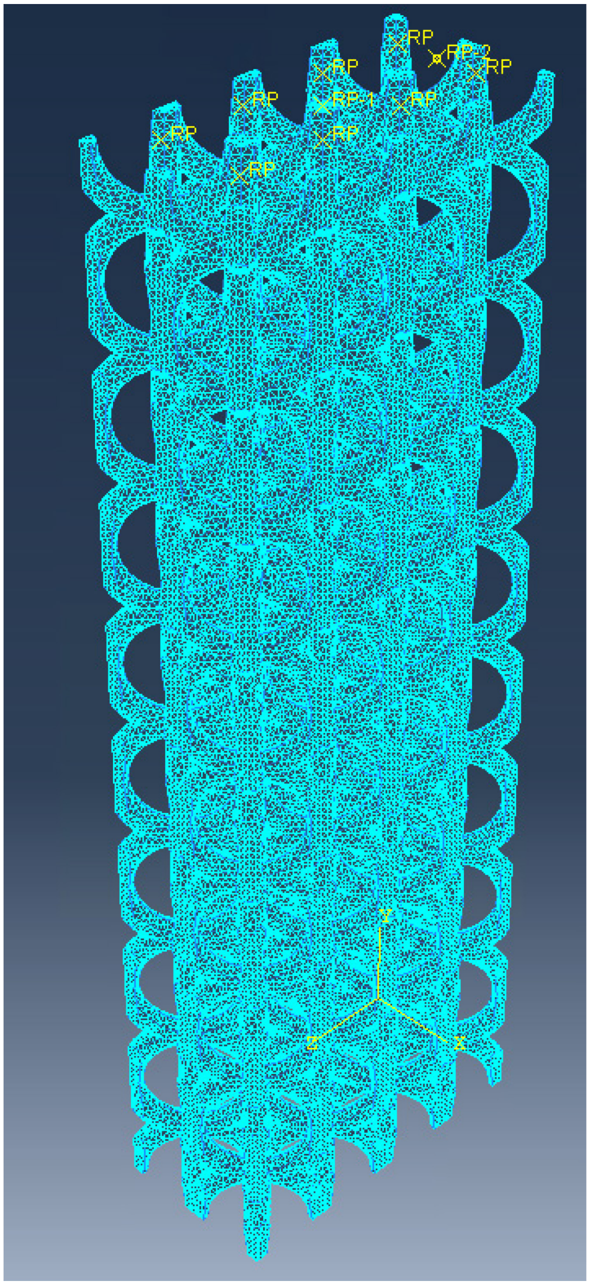

Figure 64: Entire Assembly Mesh for Tensile and Compression Simulations

Another advantage of the Arch column geometry was that it improved the final mesh of the Arch prism geometry. Figure 63 features the Arch column mesh in its standalone form. Then, by combining eight of these columns into the prism geometry form, as seen in Figure 64, ABAQUS only had to mesh the initial Arch column geometry; eliminating any errors previously encountered in the meshing stage.

3.7 Results

3.7.1 ABAQUS Simulation Results:

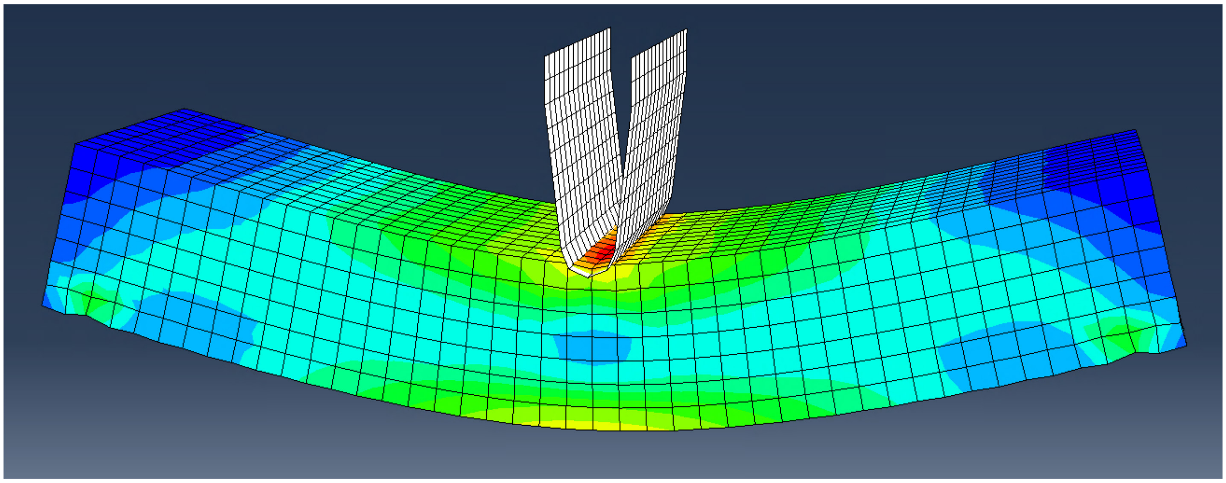

Figure 65: ABAQUS Honeycomb Rectangular Prism Three-Point Bend Test Results: Mises Stress Color Map

To visualize the stresses the Honeycomb Rectangular Prism encountered during the three-point bending simulation, a Mises stress color map was generated in ABAQUS. The Structures Team was aware that the Honeycomb Rectangular prism would not fracture during the three-point bending test, therefore the Mises stress values were not important for the results in this section. Although, the Mises color map did enhance the Structures Team's understanding of the stress concentrations during the three-point bending test.

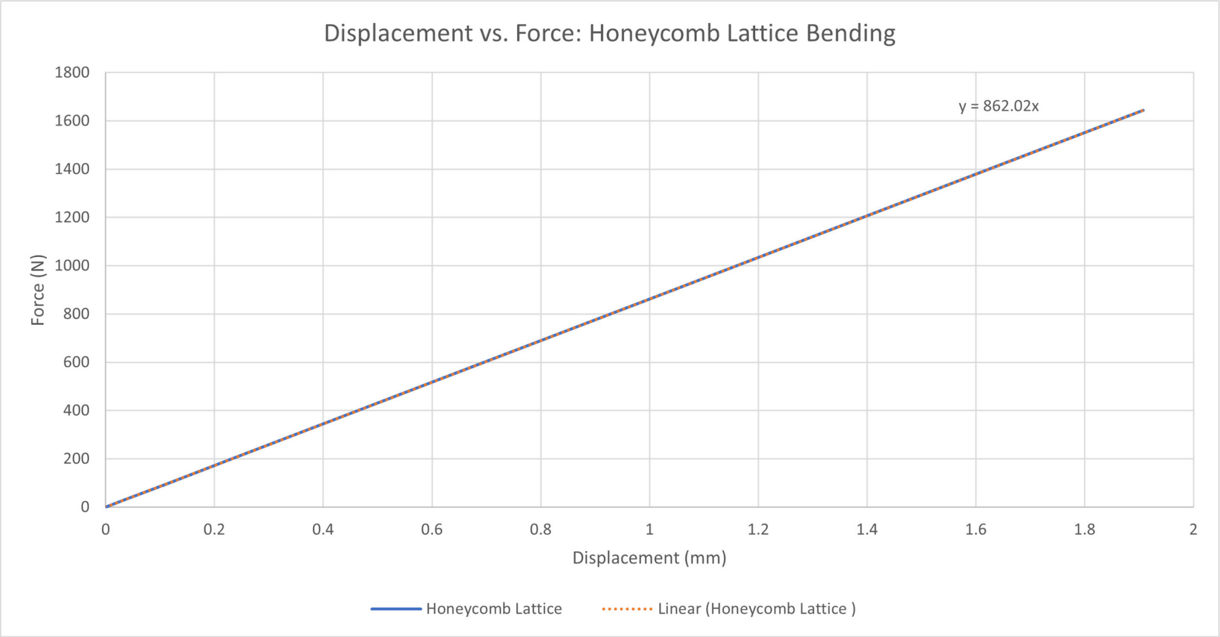

Figure 66: ABAQUS Honeycomb Rectangular Prism Force vs. Displacement Results

Figure 66 features the displacement experienced by the Honeycomb Rectangular Prism during the three-point bending simulation. In Figure 66, the displacement results, for the midpoint of the Honeycomb Rectangular prism, do agree with the lab testing displacements recorded for the Honeycomb Rectangular Prism. The agreement of these displacement results demonstrates that the Honeycomb Rectangular Prism ABAQUS model can be used for more complex simulations, such as dynamical loading scenarios or other static loading simulations.

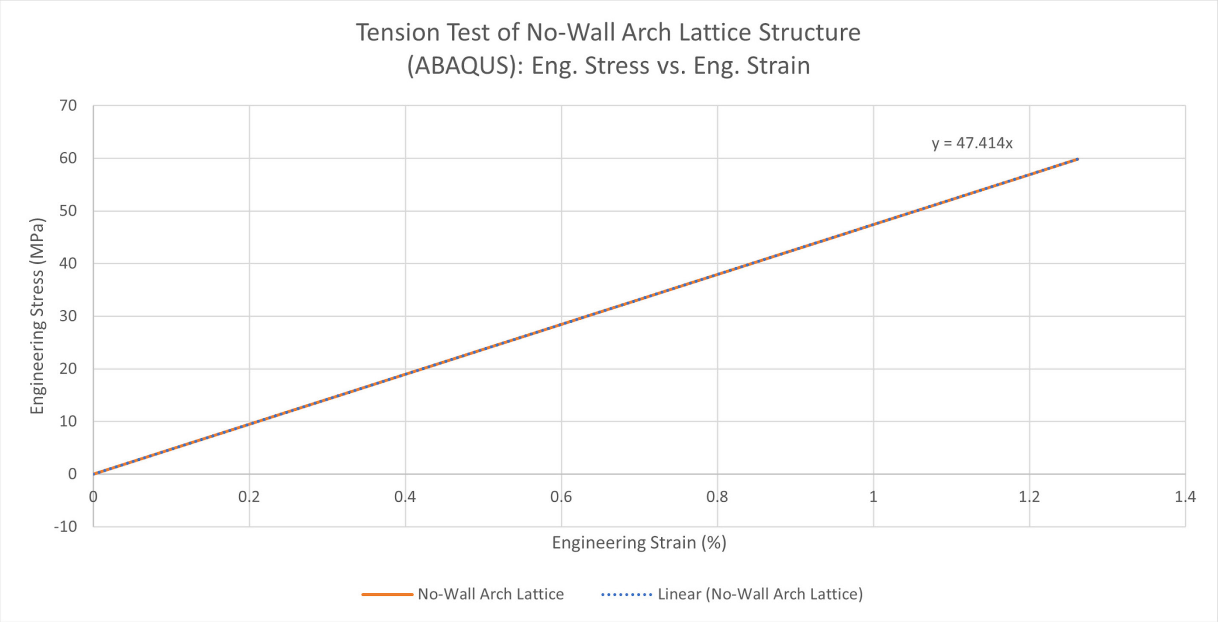

Figure 67: ABAQUS No-Walls Traditional Arch Rectangular Prism Tensile Eng. Stress vs. Eng. Strain

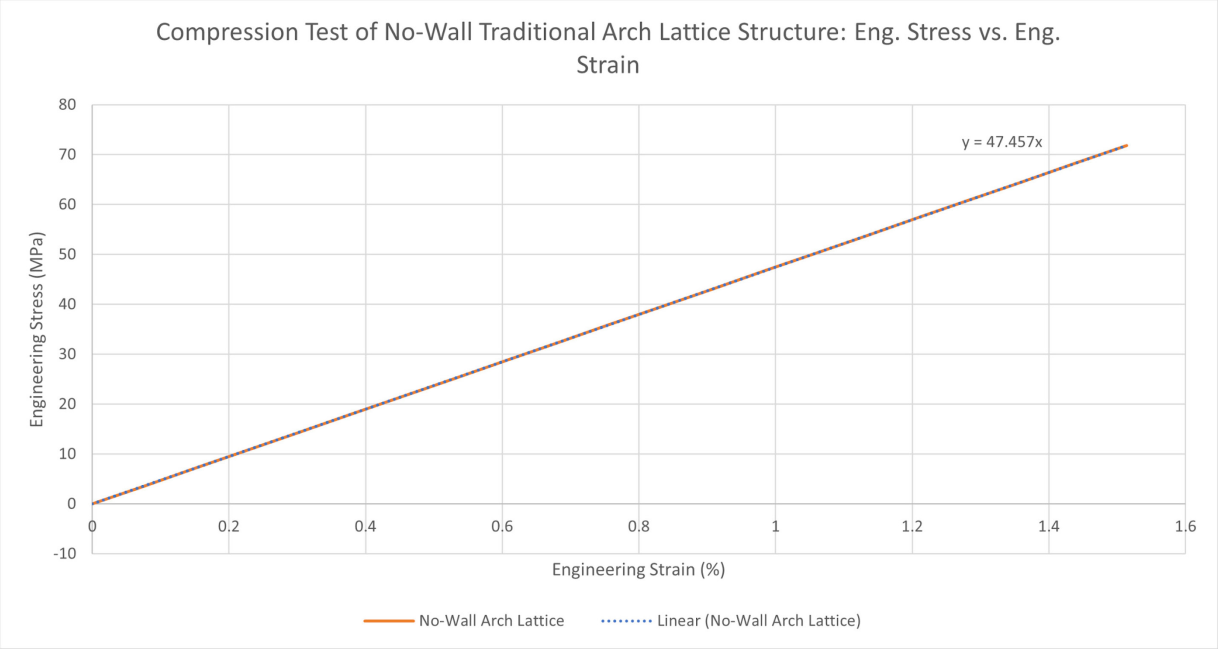

Figure 68: ABAQUS No-Walls Traditional Arch Rectangular Prism Compression Eng. Stress vs. Eng. Strain

Figures 67 and 68 present the graphs of engineering stress vs. engineering strain for tension and compression test received through the numerical analysis. The results are consistent with each other, providing a Young's modulus of 4.74 GPa. The maximum stress experienced by the No-Wall Arch Lattice prism in the tensile and compression testing procedures was around 60 and 70 MPa accordingly. The straight lines in the two plots suggest that the samples undergo elastic deformation and would return to their initial shape.

Two three-point bending tests in the Instron with each lattice structure design were conducted. For the first experiment, the test-end force was set at 1.6 kN, which was enough to fracture the Traditional Arch lattice structure but was insufficient to fracture the Honeycomb lattice structure. Shown in Figures 69 and 70 are the Honeycomb and Traditional Arch lattice structures in the three-point bending fixture respectively, where each figure shows the points of max and minimum deformation.

The second experiment was conducted with the test-end force set at 1.8 kN, which was also insufficient to fracture the Honeycomb lattice rectangular prism sample and insufficient to even permanently deform it. Displayed in Figure 69 is the Honeycomb lattice structure at the instant of max deformation. During the second experiment, the testing setup was able to capture the Traditional Arch sample fracture instant of the trial.

3.7.2 Structures Team Experimental Results

The visual comparison of the three-point bending test conducted experimentally and numerically does not match exactly. As seen in Figures 65 and 69, the Honeycomb Lattice model in the numerical simulation undergoes a far greater deformation of the 3D printed sample that was tested in the lab. The difference in results is most likely caused by the inaccurate value for Young's modulus of the 3D printer resin provided by the manufacturer. The Traditional Arch Lattice prism deformation as can be seen in Figure 70 was greater than that of the Honeycomb lattice in Figure 69, which was an expected result due to the nature of the Honeycomb lattice.

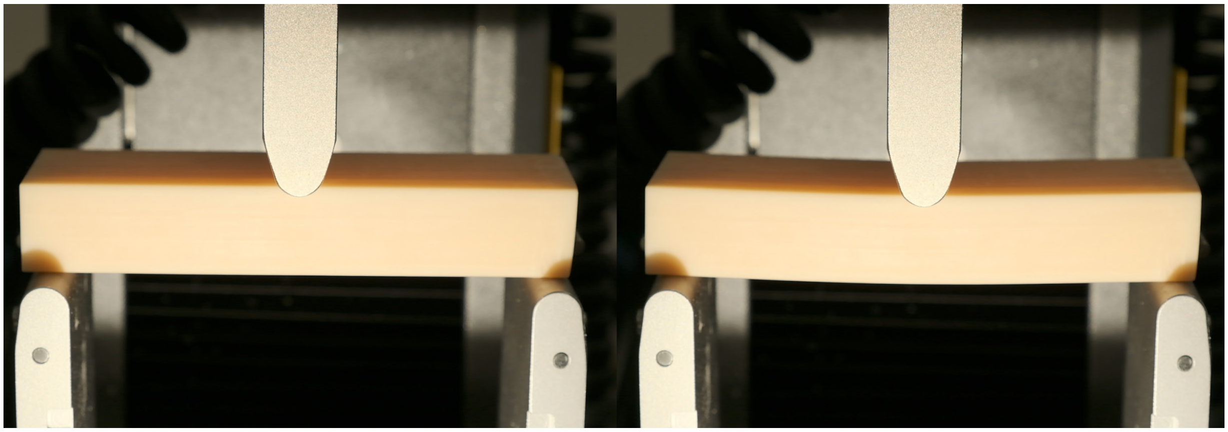

Figure 69: Honeycomb Lattice Structure Three-Point Bend Test at Initial and Maximum Deformation

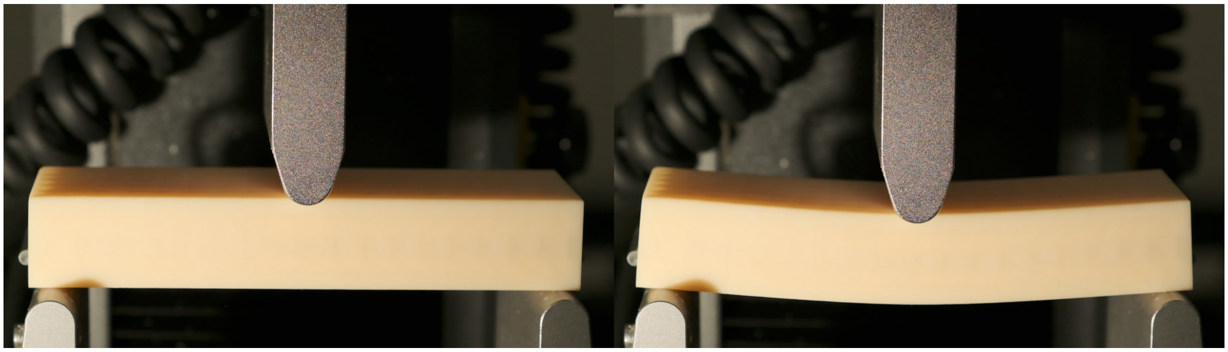

Figures 70: Traditional Arch Lattice Structure Three-Point Bend Test at Initial and Maximum Deformation

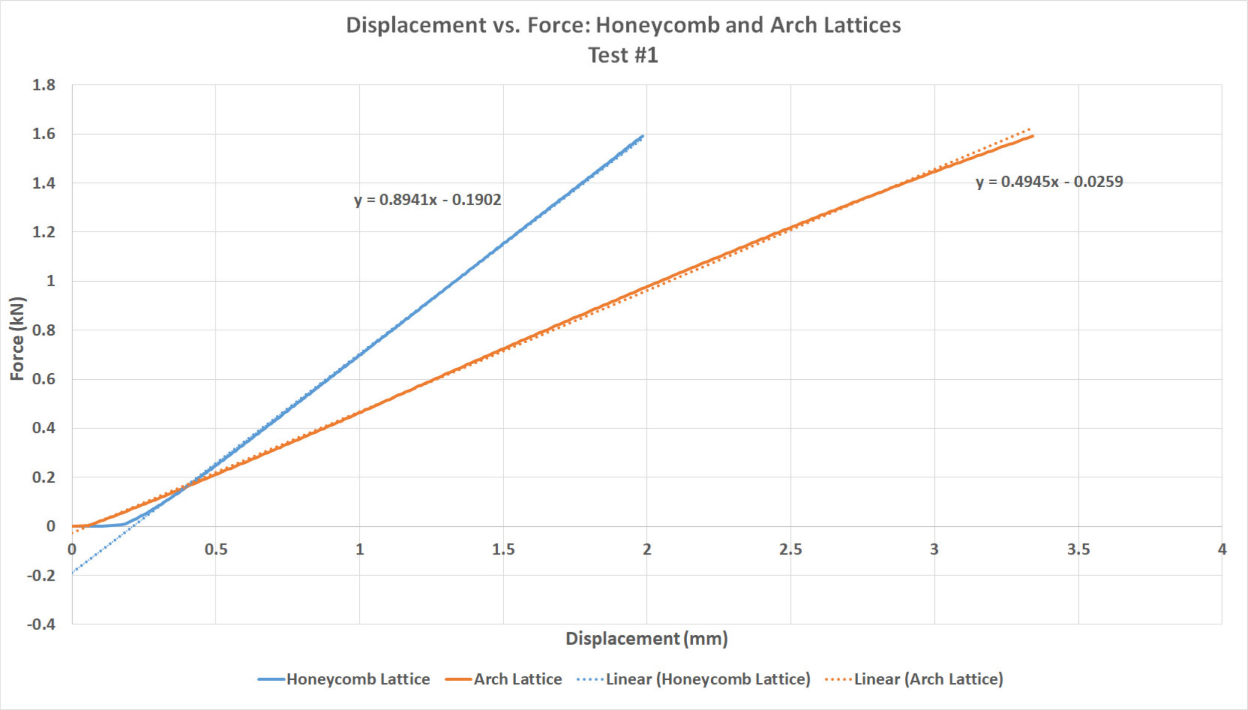

Figure 71: 1st Bending Test of Honeycomb and Arch Lattices Results Graph (Force vs. Displacement)

In Figure 71, the Honeycomb lattice structure was able to absorb approximately 1.57 J of energy, withstanding a concentrated force on the cross-section mid-length of the rectangular prism of 1.59 kN. The mid-length cross-section was recorded to deflect 1.98 mm. The minimum normal stress experienced on the upper surface of the Honeycomb sample was -1.74 Pa. Figure 50 shows the maximum values for the Traditional Arch rectangular prism sample: maximum energy absorbed before fracture 2.70 J, maximum force 1.59 kN, maximum displacement at mid-length of the rectangular prism was 3.40 mm. The minimum stress experienced on the upper surface of the Traditional Arch sample was recorded as -0.726 Pa.

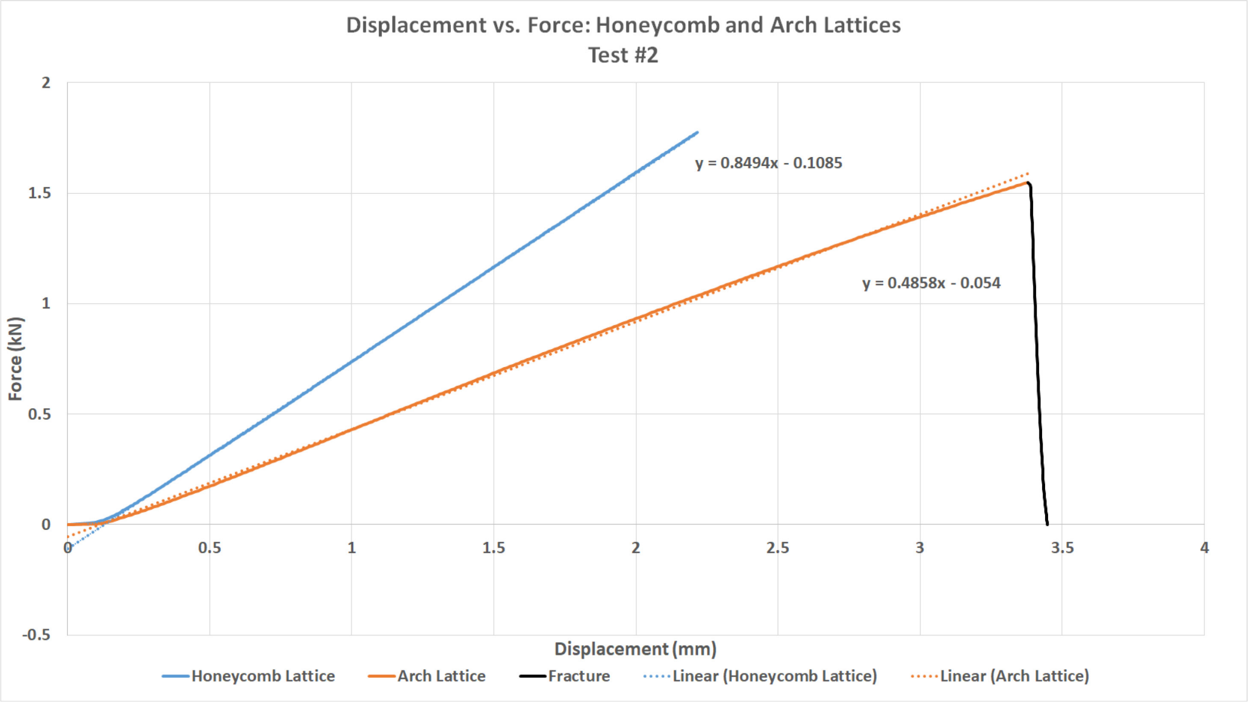

Figure 72: 2nd Bending Test of Honeycomb and Arch Lattices Results Graph with Fracture Displayed (Force vs. Displacement)

As seen in Figure 72, the second experiment yielded results of similar nature. The Honeycomb lattice structure was able to absorb approximately 1.97 J of energy, withstanding a concentrated force on the cross-section mid-length of the rectangular prism of 1.77 kN. The mid-length cross-section was recorded to deflect 2.21 mm. The minimum normal stress experienced on the upper surface of the Honeycomb sample was -1.94 Pa. Figure 73 shows the maximum values for the Traditional Arch rectangular prism sample: maximum energy absorbed before fracture 2.61 J, maximum force 1.55 kN, maximum displacement at mid-length of the rectangular prism before fracture was 3.38 mm. The minimum stress experienced on the upper surface of the Traditional Arch sample was recorded as -0.707 Pa.

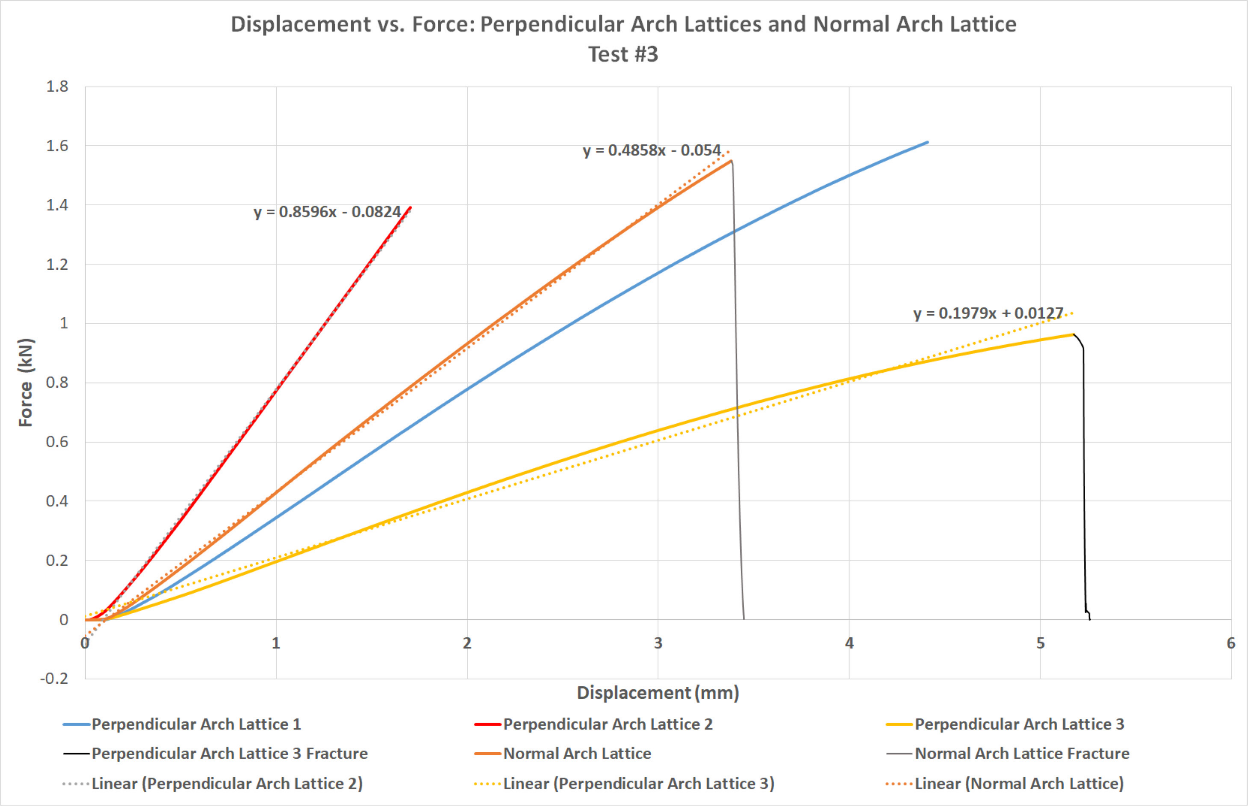

Figure 73: 3rd Bending Test of 3 Perpendicular Arch Lattices Results Graph with Fracture Displayed and Results for Normal Arch Lattice from Test #2 (Force vs. Displacement)

For the third experiment, testing proceeded with three-point bending trials on the Traditional Arch lattice rectangular prism structures with unit cells aligned perpendicularly to the height of the prism., i.e. in the longitudinal orientation. After two of the three samples were tested, significant inconsistency was discovered in the samples' performance and trials proceeded to repeat the test on a third sample to prove the inconsistency. To better understand and visualize the difference in performance based on the orientation of the unit cells, the results of the third experiment were graphed on one plot with results of the normally oriented Arch lattice from test #2. On average, the Traditional Arch lattice structure with perpendicularly oriented unit cells appears to perform very similarly to that with normal unit cell orientation lattice structure, although the performance is very unpredictable.

Table 2: 3rd Bending Test Results of 3 Perpendicular Arch Lattices from Test #3 and Normal Arch Lattice from Test #2

Parameter	**Perp. Arch Lattice 1**	**Perp. Arch Lattice 2**	**Perp. Arch Lattice 3**	**Avg. Value**	**Norm. Arch Lattice**
Energy	3.56 J	1.18 J	2.49 J	**2.41 J**	2.61 J
Max. Force	1.61 kN	1.39 kN	0.963 kN	**1.32 kN**	1.55 kN
Max. Displ.	4.41 mm	1.70 mm	5.17 mm	**3.76 mm**	3.38 mm
Min Stress	-0.229 Pa	-0.197 Pa	-0.137 Pa	**-0.188 Pa**	-0.707 Pa

As can be seen in Table 2, all of the parameters are similar except for the minimum normal stress experienced by the structures. This is due to the significantly larger second moment of inertia of the cross-section of the Arch lattice structure with perpendicularly oriented unit cells.

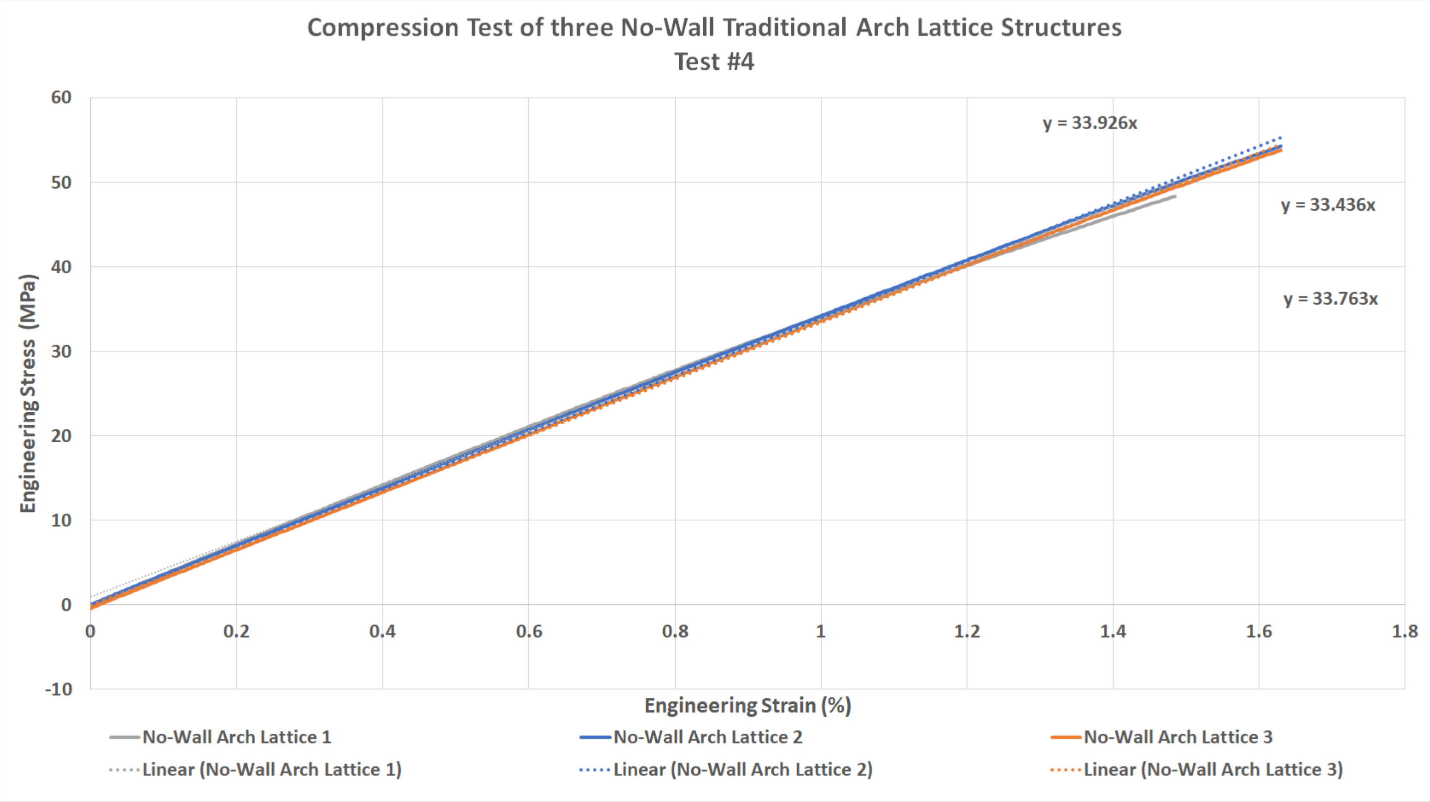

Figure 74: Compression Test of Three No-Wall Traditional Arch Lattice Structures Graph (Stress vs. Strain)

The procedure of Test #4, the compression test of the Traditional Arch lattice structure with no walls, produced consistent data. The engineering stress vs. engineering strain curves seen in Figure 74 demonstrate the elastic portion of deformation of the polymer samples. The derivative of the curves by stress shows Young's modulus of elasticity for the lattice structure. As seen in Figure 74, the modulus values for samples 1, 2, and 3 are 3.376 GPa, 3.393 GPa, and 3.344 GPa accordingly. The consistency in results and the similarity in the values were considered to demonstrate the high quality of the produced data. The graphed experimental results resemble similar trends as those received through numerical simulation. There is a difference in the calculated Young's modulii for experimental data and numerical simulation data. Results from the experimental compression tests produced Young's modulii of around 3.4 GPa and 4.7 GPa

Young's modulus was received through numerical simulation. The difference in results was thought to be caused by the inaccuracy of the Young's modulus value for the Resin provided by the manufacturer, which was used in the numerical simulation. The Structures Team did not have a sufficient amount of time to obtain the accurate value for the elasticity modulus through a laboratory procedure involving dog-bone samples. The similarity in the trends of the compression test results seems to be enough to validate the numerical simulation if proper Young's modulii values are obtained.

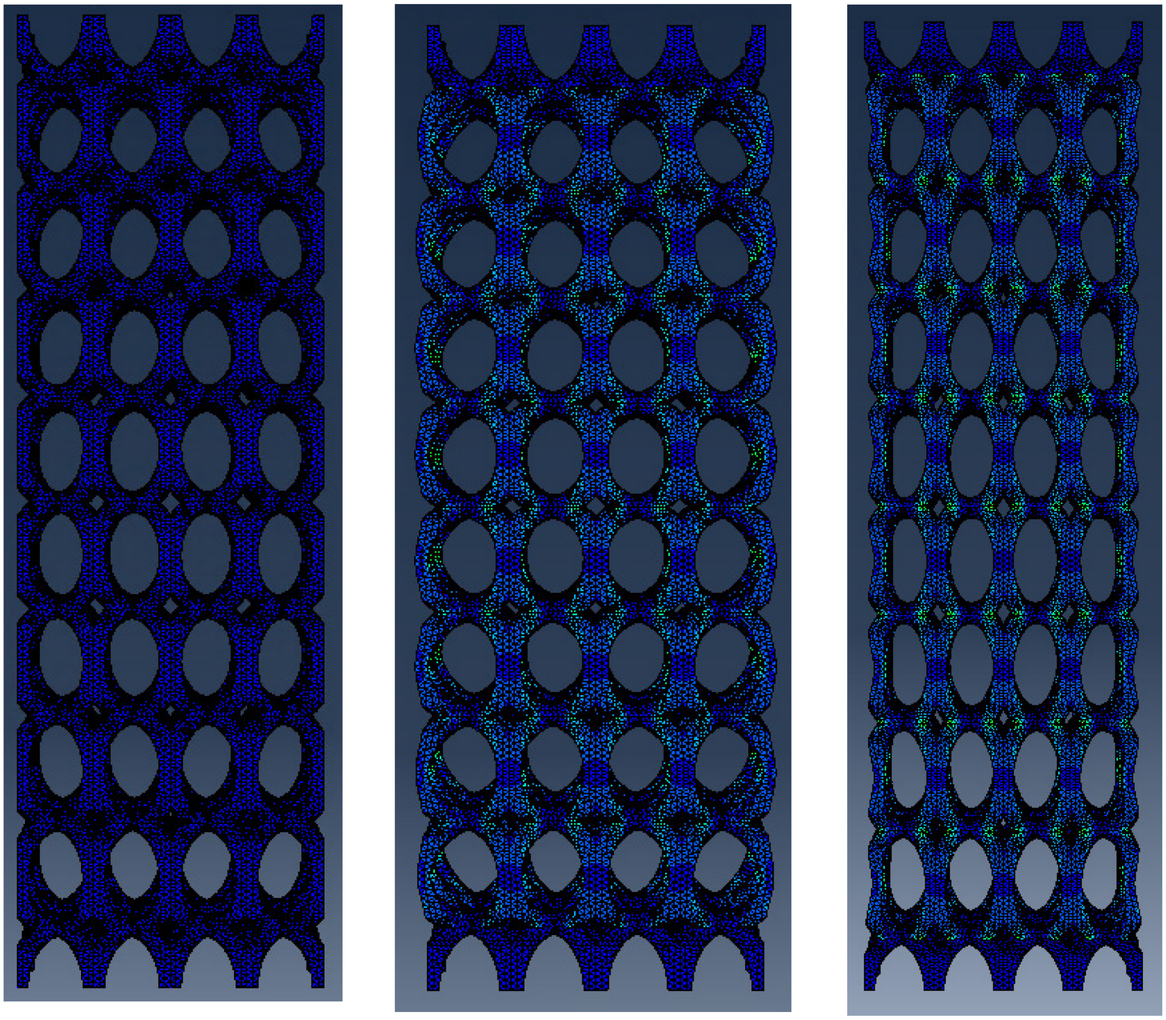

Figure 75: ABAQUS No-Walls Traditional Arch Rectangular Prism Compression (middle) and Tension (right) Test Results

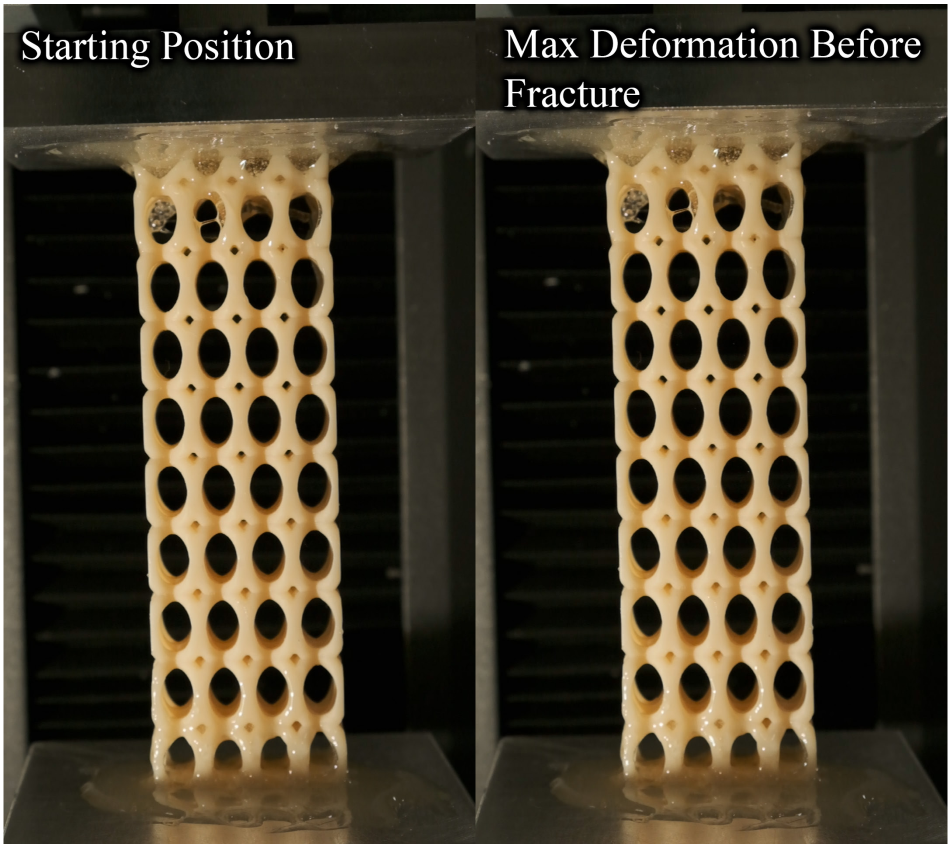

Figure 76: No-Wall Traditional Arch Lattice Structure Compression Test at Initial and Maximum Deformation

The visual comparison of the compression test experimental and numerical simulation results does not compare well enough for validation of the numerical method. The changes in the No-Wall Traditional Arch lattice structure before and during compression in Figures 75 and 76 can be seen to be of different magnitude. The visualization of the numerical model in Figure 75 deforms more than the sample in Figure 76, the difference between the initial and final states are easier to notice in the case of the numerical simulation. Similarly, as in the case with the graphed results, the difference is thought to be caused by the inaccurate modulus of elasticity provided by the 3D printer resin manufacturer. In the case of tensile tests, the difference in visual results was still present. The experimental tensile test fractured the samples, and the numerical models did not fracture due to the lack of plastic deformation and ductile damage information and values to be inputted into the software. The difference in actual and simulated behavior can be seen in Figures 75 and 77. Figures 77 and 78 present the instance at which the fracture on Sample 1 starts and the instance at which Sample 1 fractures completely. The instances are marked in Figure 78 as points "A" and "B".

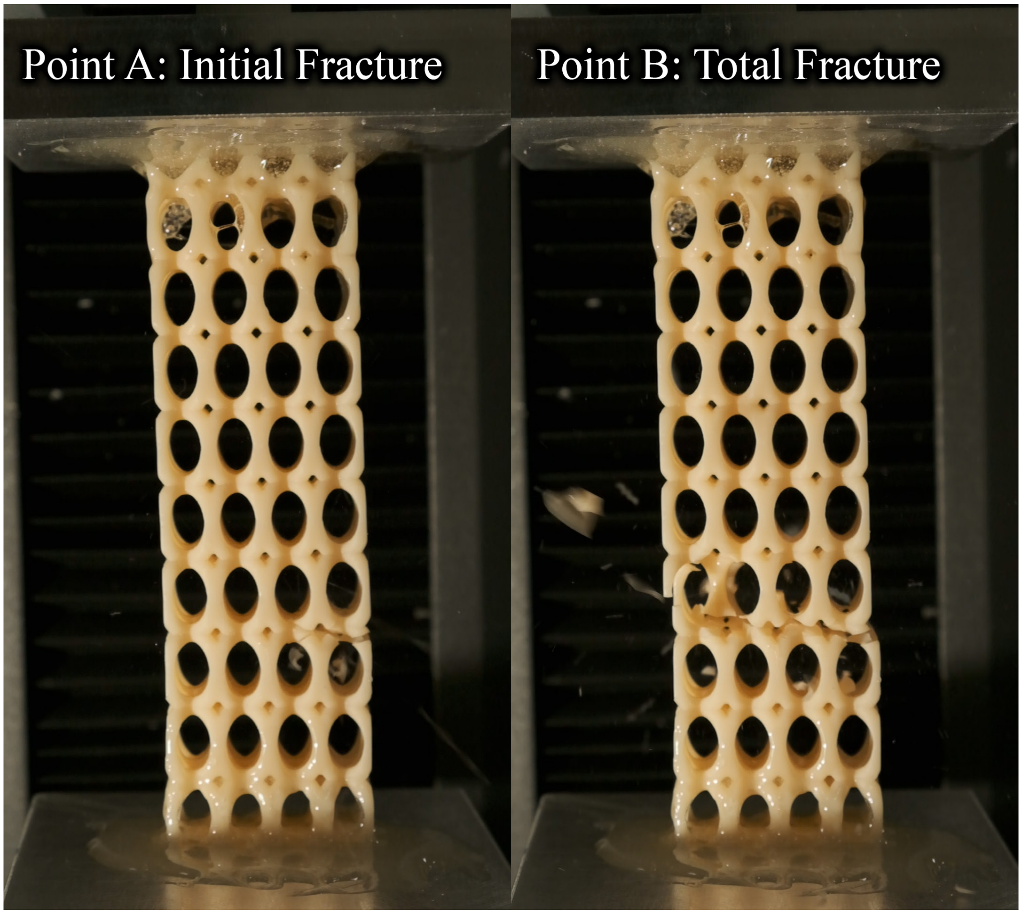

Figure 77: No-Wall Traditional Arch Lattice Structure Tensile Test at Initial and Total Fracture Points: A and B

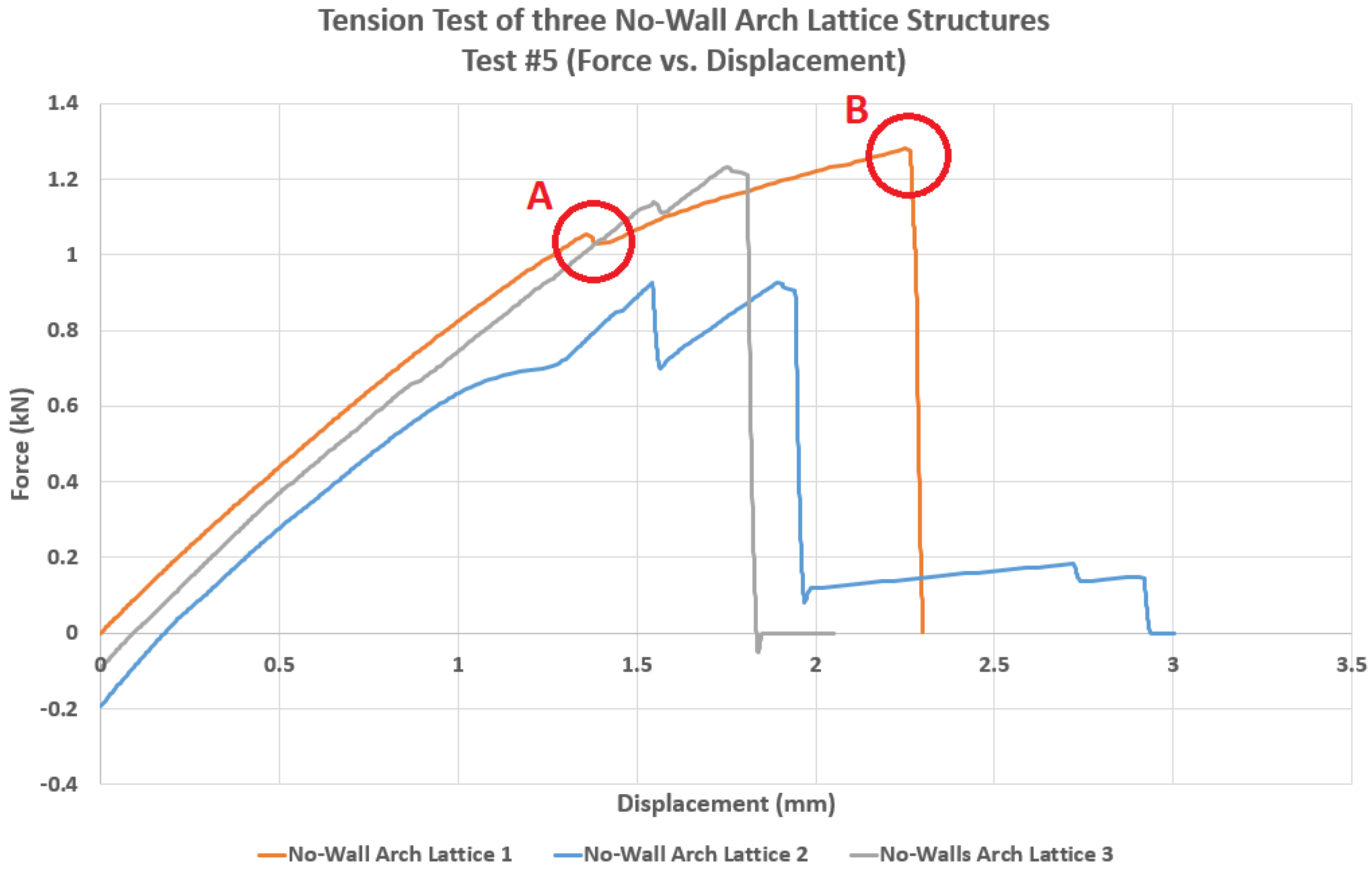

Figure 78: Tension Test of Three No-Wall Traditional Arch Lattice Structures Force vs. Displacement Graph

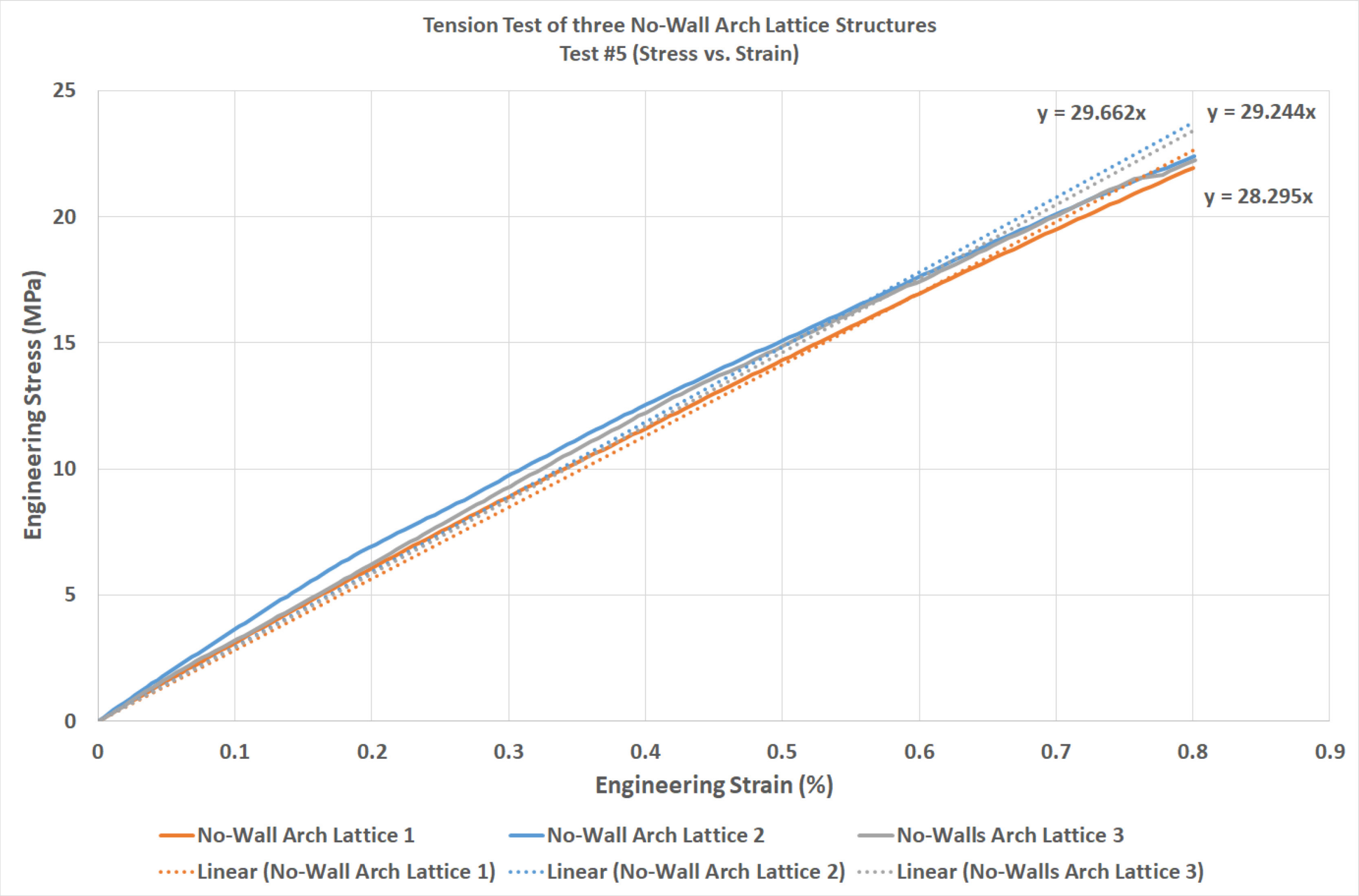

Figure 79: Tension Test of Three No-Wall Traditional Arch Lattice Structures Stress vs. Strain Graph

The tension test results provided in Figure 79 show that the data collected during the experimental procedures are accurate, with a small difference between the results of the three tested samples. The elasticity modulus for the experimental tension test was calculated to be around 3 GPa, which is similar to that of the experimental compression test resulting in values of around 3.4 GPa. The experimental tension graph section shows a similar trend to that of the numerical simulation tension test as seen in Figures 67 and 79. The Young's modulus value, however, is different from the value obtained numerically being around 4.7 GPa. The difference is thought to be caused by the inaccurate elasticity modulus value used in the numerical simulation, which was provided by the 3D printer resin manufacturer.

4. Thermal Analysis

In the thermal team's investigation, three specific thermal and flow properties of lattice structures were selected to be studied through experimentation and simulation. The experimental measurements not only provide preliminary data for the thermal behavior of these materials but also can be employed to validate the results from the corresponding numerical simulations. The three specific properties and their relevance to turbine blade applications are described below.

4.1 Property Selection

Three thermal properties relevant to turbine blade applications were selected to study lattice structures: thermal expansion, heat transfer, and change in air flow velocity. Thermal expansion is an important property for turbine blade performance because turbine blades must not significantly expand in operation, despite the high temperatures of the inlet air. Thermal expansion of the blades could change the shape and the function of the airfoil and may even lead to the blade impacting the nacelle of the engine, causing serious damage to the aircraft. Because of this, a low to zero coefficient of thermal expansion is preferred. As mentioned in the background, there has been previous research into materials and structures with low or negative thermal expansion coefficients as well as research into tuning the thermal expansion coefficients to a specific value [49]. Additionally, there has been extensive research on tailoring the thermal expansion coefficient of the Honeycomb lattice structures. The thermal expansion of each lattice structure will be analytically and experimentally tested and compared.

The second property that will be investigated is heat transfer. Increasing heat transfer away from the turbine blade will reduce high thermal loads on the blade that cause failure [51]. This is the purpose of internal blade cooling, where a coolant fluid is passed through passages in the blade, and the blade is cooled through convection [44]. One of the potential benefits of using lattice structures is their ability to transfer heat away from the turbine blade, thereby reducing the thermal loads applied on the blade itself. From the background research, it was determined that conduction and convection are the main types of heat transfer in the case of air flow through a lattice structure, with radiation effects being negligible. As such, the convective and conductive heat transfer of our structure will be investigated to better understand how effective the structures are at cooling.

Lastly, the change in velocity, and therefore, pressure, of the air surrounding the turbine blade is an important property to account for as well. Minimizing a large velocity drop of the gas before being released as the exhaust is essential to the function of the aircraft [51]. Though most of the energy from the highly compressed hot gas is used by the turbine to create mechanical energy, the remainder of the gaseous energy is released as exhaust, which creates jet thrust. This is an important property to note because there can be a significant change in the velocity of air flow through lattice structures due to the different struts of the structure blocking the air flow.

4.2 Experiments

Three experiments were created to physically test the thermal expansion, heat transfer, and change in velocity of the lattice structures. Each of these experiments was replicated in COMSOL to verify the results. Linear thermal expansion was tested by measuring the length and width of the samples before and after heating. Heat transfer was tested by measuring the change in temperature of hot air after flowing through the lattice structures. The change in velocity was tested by measuring the velocity of air flow before and after flowing through the lattice structures. Each of these experiments required 3D printed samples of the lattice structure designs. See Section 3.1.1 and 3.1.2 for a detailed explanation of this process.

4.2.1 Thermal Expansion

The thermal expansion experiment was created using the following materials: the 3D printed lattice structures, an iPhone camera, a tripod, and an oven. First, the tripod was set up in a stable, secure position on the ground so that the camera height cannot move. The camera was secured on the tripod so that it was facing the top of a table where the lattice structures were to be placed. The camera was at a height approximately 1 foot above the top of the table. The precaution was taken to make sure the camera's position was not moved at all during the procedure so that each photo could be taken at a constant height. Before heating, each lattice structure sample was placed underneath the camera and a photo was taken. The room temperature was taken and recorded.

Next, each lattice structure was heated individually by putting it in the oven on a glass dish for 5 minutes at 150 degrees C. After 5 minutes, the structure was taken out and placed under the camera. A picture was taken as quickly as possible. This was repeated for each lattice structure. Once the lattice structures cooled, the entire procedure was repeated two more times.

After pictures were taken before and after heating for each structure, the length and width of each sample were measured in pixels. This method is possible to use because each picture was taken at a constant height. Each picture was then uploaded to the Paint application. The picture was rotated if necessary so that the structure was straight. Then, using the cursor to carefully outline the edges of the structure, the number of pixels on each side was obtained. This was done several times on the same photo to ensure the number of pixels was as accurate as possible. The length and width of each structure before and after heating was measured this way and recorded. An example of this method can be seen in Figure 80.

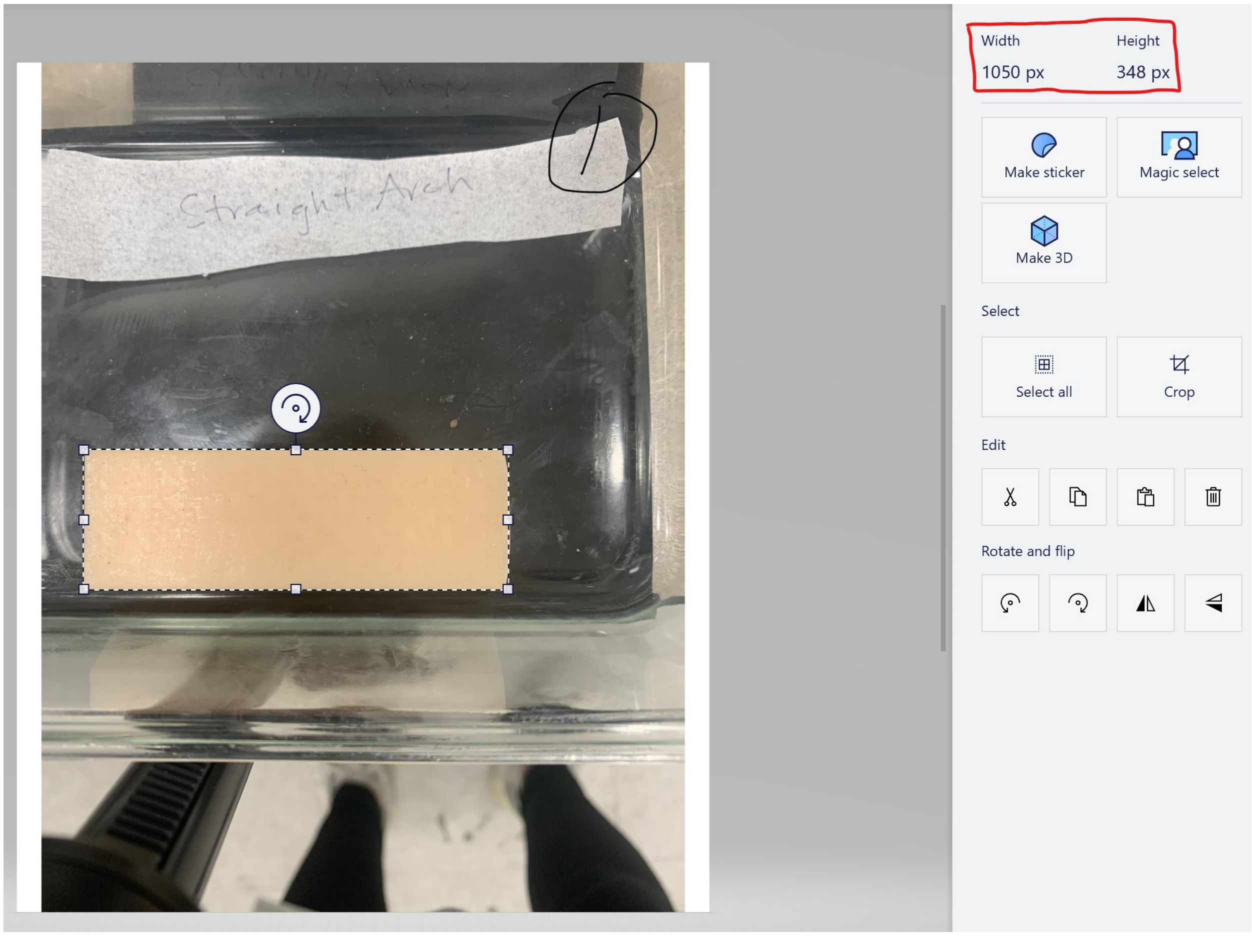

Width 1050 px

Height 348 px

Figure 80: Measuring Length and Width in Pixels for Thermal Expansion Experiment

The linear thermal expansion was found by taking the difference between the length and width of each sample before and after heating. The thermal expansion coefficient for each sample was then calculated by using the equation $\alpha = \frac{dL}{L_0}\frac{1}{dT} = \frac{\varepsilon_T}{dT}$, where L_0 is the original length, dL is the change in length, dT is the change in temperature and ε_T is the thermal strain. These values were calculated and recorded in a table.

4.2.2 Heat Transfer

The heat transfer experiment was created using the following materials: two thermocouples, data logger, two 1 ½ inch diameter, 2 feet long PVC tubes, Blu Tack reusable adhesive putty, three 1 ½ inch diameter, ¼ inch thickness wooden circles, a hair dryer, duct tape, and the 3D printed lattice structure samples.

The overall design of the experiment is to have the lattice structure in the middle of a tube with a hair dryer on one end, and two thermocouples placed before and after the structure to measure the temperature difference. First, wooden holsters were created as a way to hold the lattice structure in the center inside the tube. This was done by laser cutting the 1 ½ inch diameter wooden circles with a ¼ inch thickness. Next, a hole was laser cut in the middle of each circle that matched the length and width of the 3D printed lattice structures. The holes were sanded so that each structure fit tightly in the holster. Figure 81 shows the wooden circles.

Figure 81: Example of Wooden Holsters Created for Thermal Experiments

Next, the PVC pipes were prepared by drilling the holes for the thermocouples. Six inches from the end of the tube, a hole was drilled with the same diameter as the thermocouples. This was done for two of the PVC pipes. After the wooden holsters were created, one of them was then placed inside the end of one of the PVC pipes on the side closest to the hole. The wooden circle was sanded just enough so that it fits tightly and securely inside the pipe. One of the lattice samples was then put into the wooden holster in the PVC pipe. Once the lattice structure was secured inside one end of one of the pipes, we then connected it to the other pipe using duct tape, so that the lattice sample in the wooden circle was secured in the middle of the two connected pipes.

The now 4 foot long PVC pipe was placed on a secure surface in the lab. The hairdryer was connected to one end of the pipe and secured using duct tape. The other end is left open. The thermocouple sensors were then placed in each of the two drilled holes so that the temperature of the air can be recorded. The thermocouples were calibrated ahead of time to ensure accuracy. The holes were sealed using Blu Tack. The entire PVC pipe, hair dryer, and thermocouple setup are shown in Figure 83. The setup was secured to the table using duct tape to hold it in place.

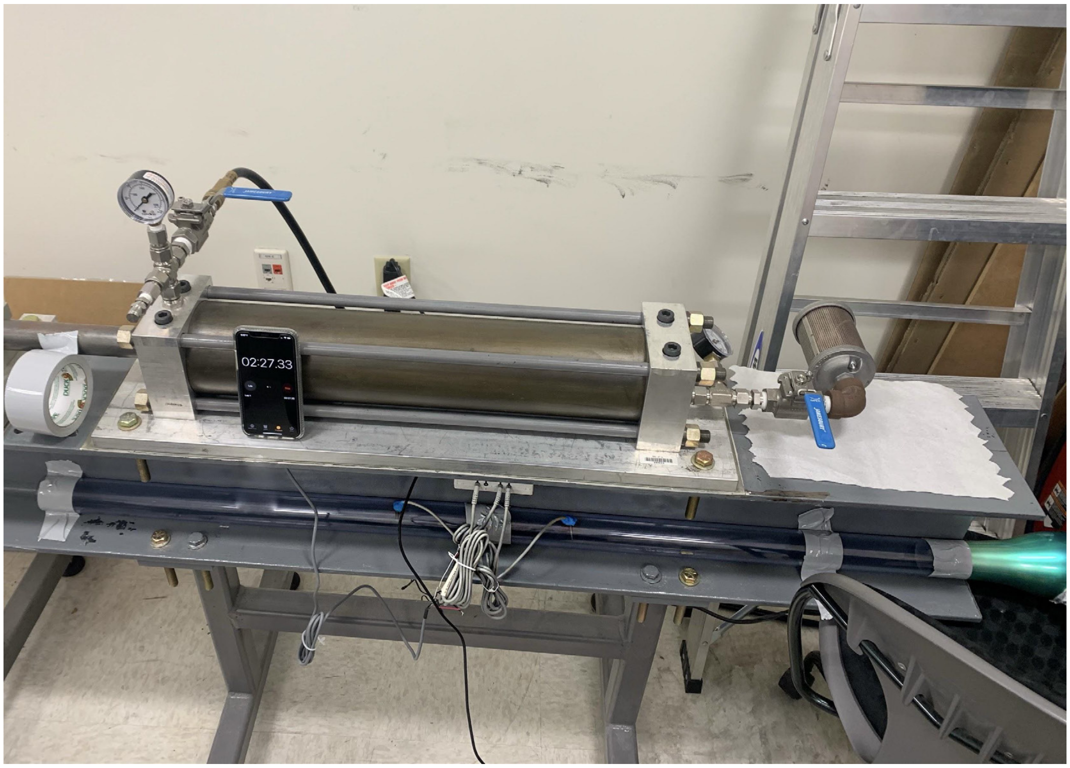

Figure 82: Heat Transfer Experimental Setup. The data logger is magnetically attached to the top plate and is connected to sensors in the pipe.

Once the materials were set up, we connected the thermocouples to the data logger and turned it on. We then turned the hair dryer on and put it on the cool air setting. The air temperature differences before and after the lattice structure were recorded. This was repeated two more times.

The middle of the structure was then taken apart by removing the duct tape. The wooden circle and lattice structure sample were then replaced with the next lattice structure sample and its coordinating wooden holster, and once again sealed using the sealant. The entire procedure was then repeated for every lattice structure sample.

4.2.3 Velocity Change

The velocity change experiment was created using a similar setup to the heat transfer experiment. The velocity change experiment was created using a mini anemometer and all the same materials as the heat transfer experiment, excluding the thermocouples.

This experiment was created using the same tube as the heat transfer experiment. It was modified by sealing the drilled holes with Blu Tack. The wooden holsters were also reused from the previous experiment, once again being used to hold the 3D printed lattice structures in place within the tube. The wooden holsters and lattice structures were secured again by placing them between the two pipes and securing them with duct tape. The mini anemometer was placed an inch away from the opening of the tube and secured in place using tape. The anemometer setup can be seen in Figure 83.

Figure 83: Setup of Mini Anemometer for Velocity Change Experiment

The hair dryer was turned on using the cold setting. The air velocity was measured and recorded by the mini anemometer for thirty seconds at 0.5-second intervals. The data was uploaded from the anemometer to a computer. This was repeated two more times.

The middle of the structure was then taken apart by removing the duct tape. The lattice structure sample was then replaced with the next lattice structure sample, and once again sealed using duct tape. The entire procedure was then repeated for every lattice structure sample for a total of three trials for each structure.

4.3 COMSOL Simulation

The main goal of the simulations was to see how well the different lattice structures would perform in an actual jet turbine environment, as these conditions cannot be replicated in the school laboratory. An additional set of simulations would be set to mimic the experimental conditions in the lab, in which the results would be compared to validate our simulated results and give our simulations based on the conditions of a turbine engine more validity. The simulation software selected was COMSOL, due to its Multiphysics software which allowed for the combination of flow and thermal studies into a singular study. The structures being simulated were designed by the Design Team, and the file was initially converted into an 'STL' file for importing into COMSOL. However, during the STL importing process, the model itself would create faces that were misaligned and even disconnected at times. As such, the lattice structure models were then converted to either IGS or STEP files, which solved all issues with importing. To save time and computing power, all meshes were done as coarse as possible. However, due to the complexities of certain structures, some meshes had to be set to a finer setting for the study to run properly. For all structures, the material was set to either Inconel 718 or resin depending on the simulation. Each simulation will be run twice, one will be set to the conditions of the experimental setup and the other will be set at the expected conditions of a jet turbine. Simulating at the experimental condition allows for the comparison of experimental and simulation results to validate the simulation, giving more credibility to the simulation results at the conditions of a jet turbine. It is important to note that certain structures in COMSOL had to be reduced in size in comparison to the experimental structure since complicated structures such as the prisms made of Arch unit cells significantly increase the computational power and time required for simulation.

4.3.1 Thermal Expansion Simulation

COMSOL has a Multiphysics suite for simulating thermal expansion, which is a combination of the solid mechanics study and the heat transfer in solids study. The goal of the thermal expansion simulation is to simulate the structure as if it was being heated in an oven to match our experimental conditions to validate the results of our simulations in the conditions of a jet turbine. Using these results, the expected coefficient of thermal expansion can be calculated using $\alpha = \frac{dL}{L_0}\frac{1}{dT} = \frac{\varepsilon_T}{dT}$, where L_0 is the original length, dL is the change in length, dT is the change in temperature and ε_T is the thermal strain. These changes in length will be separated by changes in length in the x, y, and z-axis, resulting in a coefficient of thermal expansion for each axis.

Two sets of simulations were conducted for thermal expansion, one set with free constraints and another with fixed constraints. For each set of simulations, unit cells of the three structures, as well as the prism form of the three structures were simulated. The set of simulations with free constraints was designed to calculate the coefficient of thermal expansion of the structure by measuring the change in length and temperature. This can then be compared with data from experiments to validate our findings. Thermal expansion simulation with fixed constraints was mainly designed to simulate the lattice structure in a potential application, such as in a jet turbine, in which the external corners would be attached to a wall or some other structure so that it can't expand or change in size. Between the two, the only difference in simulation methodology is applying said fixed constraints on the structure, whereas in the free constraint, automatic rigid motion suppression is applied for stability. This is done on COMSOL through the Solid Mechanics study, where a Fixed Constraint is selected and the relevant boundaries are highlighted. An example of this is shown in Figure 84, where the areas highlighted in blue and labeled with a red arrow are the fixed constraints.

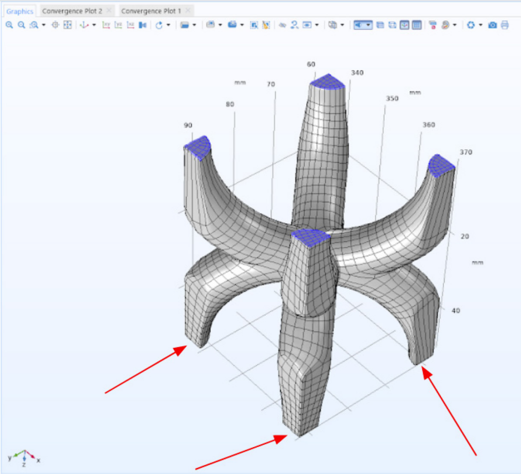

Figure 84: Location of Fixed Constraints in Curved Arch Unit Cell. Red arrows show areas that cannot be seen from this perspective.

On the other hand, for simulations with no fixed constraint, Rigid Motion Suppression needs to be selected across all boundaries, which means that the structure would not be free to rotate in space as a result of the thermal stress for structural stability [47]. For both types of simulations, there are no additional changes left to be made under the Solid Mechanics study. The next part of the study is Heat Transfer in Solids, and the settings here are identical no matter a free or fixed constraint, as all that is needed is the addition of a temperature that is applied to all boundaries. For the simulation in an oven, this temperature was set to 423.15K. Whereas for a simulation under the conditions of a jet turbine, temperatures were set to 1500K based on our research.

For every simulation, a stationary study was conducted to visualize how the structure would behave at equilibrium, which based on our testing process with time-dependent studies took no longer than 3 to 4 seconds at most. Specific details on results will be discussed in a later section.

4.3.2 Flow Property Simulation

COMSOL has several studies for simulating flow, and the ones being considered in this paper are the Laminar flow and Turbulent flow studies. The laminar flow simulations are designed to mimic the hair dryer experiment as close as possible to validate the results of the simulation, whereas the turbulent flow simulations were designed to match the expected conditions of a jet turbine based on our research.

In both studies, an “airbox” was created in addition to the structure in COMSOL. The airbox is essentially a rectangular prism that surrounds the structure with an inlet on one end, an outlet on the other end, with the rest of the sides being set with the wall condition. The structures in question will be prisms formed with multiple copies of the same unit cells, resulting in three different prisms in total. Within the laminar flow study, several boundary conditions were set. Firstly, there is the inlet, which is highlighted in blue in Figure 85 below. For the laminar condition, the airflow was set at 8 m/s into the prism, which was the expected air velocity of the hair dryer.

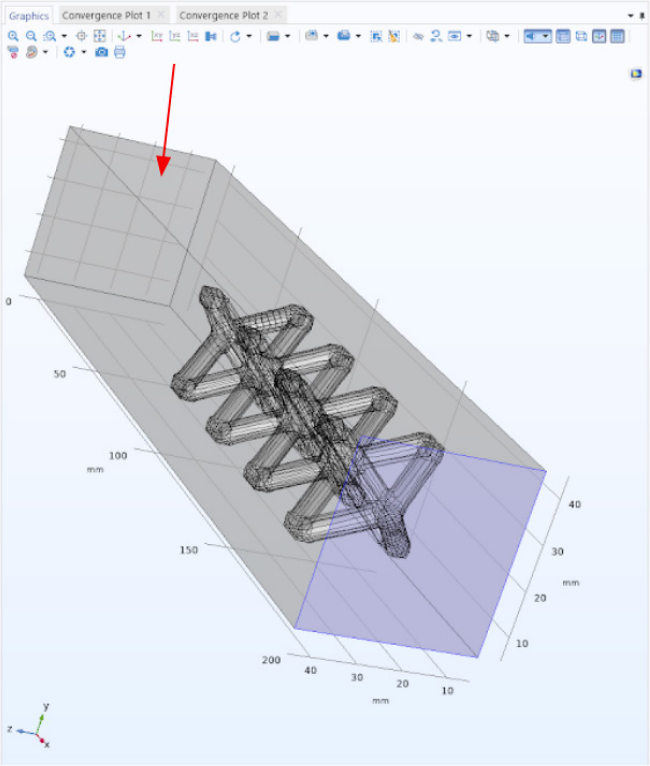

Figure 85: Boundary Conditions of Flow Simulation

The red arrow in the Figure above is the location of the outlet condition, which was set to the atmospheric pressure. The rest of the sides of the airbox are set with a wall condition. For the turbulent flow study, the □ − □ model was selected as it is the best model suited for simulating jet flow, with all other boundary conditions remaining the same as the laminar flow study, except that the magnitude of the inlet velocity is now set at 180 m/s. As a result of these studies, changes in velocity and pressure will be simulated and displayed by COMSOL, the details of which will be discussed in a later section.

4.3.3 Heat Transfer Simulation

To better simulate the heat transfer in both the experimental and jet turbine application, it was decided that an additional study should be combined with the flow simulations, specifically the Heat Transfer in Solids and Fluids study, to simulate the cooling effect due to convection and conduction from the moving air and the structure. In addition to the boundaries set in the flow simulation, the Heat Transfer study set the structure as a solid and the airbox as a fluid. The inflow boundary was at the same location as the flow inlet boundary and was set at the temperature of either 343.15K for a hair dryer or 1500K in the case of a turbine as determined from research. Besides, there was also an additional convective heat flux added to simulate cooling effects due to the structure. For the experimental conditions of 8 m/s, an empirical formula was used to determine the heat transfer coefficient of the air, which was $h_c = 12.12 - 1.16v + 11.6\sqrt{v}$, resulting in a heat transfer coefficient of 35.6498 W/m^2 K where v is the velocity of the air [14]. However, this equation only applies to air velocities from 2 to 20 m/s, and as such, for the jet turbine case, the resulting heat transfer coefficient is set at 250 W/m^2 K based on COMSOL's blog on convective heat transfer [22]. Lastly, the solid also has its thermal conductivity, which for Inconel 718, was automatically determined from COMSOL's material library, whereas for the resin, this value was 1.26 W/mK. The study itself was set as stationary, and the results will be discussed in the next section. It is important to note that due to the complexities in geometry in the Traditional Arch prism, the model had to be defeatured and the protruding edges had to be cut for the flow and heat transfer simulation to successfully run and converge to a solution. As such, the resulting simulation may not be as accurate for Traditional Arch prisms specifically.

4.4 Experimental Results

4.4.1 Thermal Expansion Results

Pictures were taken at a constant height before and after heating each structure for 5 minutes at 150 degrees C. The initial temperature of the room was 20 degrees C. The length and width of each structure were successfully measured in pixels using the Paint application and recorded. Table 3 includes the data that was recorded:

Table 3: Thermal Expansion Experiment Recorded Data

	Initial length and width (pixels)	Length and width after heating (pixels)	The difference in length and width (pixels)
Honeycomb	L = 1066	L = 1102	ΔL = +36
	W = 346	W = 352	ΔW = +6
Simplified Arch	L = 1050	L = 1086	ΔL = +36
	W = 348	W = 355	ΔW = +7
Traditional Arch	L = 1077	L = 1108	ΔL = +31
	W = 343	W = 352	ΔW = +9

After data was collected, the coefficient of thermal expansion for each structure's length and width was calculated using the following equation, $\alpha = \frac{dL}{L_0}\frac{1}{dT} = \frac{\varepsilon_T}{dT}$, where α is the coefficient of thermal expansion, L_0 is the original length, dL is the change in length, dT is the change in temperature, which was 30 degrees C, and ε_T is the thermal strain.

Table 4 shows the resulting thermal expansion coefficients:

Table 4: Experimental Coefficients of Thermal Expansion

	Coefficient of thermal expansion length, $\alpha_{\square}$	Coefficient of thermal expansion width, $\alpha_{\square}$
Honeycomb	$\alpha_{\square} = 1.126 \times 10^{-3}$	$\alpha_{\square} = 5.780 \times 10^{-4}$
Simplified Arch	$\alpha_{\square} = 1.143 \times 10^{-3}$	$\alpha_{\square} = 6.705 \times 10^{-4}$
Traditional Arch	$\alpha_{\square} = 9.595 \times 10^{-4}$	$\alpha_{\square} = 8.746 \times 10^{-4}$

As previously discussed, a low coefficient of thermal expansion is preferred for turbine applications. It can be observed that the Honeycomb structure had the lowest coefficient of thermal expansion for width and the traditional arch had the lowest coefficient of thermal expansion for length. The Simplified Arch had the highest coefficient of thermal expansion for length and the Traditional Arch for width.

4.4.2 Heat Transfer Results

The heat transfer experiment was successfully executed and data were obtained for the temperature drop of hot air after flowing through the lattice structures. A temperature difference baseline was recorded first, with only the wooden holster in the tube. The baseline was then subtracted from the recorded temperature change values with the lattice structures to account for heat transfer due to the wooden holsters. These calculations were done in Excel by exporting the CSV files. Averages were taken for three trials. The following figure illustrates the data:

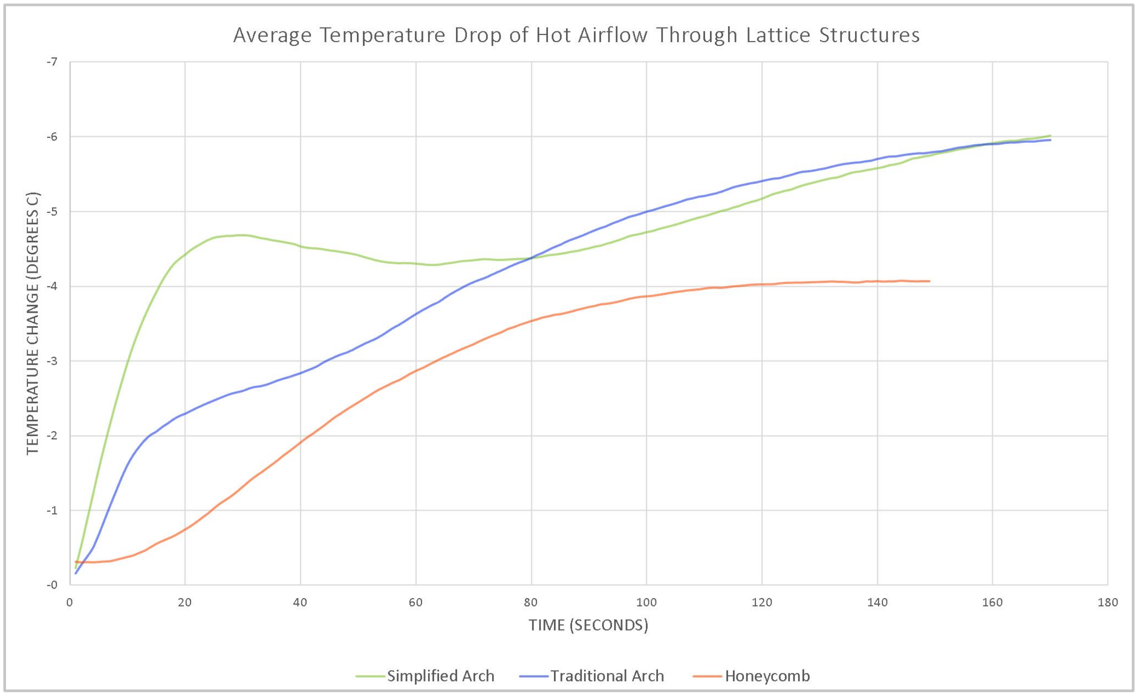

Figure 86: Heat Transfer Experimental Results. The average temperature drop of air of the Arch structures is similar, and lower for the Honeycomb structure.

The Honeycomb lattice structure performed the worst in terms of heat transfer, with a maximum temperature change of 4.07 degrees C after 148 seconds. The Simplified Arch and Traditional Arch structure performed similarly to one another. Both structures were able to reach a temperature change of 5.95 degrees C after 170 seconds. It can be observed that the rate of change of heat transfer varies for each structure over time. The Simplified Arch structure was able to quickly absorb more heat than the other two structures after 30 seconds, before slightly dipping and then flattening out. Although the heat transfer experiment was unable to be run for longer than three minutes at a time due to the hair dryer overheating, the change in temperature for each lattice structure appears to become more constant over time.

4.4.3 Velocity Change Results

From the experimental setup described above, the air velocity sensor resulted in data for a baseline test of each of the structures as well as the structures themselves, totaling six datasets in the form of CSV files. These CSV files were exported into Excel, in which the average air velocity of all six datasets was calculated. The average baseline air velocity of each structure was subsequently subtracted with the corresponding average air velocity of each structure, resulting in a value for the difference in air velocity as a result of each structure. The following results were plotted in a bar chart below to allow for easier comparison.

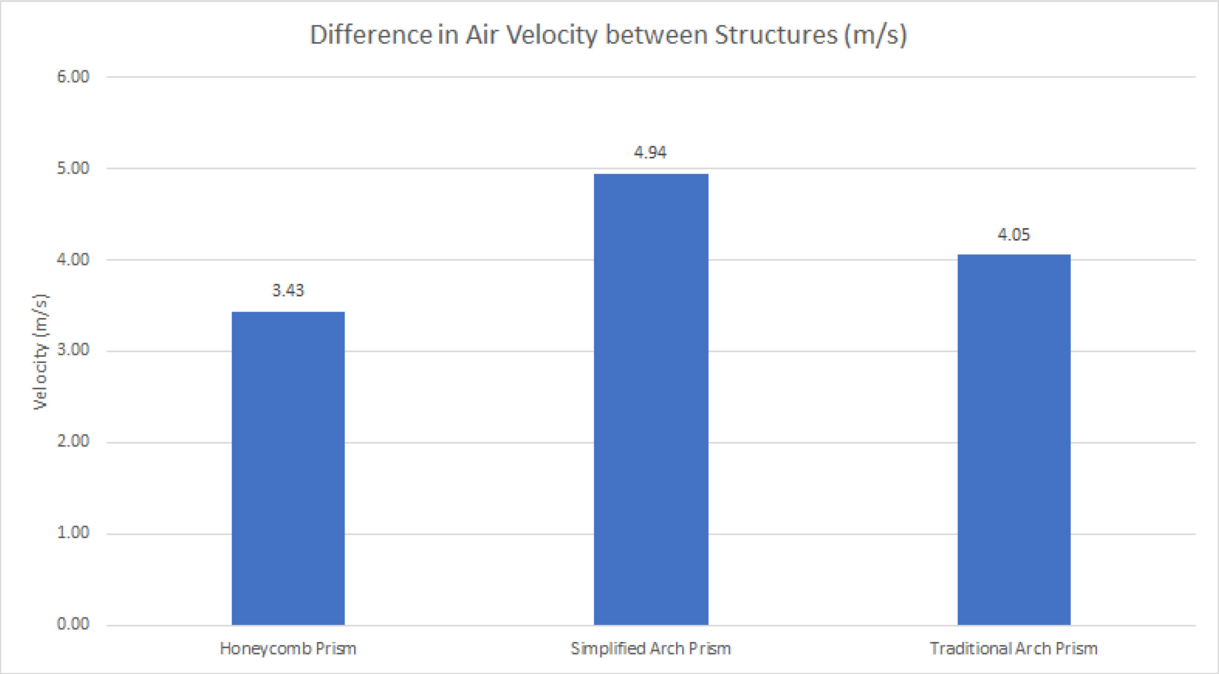

Figure 87: Average Difference in Velocity Between Baseline and Structure

As seen from Figure 87 above, the Simplified Arch prism structure has the largest drop in air velocity with a value of 4.94 m/s. In comparison, the Traditional Arch prism and Honeycomb prism had smaller differences with values of 4.05 m/s and 3.43 m/s respectively. Based on the research from earlier, large drops in air velocity are undesirable, as such the overall trend seems to be that Honeycomb prisms are best suited for the task when it comes to reducing the drop in air velocity, with the Traditional Arch prism being a close second and the simplified arch prism being the worst. Honeycomb prisms being the best structures out of the three that were tested in terms of reducing the drop in air velocity was to be expected. While both the Simplified and Traditional Arch prism structures include struts that "cut" across in a direction normal to the airflow, the Honeycomb prisms only have the walls of the hexagons themselves acting as a barrier to the airflow, with the rest of the structure consisting essentially of honeycomb tubes that are unlikely to restrict airflow. Hence, it was hypothesized that Honeycomb prisms would fare better than both

Arch prism structures in terms of reducing the drop in air velocity and the data seems to support this trend.

4.5 Simulation Results

4.5.1 Thermal Expansion Simulation Results

The first set of thermal expansion simulation results will be based on the free constraint simulations. The first structure to be simulated was the Simplified Arch unit cell with Inconel 718 as the material. In Figure 88, the wireframe rendering of the structure is the shape of the structure at room temperature and the structure that is colored is the structure after heating, with the color gradient representing the displacement magnitude of the structure. By comparing the two, it is clear that there is expansion throughout the unit cell. The overall magnitude of change in length is in the range of millimeters, and as mentioned earlier, is split into three axes. To calculate the thermal strain, the displacement data from COMSOL was exported as a text file that included the coordinates of each point and the magnitude of displacement for said point. This was then imported into Excel, where maximum and minimum values can be retrieved and used in the thermal strain equation. The resultant thermal strain in the three directions was calculated to be $\varepsilon_{\square\square} = 0.026682$, $\varepsilon_{\square\square} = 0.022207$ and $\varepsilon_{\square\square} = 0.021678$. The temperature change is calculated by subtracting the jet turbine inlet temperature by the room temperature, or $1500 - 293.15 = 1206.85\square$. Using these results in the formula for the coefficient of thermal expansion gives $\alpha_{\square} = 2.21092 \times 10^{-5}\ \square^{-1}$, $\alpha_{\square} = 1.84005 \times 10^{-5}\ \square^{-1}$ and $\alpha_{\square} = 1.79627 \times 10^{-5}\ \square^{-1}$.

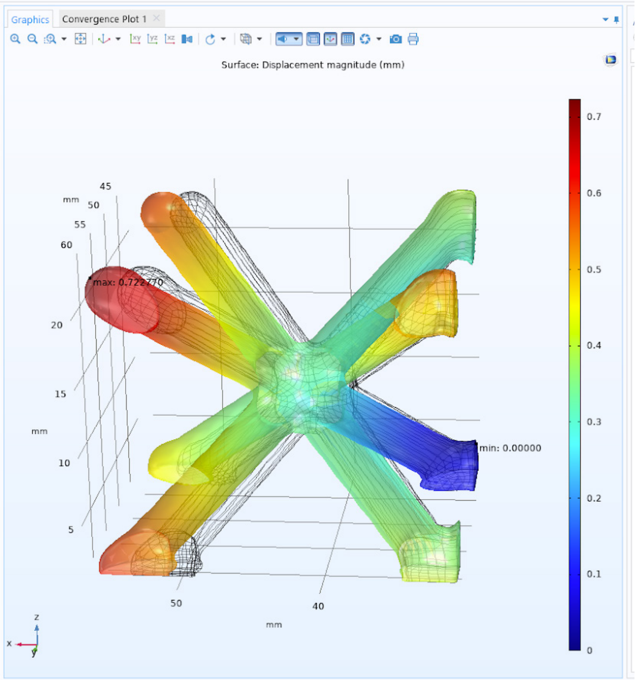

Figure 88: Simplified Arch Unit Cell Free-Displacement Magnitude for Inconel 718

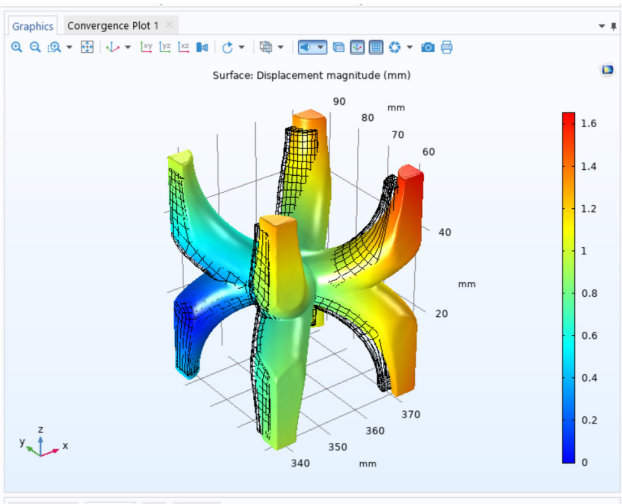

Figure 89: Traditional Arch Unit Cell Free-Displacement Magnitude for Inconel 718

Using a similar method, the thermal strain and coefficient of thermal expansion were calculated for the traditional arch unit cell under the same conditions as well, as seen in Figure 89.

The resultant thermal strain in the three directions was calculated to be $\varepsilon_{\square\square} = 0.017339$, $\varepsilon_{\square\square} = -0.027411$ and $\varepsilon_{\square\square} = -0.001808$, giving a coefficient of thermal expansion of $\alpha_{\square} = 1.43678 \times 10^{-5}\ \square^{-1}$, $\alpha_{\square} = -2.27134 \times 10^{-5}\ \square^{-1}$ and $\alpha_{\square} = -1.49888 \times 10^{-6}\ \square^{-1}$. A summary of the thermal strains and coefficients of thermal expansion for both unit cells can be found in Table 5 below.

Table 5: Summary of Thermal Strains and Coefficient of Thermal Expansion for Two Different Unit Cells (Inconel 718)

Inconel 718	Simplified Arch Unit Cell	Traditional Arch Unit Cell
$\varepsilon_{\square\square}$	0.026682	0.017339
$\varepsilon_{\square\square}$	0.022207	-0.027411
$\varepsilon_{\square\square}$	0.021678	-0.001808
$\alpha_{\square}$ ($\square^{-1}$)	2.21092×10^{-5}	1.433678×10^{-5}
$\alpha_{\square}$ ($\square^{-1}$)	1.84005×10^{-5}	-2.27134×10^{-5}
$\alpha_{\square}$ ($\square^{-1}$)	1.79627×10^{-5}	-1.49888×10^{-6}

As expected, under no constraints, the unit cells expand along their struts, which for the Simplified Arch unit cell is along the diagonals, where the struts stretch and grow. As for the Traditional Arch unit cell, this expansion was mainly in the x-direction, but the structure of the unit cell itself meant that stretching in the x-direction resulted in a narrowing effect in the other axes, resulting in negative coefficients of thermal expansion in the y and z-direction.

The next set of thermal expansion simulations were done on the prism structures, specifically the Honeycomb prism, Simplified Arch prism, and Traditional Arch prism. Their resultant thermal strains and coefficients of thermal expansion in all three directions are summarised in Table 6 below. Here, the z-direction describes the direction parallel to the hexagonal tubes, with the x-direction set as the width of the prism and the y-direction, is set as the height. This was the same set of dimensions for the Traditional Arch prism as well, but the Simplified Arch prism has the x-direction going along the structure, with the y-direction denoting width and the z-direction representing height. A visualization of this can be seen in the COMSOL screenshots below in Figures 90 to 99, and a summary of the results can be found in Table 6 below.

Table 6: Summary of Thermal Strains and Coefficient of Thermal Expansion for Three Different Prisms (Inconel 718)

Inconel 718	Honeycomb Prism	Simplified Arch Prism	Traditional Arch Prism
$\varepsilon_{\square\square}$	0.003267	0.020236	0.011108
$\varepsilon_{\square\square}$	0.000385	-0.025515	-0.000389
$\varepsilon_{\square\square}$	0.020649	0.016191	0.007156
$\alpha_{\square}$ ($\square^{-1}$)	2.70758×10^{-6}	1.67674×10^{-5}	9.20423×10^{-6}
$\alpha_{\square}$ ($\square^{-1}$)	3.19186×10^{-7}	-2.11417×10^{-5}	-3.22597×10^{-7}
$\alpha_{\square}$ ($\square^{-1}$)	1.71106×10^{-5}	1.34161×10^{-5}	5.92948×10^{-6}

As seen in Table 6 above, the main difference is that the Honeycomb naturally expands in height and width, but shrinks slightly along the direction of the hexagonal tubes. As for the Simplified Arch prism, the largest change is a shrink in width, as the structure seems to tend to expand along its length and height, effectively stretching the structure out. This is similar to the Traditional Arch prism, where its width is reduced as well due to a similar stretching effect in the other two directions. However, it seems that both the Traditional Arch and Honeycomb prism resist thermal expansion better than the Simplified Arch prism under no constraints.

The next set of thermal expansion simulation results will be based on the fixed constraint simulations. Similarly, this was conducted for both the unit cells as well as the prism structures to allow for comparison and to assist in spotting any trends in results. The pairs of figures below depict the location of the fixed constraints on either unit cell or prism on the left and the results of the simulation on the right.

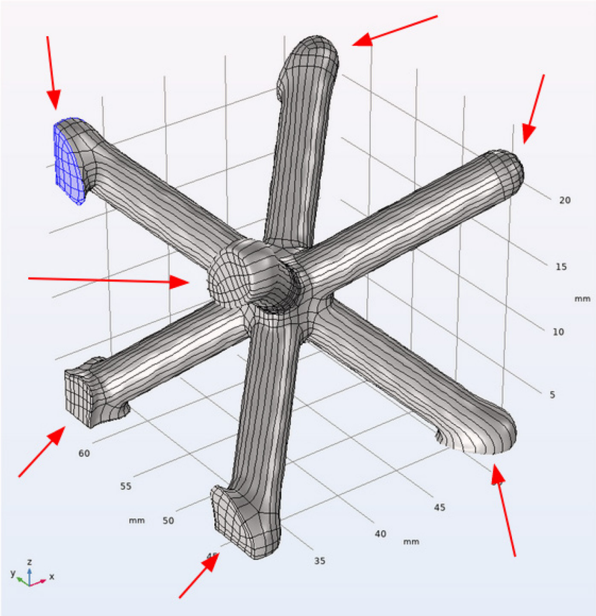

Figure 90: Location of Fixed Constraints on Simplified Arch Unit Cell for Inconel 718

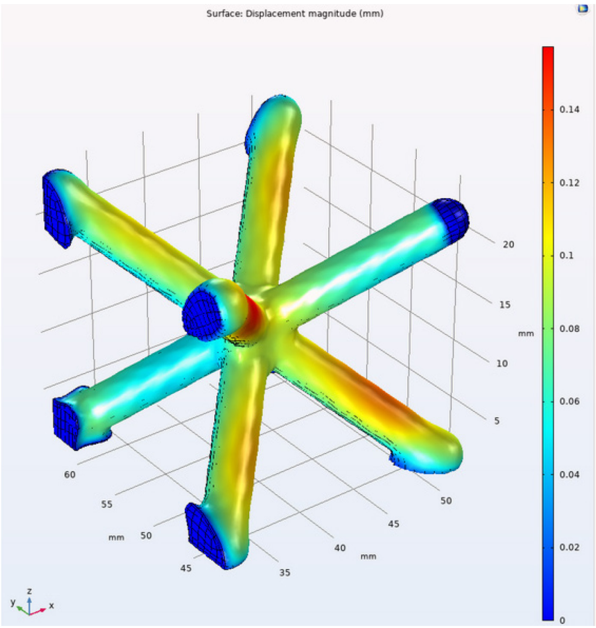

Figure 91: Results of Thermal Expansion of Simplified Arch Unit Cell for Inconel 718

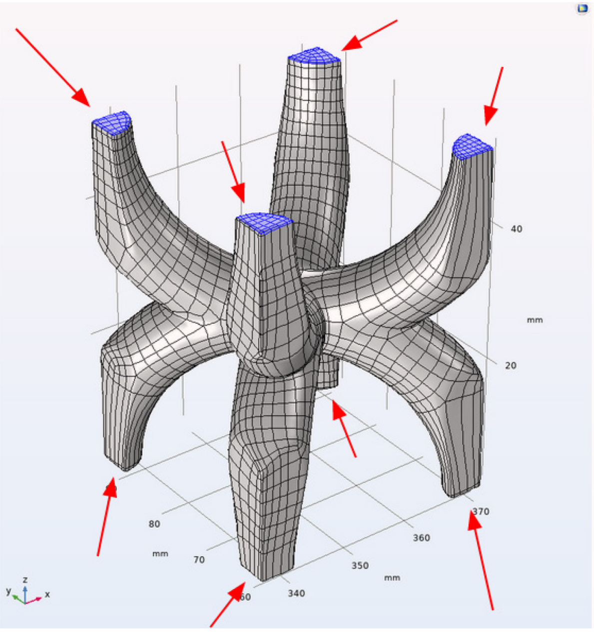

Figure 92: Location of Fixed Constraints on Traditional Arch Unit Cell for Inconel 718

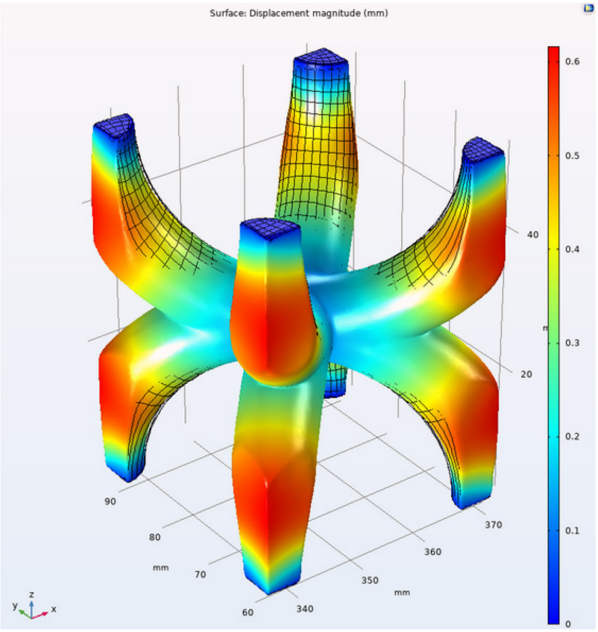

Figure 93: Results of Thermal Expansion of Traditional Arch Unit Cell for Inconel 718

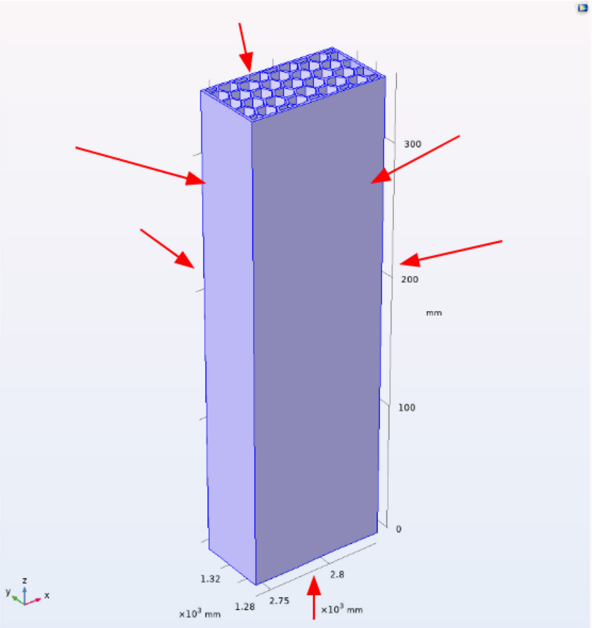

Figure 94: Location of Fixed Constraints on Honeycomb Prism for Inconel 718

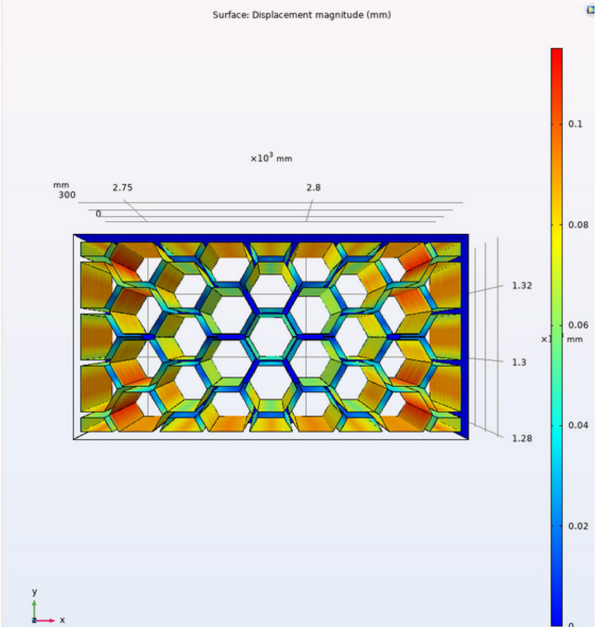

Figure 95: Results of Thermal Expansion of Honeycomb Prism for Inconel 718

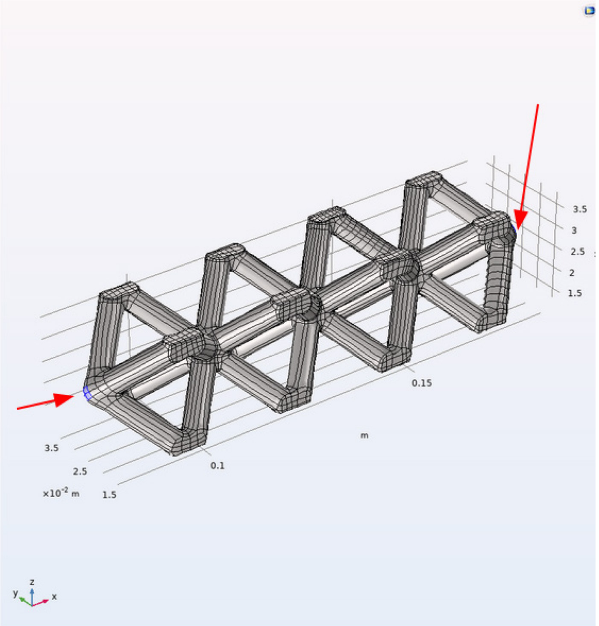

Figure 96: Location of Fixed Constraints on Simplified Arch Prism for Inconel 718

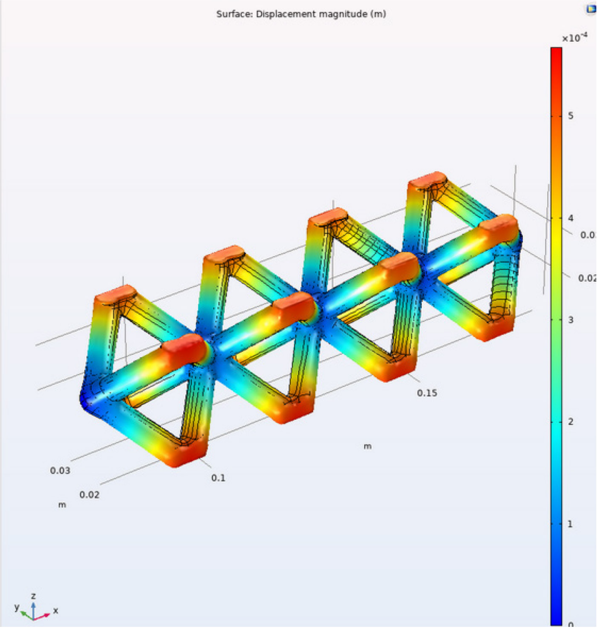

Figure 97: Results of Thermal Expansion of Simplified Arch Prism for Inconel 718

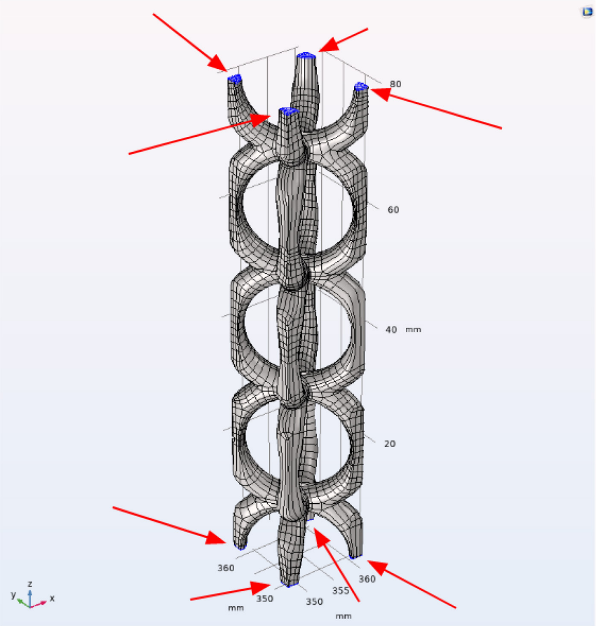

Figure 98: Location of Fixed Constraints on Traditional Arch Prism for Inconel 718

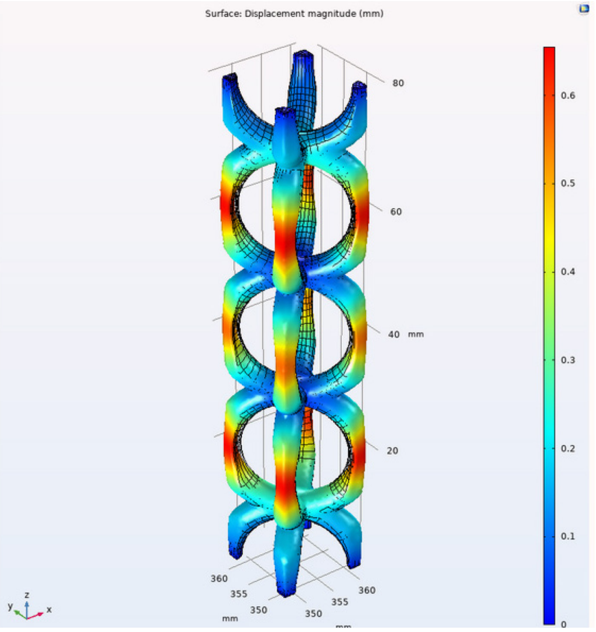

Figure 99: Results of Thermal Expansion of Traditional Arch Prism for Inconel 718

Unlike the simulations with the free constraint, in which the unit cells were free to expand, under a constrained situation, the struts of the unit cells exhibit very mild bending, with the largest displacement usually located in the mid-section of each strut for the Simplified Arch unit cell. In comparison, the Traditional Arch unit cell has a greater magnitude of displacement and has its maximum displacement located around the outer curves and corners of the structure.

As for the Honeycomb prism, given that the external walls were set as fixed constraints, all of the expansion was located along the edges of the tubes, but the magnitude of this expansion was small, with the maximum being a bit larger than 0.1 mm. The Simplified Arch structures were even more resilient to expansion, with a maximum displacement of approximately 0.0005 mm. Unsurprisingly, the thermal stresses were concentrated on the edges of the structures, with the struts themselves exhibiting minimal expansion or bending. Lastly, there was the Traditional Arch prism, which had the largest magnitude of displacement of 0.65 mm, and all of these stresses were concentrated on the struts that connected each unit cell. Overall, the simulation results are as expected, with most thermal stresses concentrated on edges and boundaries, and the overall trend of the Traditional Arch expanding the most under the same thermal load stays consistent between both the unit cell and the prism structure. After the simulations with Inconel 718 as the material of choice, the same set of simulations were completed with the UV cured resin.

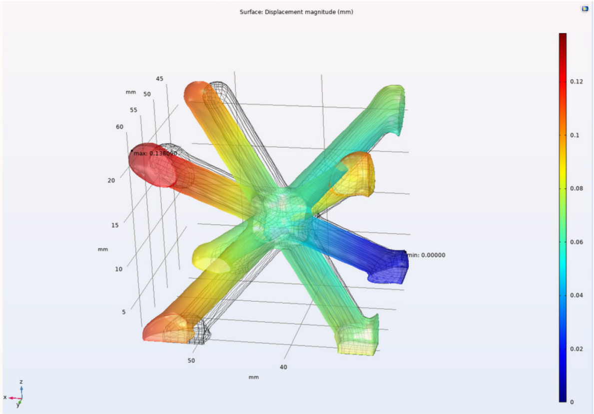

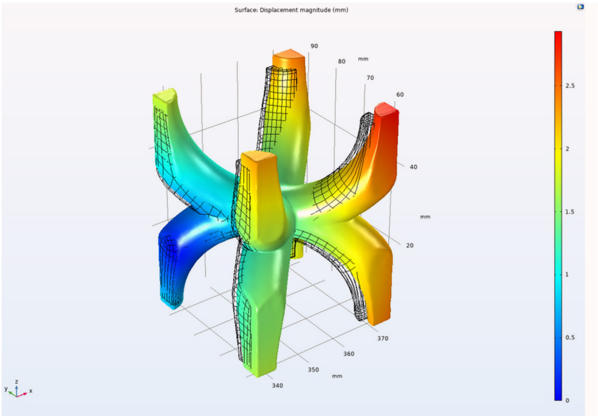

Figure 100: Results of Free Thermal Expansion of Simplified Arch Unit Cell for Resin

Figure 101: Results of Free Thermal Expansion of Traditional Arch Unit Cell for Resin

Table 7: Summary of Thermal Strains and Coefficient of Thermal Expansion for Two Different Unit Cells (Resin)

Resin	Simplified Arch Unit Cell	Traditional Arch Unit Cell
$\varepsilon_{\square\square}$	0.005097	0.002342
$\varepsilon_{\square\square}$	0.004242	-0.003703
$\varepsilon_{\square\square}$	0.004142	-0.000244
$\alpha_{\square}$ ($\square^{-1}$)	3.92141×10^{-5}	1.80187×10^{-5}
$\alpha_{\square}$ ($\square^{-1}$)	3.26363×10^{-5}	-2.84849×10^{-5}
$\alpha_{\square}$ ($\square^{-1}$)	3.18598×10^{-5}	-1.87974×10^{-6}

Table 8: Summary of Thermal Strains and Coefficient of Thermal Expansion for Three Different Prisms (Resin)

Resin	Honeycomb Prism	Simplified Arch Prism	Traditional Arch Prism
$\varepsilon_{\square\square}$	0.000529	0.003866	0.002122
$\varepsilon_{\square\square}$	5.20379×10^{-5}	-0.004874	-7.4383×10^{-5}
$\varepsilon_{\square\square}$	0.002771	0.003093	0.001367
$\alpha_{\square}$ ($\square^{-1}$)	4.07452×10^{-6}	2.97397×10^{-5}	1.63252×10^{-5}
$\alpha_{\square}$ ($\square^{-1}$)	4.00292×10^{-7}	-3.74982×10^{-5}	-5.72177×10^{-7}
$\alpha_{\square}$ ($\square^{-1}$)	2.13138×10^{-5}	2.37957×10^{-5}	1.05169×10^{-5}

As expected, the overall trends in the simulation are the same between the simulation for Inconel and the resin, with the change in magnitudes occurring due to the difference in material properties. The simulations for the fixed constraints were also done for resin, with the fixed constraints remaining the same as the simulation for the Inconel simulation. The resulting displacement of each structure can be seen in the figures below.

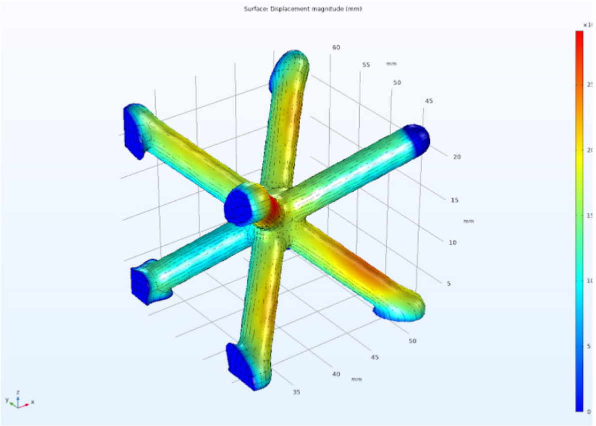

Figure 102: Results of Fixed Thermal Expansion of Simplified Arch Unit Cell for Resin

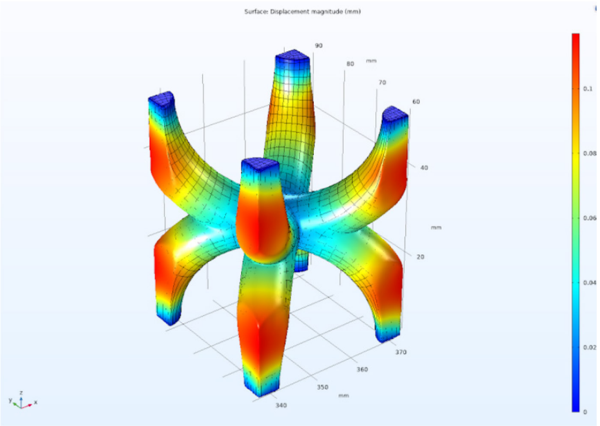

Figure 103: Results of Fixed Thermal Expansion of Traditional Arch Unit Cell for Resin

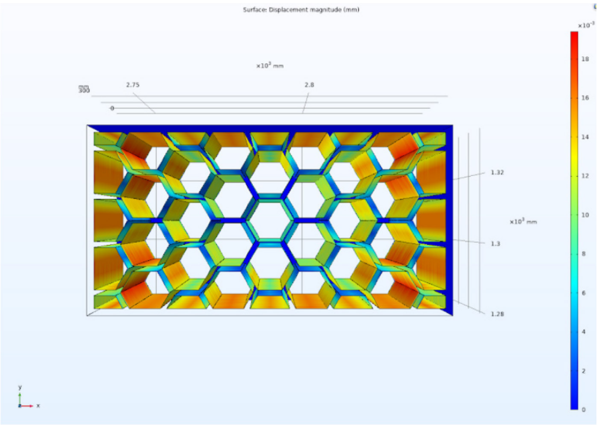

Figure 104: Results of Fixed Thermal Expansion of Honeycomb Prism for Resin

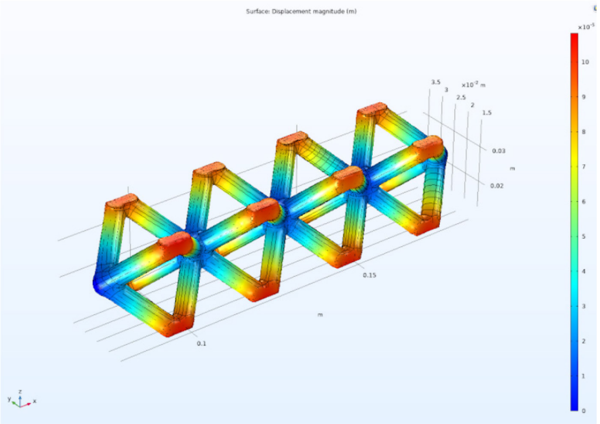

Figure 105: Results of Fixed Thermal Expansion of Simplified Arch Prism for Resin

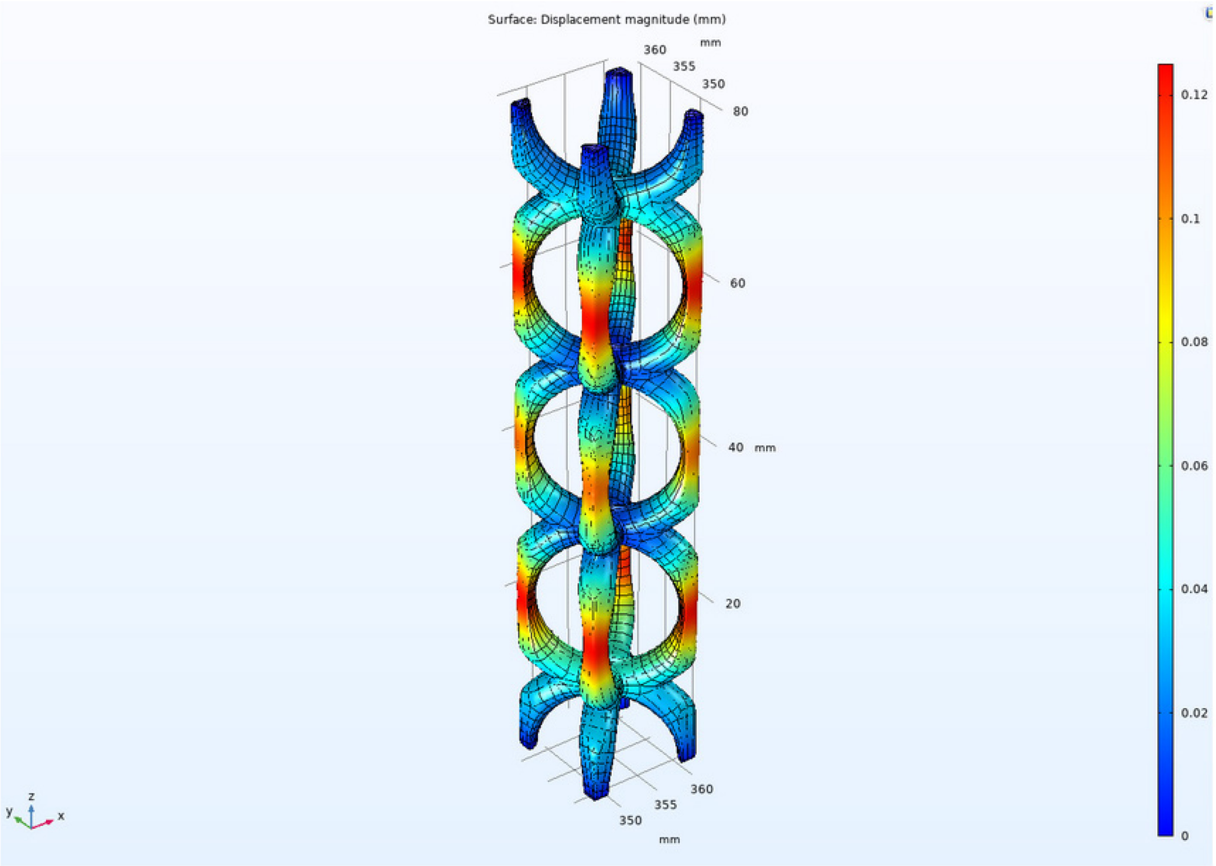

Figure 106: Results of Fixed Thermal Expansion of Traditional Arch Prism for Resin

Similar to the simulations with no constraints, the overall trend of where maximum displacement is located is the same between both structures, which is normally in the edges of the prism where each unit cell connects. Just as before, the Traditional Arch has the largest magnitude of expansion based on this simulation. A possible reason for this could be due to the geometries of the unit cells each prism is made of. For simulations with the unit cell, the Traditional Arch had a larger displacement than the simplified arch, so naturally, the Traditional Arch prism is expected to have a larger displacement than the Simplified Arch prism. The geometry of the Simplified Arch essentially consists of multiple straight beams, meaning there are few curves except at the ends and where the beams intersect with each other. In comparison, the Traditional Arch unit cell has curves and sharp corners. Based on the simulations, it seems the thermal stresses generally concentrate along with thin, sharp corners, hence why the Traditional Arch unit cell experiences greater thermal expansion and as a result, so does the Traditional Arch prism.

4.5.2 Flow Simulation Results

The first set of simulations will be of the turbulent flow study. The structures that were studied are the Honeycomb prism, the Simplified Arch prism, and the Traditional Arch prism respectively, and their resulting air velocity and pressure plots can be seen in the figures below. For the velocity results, only the velocity on one plane was plotted to assist with image quality. The next group was set using the laminar flow study to simulate the conditions of the experimental setup.

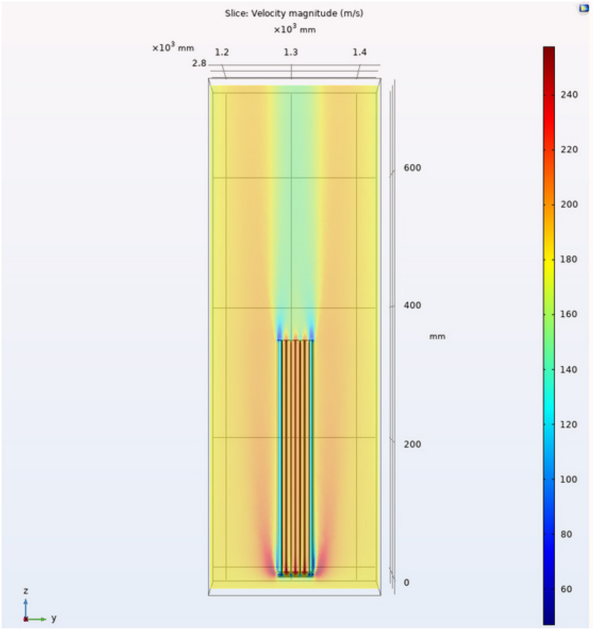

Figure 107: Air Velocity for Honeycomb Prism at 180 m/s

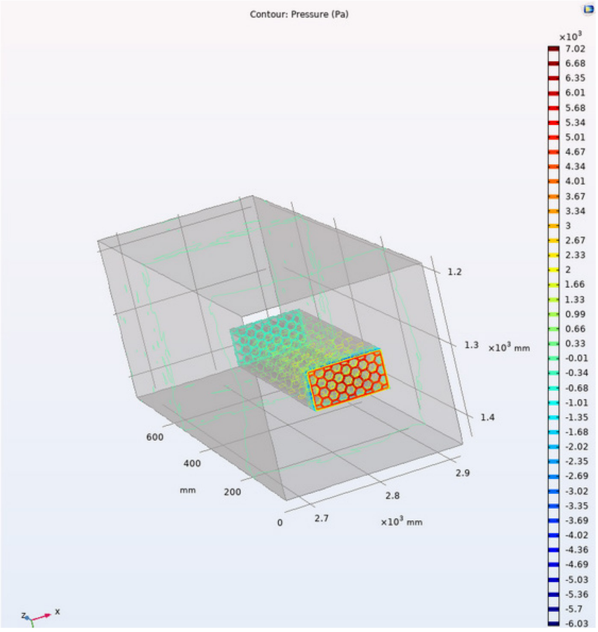

Figure 108: Pressure for Honeycomb Prism at 180 m/s

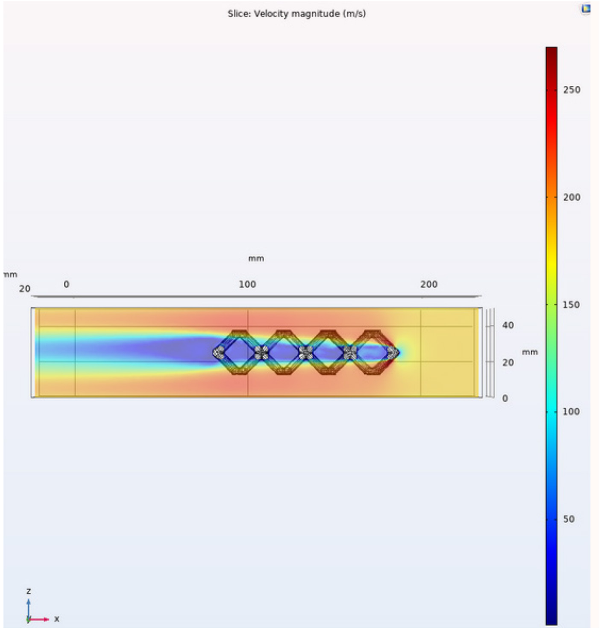

Figure 109: Air Velocity for Simplified Arch Prism at 180 m/s

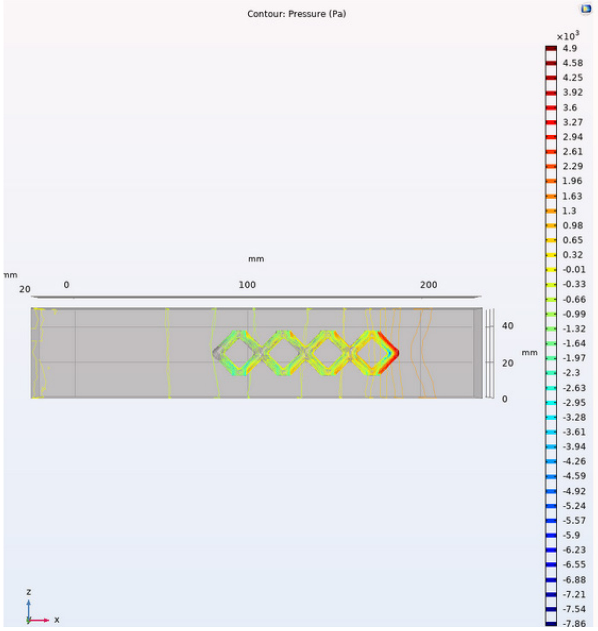

Figure 110: Pressure for Simplified Arch Prism at 180 m/s

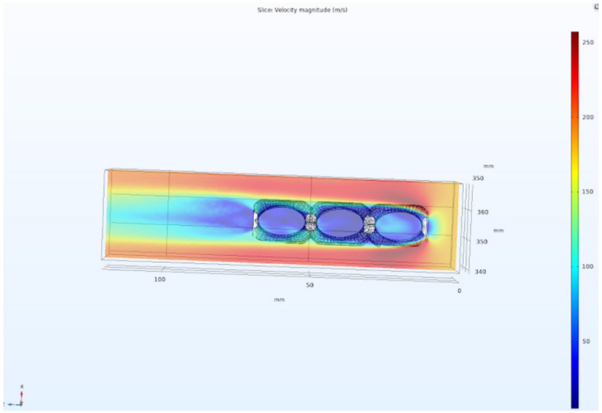

Figure 111: Air Velocity for Traditional Arch Prism at 180 m/s

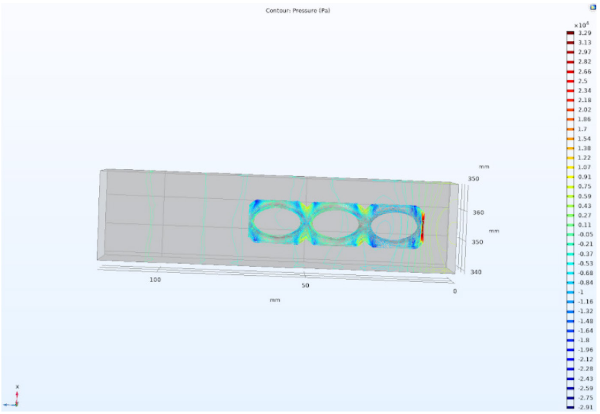

Figure 112: Pressure for Traditional Arch Prism at 180 m/s

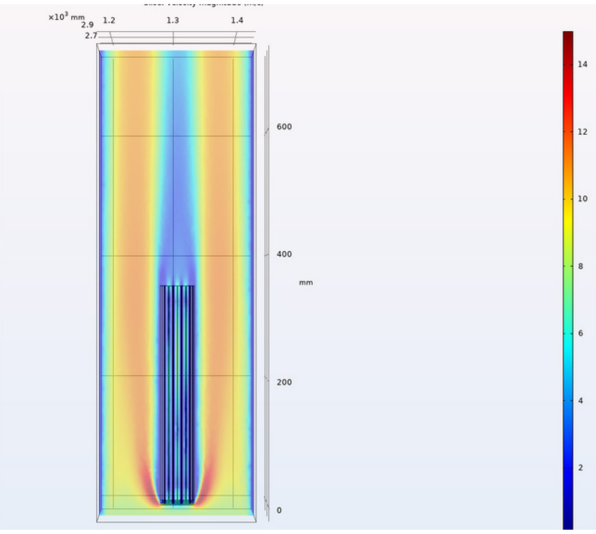

Figure 113: Air Velocity for Honeycomb Prism at 8 m/s

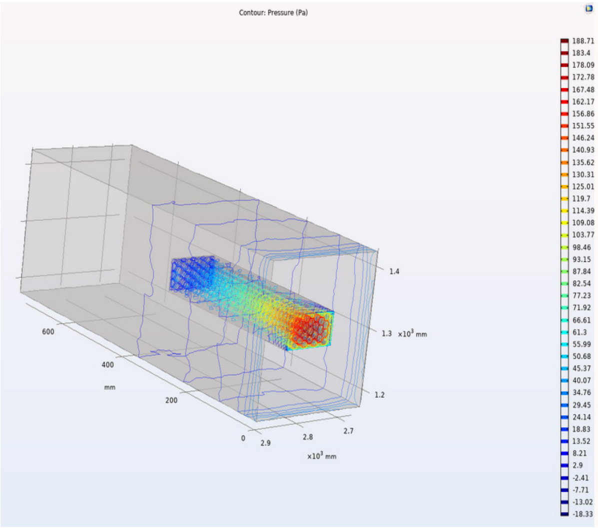

Figure 114: Pressure for Honeycomb Prism at 8 m/s

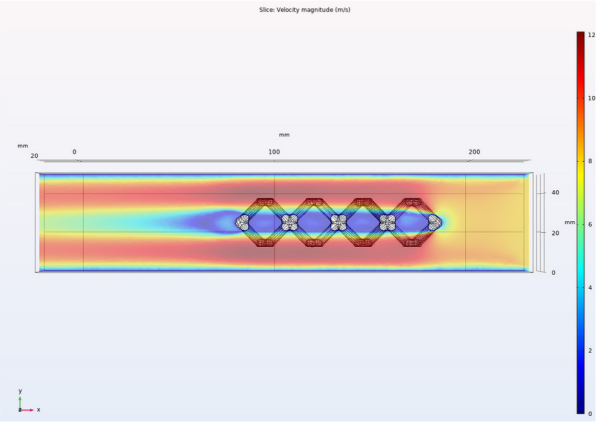

Figure 115: Air Velocity for Simplified Arch Prism at 8 m/s

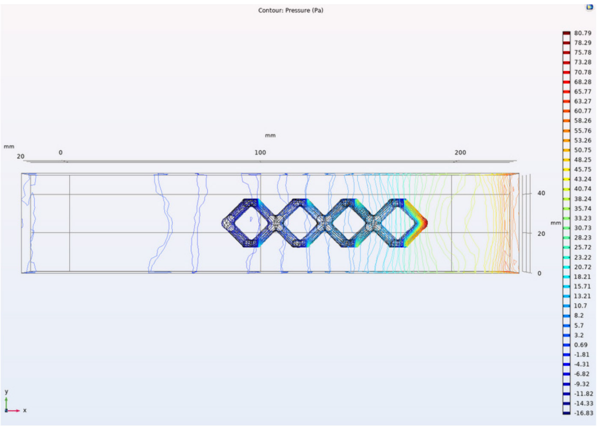

Figure 116: Pressure for Simplified Arch Prism at 8 m/s

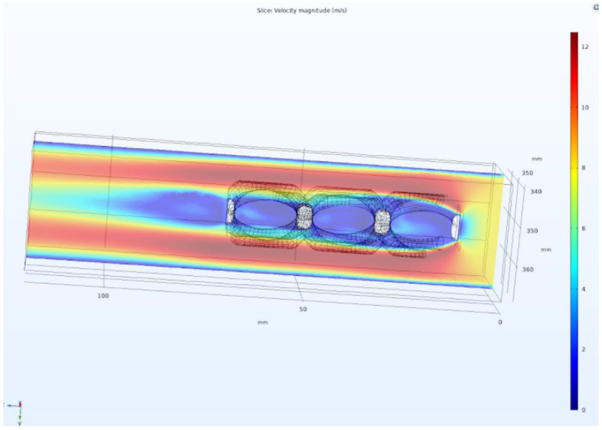

Figure 117: Air Velocity for Traditional Arch Prism at 8 m/s

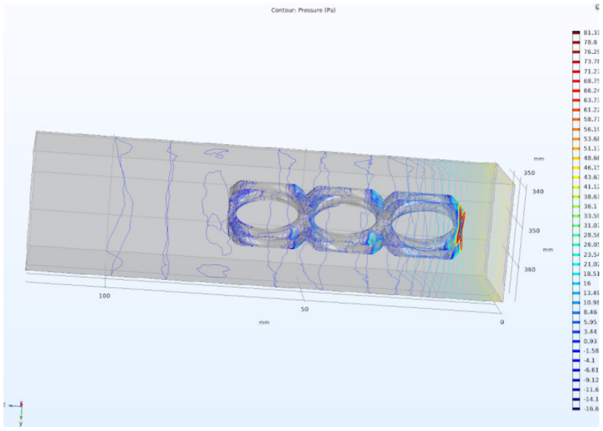

Figure 118: Pressure for Traditional Arch Prism at 8 m/s

In terms of air velocity, it was expected for the Honeycomb prism to perform best due to the lack of obstruction in the airflow, and this was reflected in simulation results, with the airflow past the Honeycomb prism reaching a velocity of approximately 140 m/s from an initial of 180 m/s for the Inconel structure and from 8 m/s to 5 m/s for the resin structure. However, with the Simplified Arch structure, the air velocity past the structure faces a massive drop to velocity nearing 30 m/s, before slowly increasing back up to the 60-100 m/s range, or from 8 m/s to 2-3 m/s in the laminar simulation. This is likely caused by the air being forced to move around the struts, resulting in the creation of several stagnation points, such as the one seen in the far right tip of the prism, hence severely reducing air velocity through the structure. A similar effect is expected and seen in the Traditional Arch structure as well, with velocity drops to 50 m/s and 3m/s for the turbulent and laminar simulation respectively.

As for pressure, the general trend is similar, with pressure at its highest when the structure first meets the airflow and lowest right behind it, with pressures reaching atmospheric pressures towards the end of each structure. However, it is noted that the Honeycomb prism does encounter higher maximum stresses in comparison to the Simplified Arch structure, and this is likely due to its face essentially acting as a wall, whereas the Simplified Arch is shaped more like a cone, meaning that airflow around the tip of the structure is smoother and therefore there is a lower magnitude in pressure. The Traditional Arch prism also encounters the largest magnitudes of pressure at the wall near the inlet, but due to the defeaturing done to the structure, it is not fully representative of the actual pressure distributions on the structure. However, it can be assumed that pressure on the faces of each strut facing the inlet would be highest as they act as small flat walls normal to the flow.

4.5.3 Heat Transfer Simulation Results

Lastly, the simulations for heat transfer in both the resin and Inconel structure were conducted. The results from the COMSOL simulations for each structure in both conditions are shown below.

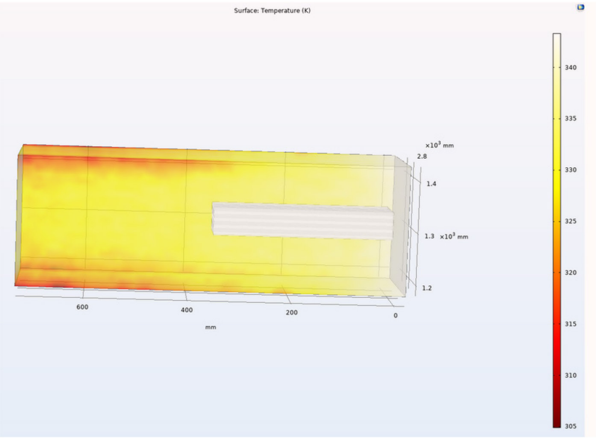

Figure 119: Temperature Change for Honeycomb Prism at 8 m/s and 343.15 K

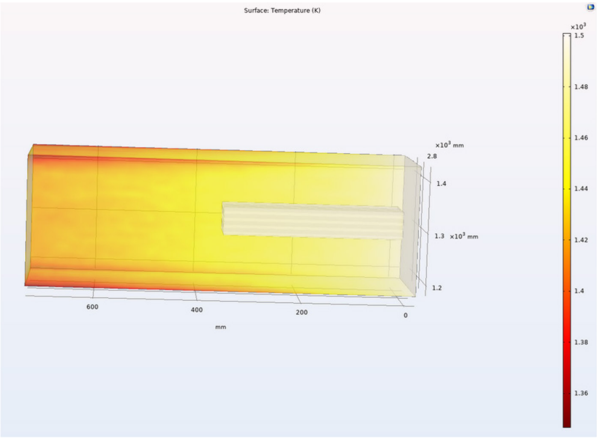

Figure 120: Temperature Change for Honeycomb Prism at 180 m/s and 1500 K

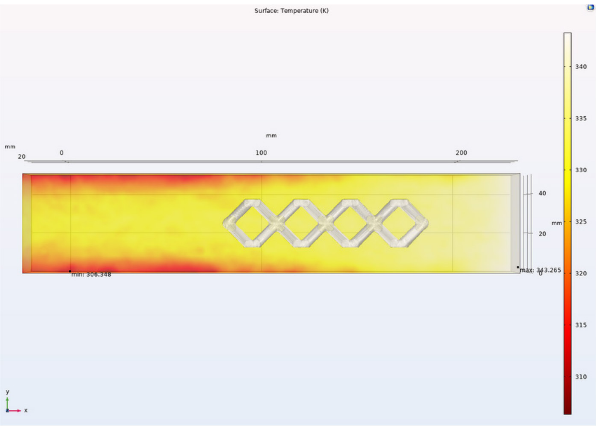

Figure 121: Temperature Change for Simplified Prism at 8 m/s and 343.15 K

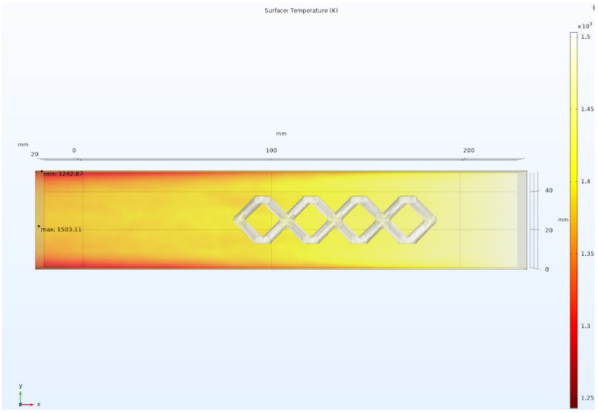

Figure 122: Temperature Change for Simplified Prism at 180 m/s and 1500 K

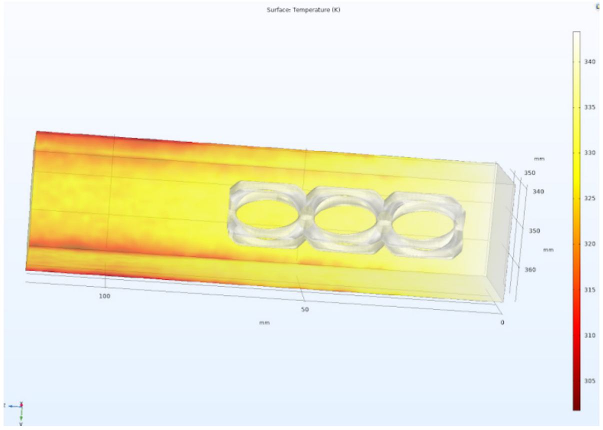

Figure 123: Temperature Change for Traditional Prism at 8 m/s and 343.15 K

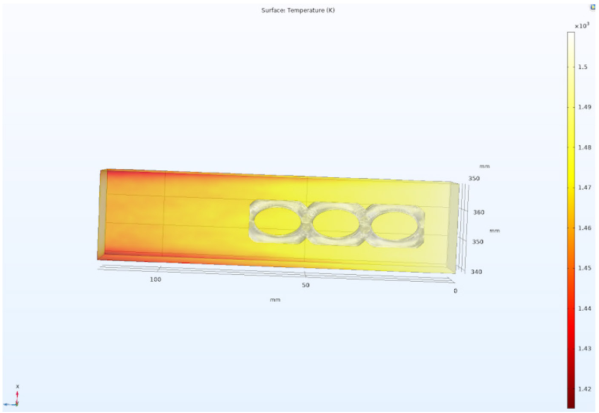

Figure 124: Temperature Change for Traditional Prism at 180 m/s and 1500 K

As seen from the figures above, the results of temperature change through the structure is mainly dependent on the initial air velocity due to heat transfer due to convection, as the temperature difference between the different prisms for the laminar flow, simulation was similar for all three, with a drop to approximately 330 K behind the structure, or a drop of about 13 K and lower after that. A similar trend can be seen with the turbulent flow simulation, but slight differences in the temperature right after the structure can be seen. For the Honeycomb prism, the drop is about 45K, whereas, for the Simplified Arch prism, this was a drop of approximately 110 K and for the Traditional Arch prism, this drop was about 40 K. As mentioned earlier, it was expected that heat transfer due to convection was going to be the dominant mode of heat transfer and turbulent flow can help amplify it, as the intense mixing of fluid in turbulent flow over the structure increases heat transfer due to convection, and this is because heat transfer between the fluid particles increases under turbulent flow. To better visualize this point, the velocity streamlines of each structure under turbulent flow are plotted below.

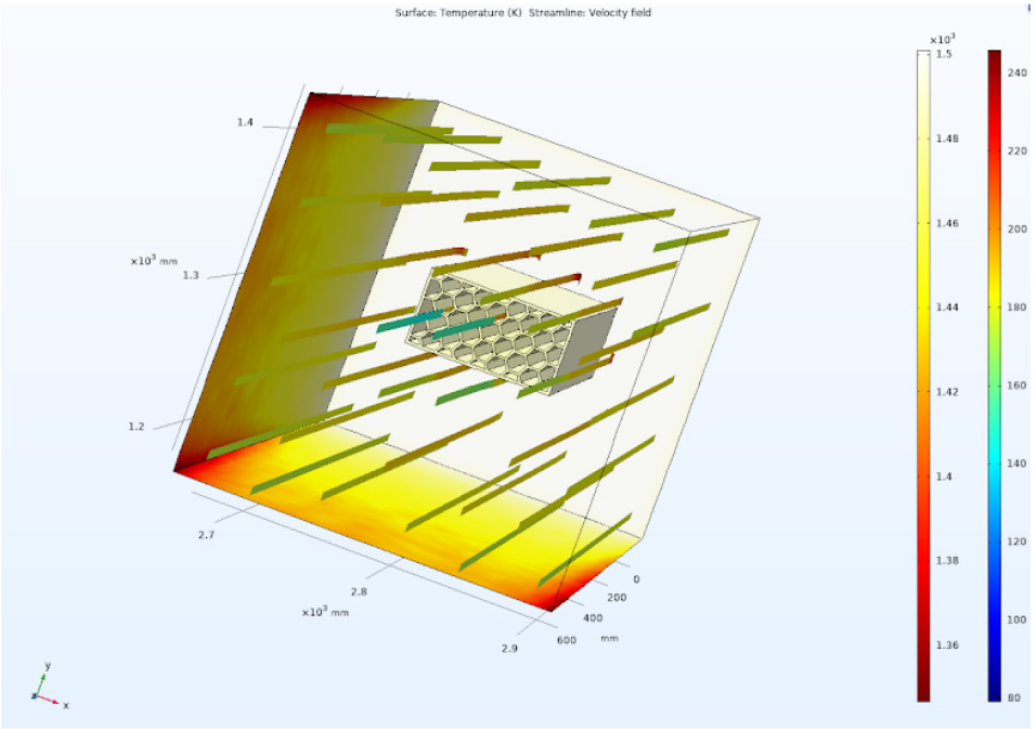

Figure 125: Velocity Streamlines of Honeycomb Prism

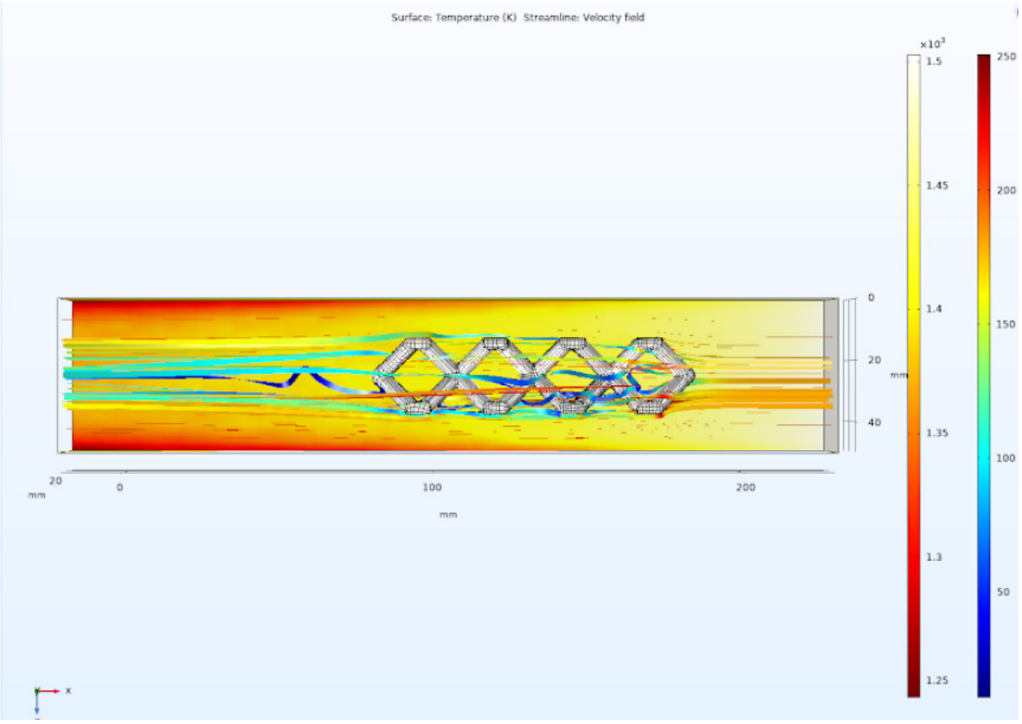

Figure 126: Velocity Streamlines of Simplified Arch Prism

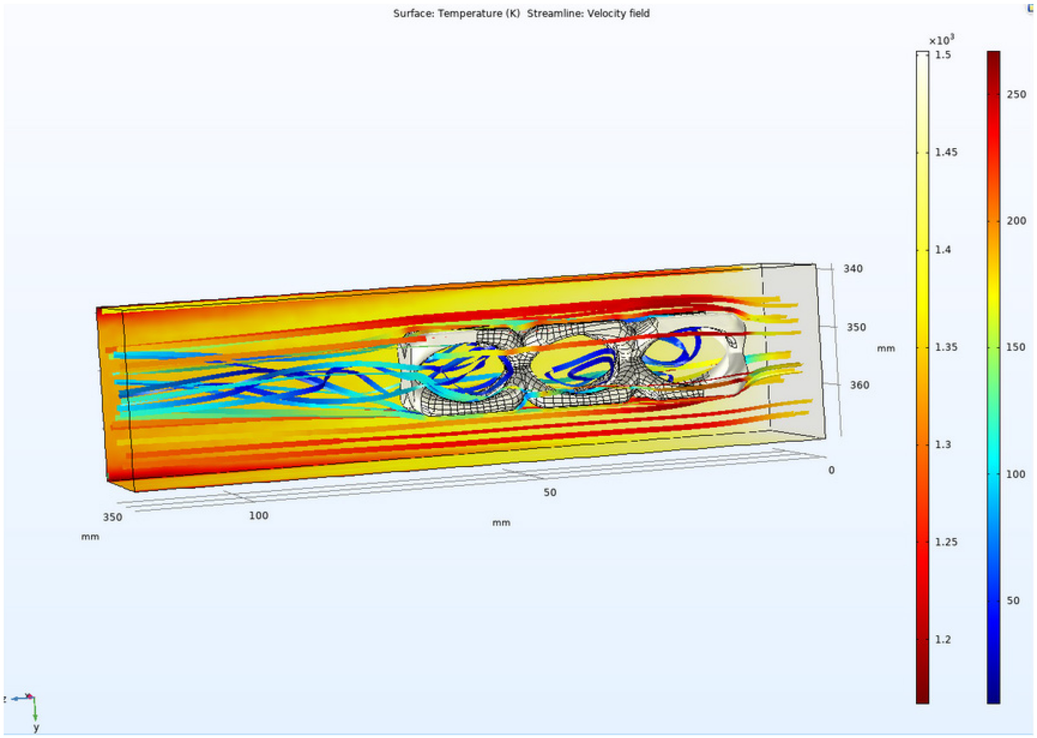

Figure 127: Velocity Streamlines of Traditional Arch Prism

In Figures 125 to 127, the background is the temperature gradient and the streamlines are colored based on the magnitude of velocity. In Figure 125, it can be seen that in the Honeycomb prism, the streamlines are relatively undisturbed, except for flow curving around the entrance of the prism itself. However, with the Simplified Arch prism in Figure 126, it can be seen that the flow in and around the structure is more turbulent than the Honeycomb prism and as a result, it had a much larger drop in temperature due to increased heat transfer due to convection. Lastly, there is the Traditional Arch prism and from a glance at Figure 127, it seems to be the most turbulent of the three, and yet the temperature drop is similar to the Honeycomb prism instead. This is likely because the airflow becomes trapped in the structure, which is most obvious in the second and last "holes" of the structure, where the velocity of the air has a large drop as shown by the dark blue color. This slow-moving air inside the structure results in a lower rate of convection, decreasing the overall heat transfer capabilities of the Traditional Arch prism structure.

4.6 Discussion

The experimental results were compared to the simulation results to determine the accuracy of the simulations. For thermal expansion, the simulation results shown in Table 8 were much smaller than the experimental results shown in Table 4. The thermal expansion coefficient for length corresponds to the z-axis and the width corresponds to the x-axis for the Honeycomb prism. For the Simplified Arch, the x-axis is the length and y is the width. For the Traditional Arch, the z-axis is the length and y is the width. Although the magnitude of the results differs, there are still similarities in some trends of the data. Comparing both the experiments and simulations, the experimental results had a larger coefficient of thermal expansion, usually by an order of 1 or 2. While differences in the magnitude of values can be explained due to different material properties, a major source of concern was the fact that for both arch prism simulations, the coefficient of thermal expansion in the y-axis, which is along the width, was negative, whereas it was positive in the experiments. While it is unsure what the reason for this discrepancy is, it is suspected that choosing rigid motion suppression, which prevents rotation of the structure under expansion for a constraint-less structure, could be the reason. Simulating free thermal expansion of the structures meant that each structure was located in free space. However, it was not possible to heat the structure in free space experimentally, hence an oven was used. When the structure is placed in an oven, the face that is resting on the oven may be treated as a constraint as the structure can’t expand in that direction. Doing so in a new simulation may then result in positive values in the width instead of negative to better match the experimental results. By comparing experimental results with the simulation results, it can be concluded that material properties used in simulation need to be modified to more closely match the properties of the structure and that certain boundaries need to be redefined in the simulation to best match the experimental setup, resulting in a more valid thermal expansion simulation.

For heat transfer, the simulation results for air temperature change across the structure were much greater than the experimental results by approximately 10-30 degrees K. This could be due to experimental constraints, such as not being able to heat the structure for longer or at higher temperatures, as the simulations were run with a steady-state study. The results from the heat transfer experiments are relatively similar to the simulations. Although all three structures perform similarly in the simulations, the Honeycomb structure absorbs slightly less heat than the other two structures. This correlates to the experimental data, which shows that hot air flowing through the Honeycomb structure has a slightly lower change in temperature than the other two structures, which perform closely. A large heat transfer capability is desired for turbine blade applications.

For velocity change, the experimental results are slightly greater than the simulation results by approximately 1-2 m/s. This could be due to experimental errors, such as the sensor detecting wind within the room because anemometers are designed to measure wind velocity. However, trends similar to the thermal expansion trends were once again noticed. In both the experiments and the simulations, the Honeycomb structure had the lowest drop in air velocity through the structure. This was as expected due to the tube-like channels created by the Honeycomb. As previously stated, a low drop in air velocity across the structure is desired.

Based on the simulation results, it can be seen that the Simplified Arch unit cell has less thermal expansion in comparison to the Traditional Arch unit cell, and this trend is propagated to the prism structures as well, with the Simplified Arch prism having the lowest coefficient of thermal expansion out of the three. As for flow properties, the Honeycomb prism structure is expected to perform best and does indeed perform best due to the individual hexagonal tubes acting as channels for air to flow through, whereas the other structures have struts and other parts of the structure disrupting the airflow. However, this disruption in airflow in both Arch prism structures results in more turbulent airflow as the air is mixing around as it flows past the structure, therefore improving its convective heat transfer capabilities. As a result, there seems to be a trend forming in which low drops in air velocity are generally a result of undisturbed flow, but undisturbed flow results in low rates of convection. Therefore, between air velocity and temperature difference, there is a balance to be had, where the structure must be able to disturb the flow to increase convection, but not by too much where velocity drops become very large, such as with the Traditional Arch prism simulation.

While our simulations generally show the trend for all three experiments, further research can be conducted to better understand actual material properties, especially for the resin, and increased familiarity with COMSOL could have also resulted in simulations that were an even closer match to the experimental setup. Doing so would likely make the simulation results closer to experimental results, meaning that the results for Inconel 718 under jet engine conditions would be more valid as well.

5. Summary, Conclusions, Recommendations, Broader Impacts

5.1 Summary

The heart of this project was exploring different types of lattice structures to see how they could most beneficially be used in the cooling of a jet engine turbine blade. This was done by taking a team of seven and splitting them into three sub-teams who performed: design, structural analyses, and thermal analyses of different lattice structures. The early stages of the project began with a multitude of research on lattice structures, their applications, what has been researched about them, and the complexity of fabrication.

The Design team worked to design and fabricate lattice structures that could be passed to other teams for further analysis. This process began with the investigation of multiple CAD software to see which would allow for the most ease. Solidworks, FLatt pack and Netfabb were explored by the team, who ultimately produced the most designs using Netfabb. Designs produced included: Orthogrid, Isogrid, Honeycomb, Simplified Arch, Traditional Arch, and Gyroid structure. These designs were made as unit cells in a variety of other configurations, as specified earlier, based on the need.

Lattice structures were printed by the Structures team. Once printed, many post-processing steps occurred to allow the structures to be used in testing. Three main tests were performed by the team, a three-point bending test, a compression test, and a tensile test. Additionally, simulations were run using ABAQUS, in an attempt to validate the results with the experiments. Tests were translated into force vs. displacement and stress vs. strain plots to better demonstrate the conclusions made.

Thermal investigations began using COMSOL to perform flow and heat flux simulations through various configurations of the presented lattice structures. In addition to the simulations, custom-built experiments used to measure thermal expansion, heat transfer, and flow velocity for low-speed and laminar flows at slightly elevated temperatures were set up. Results from both simulations and experiments were used to validate simulation results and to spot any errors from each.

5.2 Conclusions

The goal of this project was to explore the utility of a novel class of lattice-structure-based materials for effective cooling in a jet engine turbine blade, thus improving the overall efficiency of the aircraft. Over the timeframe of the project, there were three different lattice structures designed and tested. From a design perspective, the Simplified Arch lattice structure was the best. The overall simplicity of the structure, ease of design, and ability to customize the dimensions of the structure outweighed all other lattices.

Structurally, the Traditional Arch lattice is the best choice given the structures that were analyzed. The Honeycomb part, although not breaking during the three-point bending test, is a two-dimensional lattice. The arch is proved to be able to support the load up to approximately 1.3 kN in either the traditional or perpendicular orientation. Having this flexibility is more valuable in the turbine blade application due to the various forces experienced, and thus the Traditional Arch lattice is the Structure team's choice for best performing lattice structure regarding mechanical properties.

From a thermal perspective, the Honeycomb structure had the lowest and therefore the best air velocity change properties, while the Simplified Arch structure had the worst. However, the Simplified Arch structure had the lowest coefficient of thermal expansion and the greatest heat transfer capabilities. Therefore the Simplified Arch lattice was deemed to be the most successful from the view of the Thermal team.

Overall, the best structure, of those investigated in this study, to use for effective cooling while maintaining structural integrity in a jet engine turbine blade would be the Traditional Arch lattice structure due to its ease of design and customizability, while having advantageous structural properties without sacrificing desirable thermal properties.

5.3 Recommendations

Familiarity and expertise with software were an integral part of the success of our project. The majority of the time at the beginning of the project was reserved for deciding which finite element analysis and CAD software to use as well as becoming well versed in the functionality of such software. Having more time for the project would allow becoming more proficient in the software that was used. Subsequently, the more complex analysis could have been performed.

Netfabb was used for a significant portion of the designs. This software provided the capability of making more complex designs in a shorter amount of time as well as offering more customizability than previous CAD programs. However, it took time to first learn how to use the software and it took even more time to generate CAD models that could be utilized for simulations. More exposure to software such as Netfabb would allow for increased proficiency in such and thus less time spent on logistics and more on the main project objectives.

More time in the laboratory would have been advantageous for the Structures team as well, because the results were rushed when the laboratory finally opened for use. There were and always will be unforeseeable issues and troubleshooting when working with unfamiliar equipment, and more time allows for greater familiarity with the laboratory processes.

Furthermore, had the laboratory been accessible for the entire duration of this project, specific stress tests could have been iterated and improved. For example, the tensile test with the Traditional Arch lattice structure was difficult to set up so that the aluminum fixtures were completely in line with each other. In the first iteration of that arch tensile test, the fixtures were not in line, resulting in the Traditional Arch lattice undergoing uneven tensile stresses.

Regardless, it was nearly impossible to align the fixtures perfectly in-line, thus almost all the tests yielded slightly inaccurate data due to the angle of the structure. More time would allow for more iterations of the fixtures and test setup so that these sources of error could be mitigated. Nevertheless, discovering these sources of error was part of the engineering and design process. The lab test setup, fixtures, samples, and processing methods were being iterated continuously, so the error was unavoidable and could only be reduced with more testing in the laboratory. The chances of success will increase with the more time and practice an individual has worked with the equipment.

Additionally, hundreds of complications were encountered while learning and working with ABAQUS. Gaining familiarity with new software or programming language is simple, but generating productive workflow and proper techniques within these subjects is difficult. There were also many issues and troubleshooting due to a lack of familiarity with the software. Learning how to use finite element analysis software is difficult for anyone who has never done it before. The drive to learn and keep pushing through obstacles, coupled with some help from faculty who have extensive knowledge of the software, will be the keys to success for any team that may attempt to replicate this project.

Similar to the Design and Structures team, time was a huge factor in the project, and the beginning of the project consisted of selecting the necessary properties to test for, designing experiments to test said properties, and to practice using COMSOL. With more time, the intricacies of COMSOL could be better understood, allowing for more accurate and complex simulations that are more fitting to the experimental setup without resorting to strategies such as reducing the size of the model and by defeaturing the model as well.

Due to the amount of time, equipment available, and budget, several improvements could have been made to the experiments and simulations, which would have likely produced results of greater accuracy. Firstly, when calculating the coefficient of thermal expansion, instead of using software such as paint to manually calculate the difference in the number of pixels, edge detection software, such as one coded in MATLAB, could have been used instead to produce more accurate results. Secondly, when it came to air velocity and temperature difference experiments, a hairdryer was selected as it best fit our needs based on our budget and the equipment available. However, there were several issues with using a hairdryer, such as how the air velocity at the outlet of the hairdryer is not controlled, meaning there could be small changes in air velocity, impacting the results in a change in air velocity. We attempted to alleviate this by comparing results to a baseline, which had small velocity variations, but it was difficult to tell when it was happening during the experimental trial themselves. Additionally, while it was assumed that the hairdryer could be modeled as laminar flow due to the existence of a grid-like structure to ensure that flow was smooth exiting the hairdryer, it likely wasn't completely laminar, which could have resulted in some differences in comparison to simulation. Furthermore, the heating element of the hairdryer not only took time to heat up, but it also took time to cool down back to room temperature as well. Given that only 5 minutes was given to cool down the hairdryer before each trial, this may not have been enough time for it to cool down completely to room temperature, which could have resulted in higher temperatures or a quicker ramp-up of temperatures in the next two trials.

In terms of simulation, while they were modeled to best match their respective situations, there were several differences as well that could have led to more accurate results. Firstly, to save computational power and time, only a section of a row of the actual printed structure was modeled and simulated. This meant that the experiment and simulation were not an exact match and trends for the whole structure had to be extrapolated and predicted from simulations of a smaller structure. Specific to the air velocity simulations, the experimental setup consisted of a wooden circle securing the structure in the center of the tube. However, this circle was not simulated in COMSOL, hence resulting in varying changes in air velocity results as well as for temperature difference. With more time, better constraints could have been used to match the thermal expansion simulations with the experiments, as that could have led to some of the inaccuracies leading to differences in trends between the simulation and experimental data. With more time and computing power, it could be beneficial to model the entire structure as is to better understand the flow and thermal properties of the structure at hand and allow for more certainty during the validation process.

5.4 Broader Impacts

There are many impacts lattice structures have on the world. The impact can be seen in many different areas of life including economic and social. Two main ways space travel and air travel are becoming increasingly less expensive are the development of more efficient propulsion systems and lighter materials within the structure of the aircraft or spacecraft. Currently, space travel is anywhere from $10,000-20,000 per kilogram, whereas air travel is about $4-8 per kilogram. Structure and fuel make up about 90% of the weight of aircraft and spacecraft, making these two factors the most expensive part of both. Therefore the use of lighter lattice structures reduces the overall weight of both aircraft and spacecraft, thus reducing cost [14].

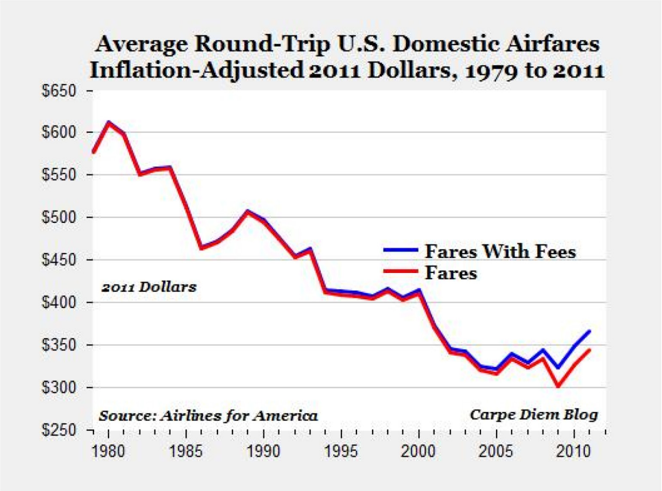

Figure 128: Average cost of domestic airfares from 1979-2011 [45]

While lattice structures prove to be economically beneficial, they also prove to be advantageous in many social aspects of the world as well. More efficient travel results in “greener travel,” which is possible with the use of lighter aircraft, thus lattice structures. Additionally, the use of this lighter material will result in noise reduction within aircraft cabins. A reduction in air travel expenses would make travel more affordable. Lattice structures again, making for lighter vehicles. Sound is vibrations within the frequency range of 20 Hz to 20,000 Hz and can be suppressed through damping measures [14]. Combining the use of damping measures and lattice structures, by designing lattice structures with damping components contribute to this idea of noise reduction with vehicles.

References

1. Abu Al-Rubb, R,. & Abueidda, D,. & Elhebeary, M,.& Jasiuk, I,. & Pang, S,. & Shiang, C, (2019). Mechanical properties of 3D printed polymeric Gyroid cellular structures: Experimental and finite element study, *Materials & Design Volume 165.* https://doi.org/10.1016/j.matdes.2019.107597
2. Abdalla, M,. & Wang, D. (2014). Buckling Analysis of Grid-Stiffened Composite Shells. https://www.researchgate.net/publication/264322273_Buckling_Analysis_of_Grid-Stiffened_Composite_Shells
3. Acharya, S., & Kanani, Y. (2017). Chapter Three—Advances in Film Cooling Heat Transfer. In E. M. Sparrow, J. P. Abraham, & J. M. Gorman (Eds.), *Advances in Heat Transfer* (Vol. 49, pp. 91–156). Elsevier. https://doi.org/10.1016/bs.aiht.2017.10.001
4. Ai, L., & Gao, X.-L. (2017). Metamaterials with negative Poisson's ratio and non-positive thermal expansion. *Composite Structures*, *162*, 70–84. https://doi.org/10.1016/j.compstruct.2016.11.056
5. Al-Ketan, O., & Ali, M., & Khalil, M., & Rowshan, R., & Khan, K. A., & Abu Al-Rub, R. K. (2021). Forced Convection Computational Fluid Dynamics Analysis of Architected and Three-Dimensional Printable Heat Sinks Based on Triply Periodic Minimal Surfaces. *Journal of Thermal Science and Engineering Applications*, *13*(2). https://doi.org/10.1115/1.4047385

6. App inc. (2018). Honeycomb Structures, Properties and Uses in Composites Manufacturing, *App Inc.* https://kb.appinc.co/knowledge-base/honeycomb-structures-properties-and-uses/
7. Arakerimath R.R., & Pisal V.S., & Rathod G.G., & Sonawane G.R., & Roy S., & Umap A.S. (2020). Stress and Deflection Analysis of Orthogrid and Isogrid Structure. In: Gunjan V., Singh S., Duc-Tan T., Rincon Aponte G., Kumar A. (eds) ICRRM 2019 – System Reliability, Quality Control, Safety, Maintenance and Management. ICRRM 2019. Springer, Singapore. https://doi.org/10.1007/978-981-13-8507-0_24
8. Azzi, W., Roberts, W., & Rabiei, A. (2005). Developing an Application for Refractory Open Cell Metal Foams in Jet Engines. *MRS Proceedings*, *851*, 511. https://doi.org/10.1557/PROC-851-NN11.3
9. Baillis, D., Coquard, R., & Randrianalisoa, J. (2012). Radiative heat transfer in honeycomb structures-New simple analytical and numerical approaches. *Journal of Physics: Conference Series*, *369*, 012006. https://doi.org/10.1088/1742-6596/369/1/012006
10. Bhate, Dhruv (2016). Classification of Cellular Solids (and why it matters). *PADT Inc.* *https://www.padtinc.com/blog/classification-of-cellular-solids-and-why-it-matters/*
11. Bowman, Randy (2000). Superalloys: A Primer history. 9th International Symposium on Superallys.https://www.tms.org/Meetings/Specialty/Superalloys2000/SuperalloysHistory.html#:~:text=)%3A%20The%20continuous%20matrix%20(called,is%20called%20gamma%20prime%20(%20)
12. Bracconi, M., Ambrosetti, M., Okafor, O., Sans, V., Zhang, X., Ou, X., Da Fonte, C. P., Fan, X., Maestri, M., Groppi, G., & Tronconi, E. (2019). Investigation of pressure drop in 3D replicated open-cell foams: Coupling CFD with experimental data on additively

manufactured foams. *Chemical Engineering Journal*, *377*, 120123. https://doi.org/10.1016/j.cej.2018.10.060

13. Chaolin T., & Sheng L., & Khamis Essa., & Parastoo Jamshidi., & Kesong Z., & Wenyou Ma., & Moataz M. A., (2019). Laser Powder Bed Fusion of Ti-rich TiNi lattice structures: Process optimisation, geometrical integrity, and phase transformations, International Journal of Machine Tools and Manufacture 141, 19-29, https://doi.org/10.1016/j.ijmachtools.2019.04.002
14. *Convective Heat Transfer*. (2003). Engineering Toolbox. https://www.engineeringtoolbox.com/convective-heat-transfer-d_430.html
15. Coopersmith, Jonathan. “Affordable Access to Space.” Issues in Science and Technology 29, no. 1 (Fall 2012). https://issues.org/jonathan/
16. Ding, R,. & Du B,. & Guo, Y,. & Kang, Z,. & Yao, J,. & Zheng, H,. (2020). Mechanical Properties and Deformation Behaviour of ARCH and BCT Lattice Structures Manufactured by Selective Laser Melting, *IOP Conf. Series: Materials Science and Engineering 727*. https://iopscience.iop.org/article/10.1088/1757-899X/727/1/012001/pdf
17. Doi, Minoru & Miki, Daisuke & Moritani, Tomokazu & Kozakai, Takao. (2004). Gamma/Gamma-Prime Microstructure Formed by Phased Separation of Gamma-Prime Precipitates in a Ni-Al-Ti Alloy. Proceedings of the International Symposium on Superalloys.10.7449/2004/Superalloys_2004_109_114
18. Downing, D., Leary, M., McMillan, M., Alghamdi, A., & Brandt, M. (2020). Heat transfer in lattice structures during metal additive manufacturing: Numerical exploration of temperature field evolution. *Rapid Prototyping Journal*, *26*(5), 911–928. https://doi.org/10.1108/RPJ-11-2018-0288

19. Echeta, I., & Feng, X., & Dutton, B. & Piano, S., & Leach, R. (2020). Review of defects in lattice structures manufactured by powder bed fusion. International Journal of Advanced Manufacturing Technology. 106. 10.1007/s00170-019-04753-4

20. Farokhi, S. (2014). *Aircraft Propulsion*. John Wiley & Sons.

21. Farnia (2014). Why Choosing Inconel 718 for Aerospace Additive Manufacturing?, *Farnia.* https://www.farinia.com/blog/why-choosing-inconel-718-aerospace-additive-manufacturing

22. Fleck, Norman (2004). An overview of the mechanical properties of foams and periodic lattice materials, *Cellular Metals and Polymers.* http://www-mech.eng.cam.ac.uk/profiles/fleck/papers/c51.pdf

23. Frei, W. (2017, July 6). Which Turbulence Model Should I Choose for My CFD Application? *COMSOL Blog*. https://www.comsol.com/blogs/which-turbulence-model-should-choose-cfd-application/

24. Ghosha, R., & Haghpanaha, B., & Hamoudab, M.A., & Mousanezhada, D., & Nayeb-Hashemia, H., & Vaziria, A (2016). Elastic Properties of Chiral, anit-chiral, and hierarchical honeycombs: A simple energy-based approach, *Theoretical and Applied Mechanics Letters 6,* 81-96. https://doi.org/10.1016/j.taml.2016.02.004

25. Goodfellow, A.J., & Galindo-Nava, E.I., & Christofidou, K.A. et al.(2018). Gamma Prime Precipitate Evolution During Aging of a Model Nickel-Based Superalloy. Metall Mater Trans A 49, 718–728. https://doi.org/10.1007/s11661-017-4336-y

26. Ha, C. S., Hestekin, E., Li, J., Plesha, M. E., & Lakes, R. S. (2015). Controllable thermal expansion of large magnitude in chiral negative Poisson’s ratio lattices. *Physica Status Solidi (b)*, *252*(7), 1431–1434. https://doi.org/10.1002/pssb.201552158

27. Jefferson, G., Parthasarathy, T. A., & Kerans, R. J. (2009). Tailorable thermal expansion hybrid structures. *International Journal of Solids and Structures*, *46*(11), 2372–2387. https://doi.org/10.1016/j.ijsolstr.2009.01.023

28. Kidane, Samuel (2002). Buckling analysis of grid stiffened composite structures, *LSU Master's Thesis.* https://digitalcommons.lsu.edu/cgi/viewcontent.cgi?article=2503&=&context=gradschool_theses&=&sei-redir=1&referer=https%253A%252F%252Fwww.google.com%252Furl%253Fq%253Dhttps%253A%252F%252Fdigitalcommons.lsu.edu%252Fcgi%252Fviewcontent.cgi%253Farticle%25253D2503%252526context%25253Dgradschool_theses%2526sa%253DD%2526source%253Deditors%2526ust%253D1613598431083000%2526usg%253DAOvVaw1PxScMKi3mlWcz_nBEHkWa#search=%22https%3A%2F%2Fdigitalcommons.lsu.edu%2Fcgi%2Fviewcontent.cgi%3Farticle%3D2503%26context%3Dgradschool_theses%22

29. "Laser Sintering, Melting and Others - SLS, SLM, DMLS, DMP, EBM, SHS." *Additive Blog*, 3 Sept. 2017, www.additive.blog/knowledge-base/3d-printers/laser-sintering-melting-sls-slm-dmls-dmp-ebm-shs/.

30. Lu, W., Zhao, C. Y., & Tassou, S. A. (2006). Thermal analysis on metal-foam filled heat exchangers. Part I: Metal-foam filled pipes. *International Journal of Heat and Mass Transfer*, *49*(15), 2751–2761. https://doi.org/10.1016/j.ijheatmasstransfer.2005.12.012

31. Lyndondr. (2004). *PeopolyWiki - Moai System Settings*. https://wiki.peopoly.net/doku.php?id=moai-system-setting.

32. Mohammadinasrabadi, Al., & Hedayati, R., & Sadighi, M. (2016). Numerical and experimental study of the mechanical response of aluminum foams under compressive loading using CT data. 54. 1357-1368. https://www.researchgate.net/figure/1-Different-foam-types-a-closed-cell-b-open-cell_fig6_310488467

33. Novak, N., & Ren, Z., & Vesenjak, M (2016). Auxetic Cellular Materials - A Review, *Strojniški vestnik - Journal of Mechanical Engineering 62(9)*, 485-493. https://doi.org/10.5545/sv-jme.2016.3656

34. Palumbo, N. M. A., Smith, C. W., Miller, W., & Evans, K. E. (2011). Near-zero thermal expansivity 2-D lattice structures: Performance in terms of mass and mechanical properties. *Acta Materialia*, *59*(6), 2392–2403. https://doi.org/10.1016/j.actamat.2010.12.037

35. Panesar, A., Abdi, M., Hickman, D., & Ashcroft, I. (2018). Strategies for functionally graded lattice structures derived using topology optimisation for Additive Manufacturing. *Additive Manufacturing*, *19*, 81–94. https://doi.org/10.1016/j.addma.2017.11.008

36. Panwisawas, C., Tang, Y.T. & Reed, R.C. (2020) Metal 3D printing as a disruptive technology for superalloys. Nat Commun 11, 2327. https://doi.org/10.1038/s41467-020-16188-7

37. Parsons, E. M. (2019). Lightweight cellular metal composites with zero and tunable thermal expansion enabled by ultrasonic additive manufacturing: Modeling, manufacturing, and testing. *Composite Structures*, *223*, 110656. https://doi.org/10.1016/j.compstruct.2019.02.031

38. Peopoly. (2021). Peopoly Forum. https://forum.peopoly.net/.

39. Prawoto, Yunan (2012). Seeing auxetic materials from the mechanics point of view: A structural review on the negative Poisson's ratio, *Computational Materials Science*, *58,* 140-153. https://doi.org/10.1016/j.commatsci.2012.02.012

40. Olmo, E. & Grande, E. & Samartin, C.R. & Bezdenejnykh, M. & Torres, J. & Blanco, Norbert & Frovel, M. & Cañas, J.. (2012). Lattice structures for aerospace applications. European Space Agency, (Special Publication) ESA SP. 691. https://www.researchgate.net/publication/287393371_Lattice_structures_for_aerospace_applications

41. Raheem, Zainab. (2019). Standard Test Methods for Flexural Properties of Unreinforced and Reinforced Plastics and Electrical Insulating Materials 1.

42. Romeorim. (2021). *romeorim.com*. Thermosets vs. Thermoplastics. https://romeorim.com/thermoset-vs-thermoplastics/.

43. Ruzzeneb, M,. & Spadonia, A (2012). Elasto-static micropolar behavior of a chiral auxetic lattice, *Journal of the Mechanics and Physics of Solids 60,* 156–171. https://citeseerx.ist.psu.edu/viewdoc/download?doi=10.1.1.1012.2113&rep=rep1&type=pdf

44. Suleiman, A. S., & Dukhan, N. (2014). Forced convection inside metal foam: Simulation over a long domain and analytical validation. *International Journal of Thermal Sciences*, *86*, 104–114. https://doi.org/10.1016/j.ijthermalsci.2014.06.022

45. Tamunobere, O. (2015). Heat Transfer and Film Cooling on a Gas Turbine Blade and Shroud. *LSU Doctoral Dissertations*. https://digitalcommons.lsu.edu/gradschool_dissertations/3331

46. Thompson, Derek. (2013). How Airline Ticket Prices Fell 50 Percent in 30 Years (And Why Nobody Noticed), *The Atlantic.* https://www.theatlantic.com/business/archive/2013/02/how-airline-ticket-prices-fell-50-in-30-years-and-why-nobody-noticed/273506/

47. Varotsis, B.A. (2021). Introduction to SLA 3D printing. 3D Hubs. https://www.3dhubs.com/knowledge-base/introduction-sla-3d-printing/

48. Vyshenska, K. (2018, June 28). How to Provide Structural Stability in Thermal Expansion Simulations. *COMSOL Multiphysics*. https://www.comsol.com/blogs/how-to-provide-structural-stability-in-thermal-expansion-simulations/

49. Wahyudin P.S., &, Wu J., & Zhao B., Maskery, I., & Elmadih W., & Leach R., Design and analysis of strut-based lattice structures for vibration isolation, *Precision Engineering*, Volume 52, 2018 ,Pages 494-506 https://doi.org/10.1016/j.precisioneng.2017.09.010.

50. Wang, Q., Jackson, J. A., Ge, Q., Hopkins, J. B., Spadaccini, C. M., & Fang, N. X. (2016). Lightweight Mechanical Metamaterials with Tunable Negative Thermal Expansion. *Physical Review Letters*, *117*(17), 175901. https://doi.org/10.1103/PhysRevLett.117.175901

51. Wu, L., Li, B., & Zhou, J. (2016). Isotropic Negative Thermal Expansion Metamaterials. *ACS Applied Materials & Interfaces*, *8*(27), 17721–17727. https://doi.org/10.1021/acsami.6b05717

52. Yahya, S. M. (2010). *Turbines Compressors and Fans*. McGraw-Hill Education (India) Pvt Limited.

53. Yang, G., Hou, C., Zhao, M., & Mao, W. (2019). Comparison of convective heat transfer for Kagome and tetrahedral truss-cored lattice sandwich panels. *Scientific Reports*, *9*(1), 3731. https://doi.org/10.1038/s41598-019-39704-2